REGIONAL MOMENT TENSOR SOURCE-TYPE DISCRIMINATION ANALYSIS

Douglas S. Dreger, et al.

University of California, Berkeley
215 McCone Hall
University of California
Berkeley, CA 94720

16 November 2015

Final Report

AIR FORCE RESEARCH LABORATORY
Space Vehicles Directorate
3550 Aberdeen Ave SE
AIR FORCE MATERIEL COMMAND
KIRTLAND AIR FORCE BASE, NM 87117-5776

DTIC COPY

NOTICE AND SIGNATURE PAGE

Using Government drawings, specifications, or other data included in this document for any purpose other than Government procurement does not in any way obligate the U.S. Government. The fact that the Government formulated or supplied the drawings, specifications, or other data does not license the holder or any other person or corporation; or convey any rights or permission to manufacture, use, or sell any patented invention that may relate to them.

This report was cleared for public release by the PRS OPSEC Office and is available to the general public, including foreign nationals. Copies may be obtained from the Defense Technical Information Center (DTIC) (http://www.dtic.mil).

AFRL-RV-PS-TR-2016-0014 HAS BEEN REVIEWED AND IS APPROVED FOR PUBLICATION IN ACCORDANCE WITH ASSIGNED DISTRIBUTION STATEMENT.

//SIGNED//   //SIGNED//
_____   _____
Robert Raistrick   Glenn M. Vaughan, Colonel, USAF
Project Manager, AFRL/RVBYE   Chief, Battlespace Environment Division

This report is published in the interest of scientific and technical information exchange, and its publication does not constitute the Government's approval or disapproval of its ideas or findings.

REPORT DOCUMENTATION PAGE

1. REPORT DATE *(DD-MM-YYYY)* 16-11-2015	2. REPORT TYPE Final Report	3. DATES COVERED *(From - To)* 23 Aug 2013 – 22 Nov 2015

4. TITLE AND SUBTITLE
Regional Moment Tensor Source-Type Discrimination Analysis

5a. CONTRACT NUMBER
FA9453-13-C-0271

5b. GRANT NUMBER

5c. PROGRAM ELEMENT NUMBER
62601F

6. AUTHOR(S)
Douglas S. Dreger, Andrea Chiang, Sean R. Ford, and Arben Pitarka

5d. PROJECT NUMBER
1010

5e. TASK NUMBER
PPM00018803

5f. WORK UNIT NUMBER
EF122615

7. PERFORMING ORGANIZATION NAME(S) AND ADDRESS(ES)
University of California, Berkeley
215 McCone Hall
University of California
Berkeley, CA 94720

8. PERFORMING ORGANIZATION REPORT NUMBER

9. SPONSORING / MONITORING AGENCY NAME(S) AND ADDRESS(ES)
Air Force Research Laboratory
Space Vehicles Directorate
3550 Aberdeen Avenue SE
Kirtland AFB, NM 87117-5776

10. SPONSOR/MONITOR'S ACRONYM(S)
AFRL/RVBYE

11. SPONSOR/MONITOR'S REPORT NUMBER(S)
AFRL-RV-PS-TR-2016-0014

12. DISTRIBUTION / AVAILABILITY STATEMENT
Approved for public release: distribution is unlimited. (377ABW-OPS-16-1057 dtd 11 Feb 2016)

13. SUPPLEMENTARY NOTES

14. ABSTRACT
In this study we developed a new iterative inversion approach to find the maximum fit surface in moment tensor source-type space that has the advantage that it does not rely on a distribution of a large number of random moment tensors, is not dependent on the particular source-type mapping used, and since it inverts for the best fit solution for specified source-types it returns the true maximum fit surface. We have also investigated the effects of shallow depth of burial on seismic moment tensor recovery, bias in solutions, and the estimation of yield. The results indicate that while shallow depth of burial can affect moment tensor recovery due to the effects of vanishing traction on computed Green's functions the combination of long-period waveforms and first-motions results in unique discrimination of explosive events, and reasonable estimates of yield. The primary focus of the research was the investigation of 3D velocity structure effects on the recovery of seismic moment tensors at regional distances. A series of synthetic sensitivity tests and applications to NTS explosions utilizing 3D Green's functions obtained by invoking source-receiver reciprocity using the LLNL SW4 finite-difference code were carried out. The results indicate that minor improvement is afforded by the consideration of 3D velocity model, path average 1D structures perform as well at less computational cost. Additional work is needed to investigate more 3D velocity structures to assess whether a different model can improve performance and to assess the uncertainties resulting from variation in 3D velocity structure.

15. SUBJECT TERMS
Seismic Moment Tensor, Seismic Source

16. SECURITY CLASSIFICATION OF:			17. LIMITATION OF ABSTRACT	18. NUMBER OF PAGES	19a. NAME OF RESPONSIBLE PERSON Robert Raistrick
a. REPORT Unclassified	**b. ABSTRACT** Unclassified	**c. THIS PAGE** Unclassified	Unlimited	112	19b. TELEPHONE NUMBER *(include area code)*

This page is intentionally left blank.

Table of Contents

List of Figures

List of Tables

Acknowledgments

We thank Weston Geophysical for providing the Humming Albatross waveform data. Plots were made with GMT (Wessel and Smith, 1998).

1. SUMMARY

In this project (FA9453-13-C-0271) we build on our earlier results (DE-FC52-06NA27324, Dreger et al., 2008; Ford et al., 2010; Ford et al., 2009a; Ford et al., 2008; Chiang et al., 2014, Nayak and Dreger, 2014) to investigate the effects of 3D velocity structure on seismic moment tensor recover and moment tensor source-type discrimination. In addition, we have investigated the effect of shallow depth of burial and the issue of vanishing traction at the free-surface on fundamental Green's function amplitudes and on the recovery of the seismic moment tensor. Finally we have developed a source-type specific inversion that enables the estimation of the true maximum fit surface in the moment tensor source-type space.

2. INTRODUCTION

The estimation of the seismic moment tensor using long-period regional distance three-component waveform data has proved to be an effective approach in the discrimination of explosions from earthquakes (Ford et al., 2009a,b; Chiang et al., 2014). In fact, the approach has been found to be able to uniquely discriminate explosions from earthquakes as evaluated in source-type space (Hudson et al., 1989; Tape and Tape, 2015) when long-period regional distance waveforms are combined with regional or teleseismic distance P-wave first-motion observations (e.g. Ford et al., 2012; Chiang et al., 2014). Sources of error such as noise in the data and poor station coverage are now routinely evaluated, however the primary source of error is due to the assumption of a suitable seismic velocity model from which to calculate the needed Green's functions for the inversion and remains an important problem. Although it is becoming common to evaluate uncertainty due to assumed 1D velocity models (e.g. Ford, 2008; Chiang et al., 2014) the effect of unaccounted for 3D velocity structure is an important open problem, which sections 3.3 and 3.4 of this report address. For the western US earthquakes and the NNSS nuclear explosions a synthetic investigation of the effects of 3D structure on the recovery of seismic moment tensors, particularly the isotropic component needed for source-type discrimination is presented. Invoking source-receiver reciprocity (Eisner and Clayton, 2001) Green's functions for a surface wave group and phase velocity constrained seismic velocity model (Moschetti et al., 2010) are applied to NNSS nuclear explosions and earthquakes to assess the recovery of the seismic moment tensor and its use in source-type discrimination.

Also during the period of the project two other important problems were studied. The first, in section 3.2, involves the effect of the free-surface boundary condition and the vanishing nature of some fundamental moment tensor Green's functions for events with shallow depth of burial. A thorough synthetic seismogram analysis of this effect on the recovery of seismic moment tensors and the discrimination potential was carried out. Shallow (~15m depth) mining related explosions were then studied at local distances to corroborate the synthetic results, and to demonstrate the ability to obtain moment tensors for these small explosions, discriminate the source-type, as well as estimate the yield of the small explosions. The second, in section 3.1, involved the development of a new inverse procedure for estimating seismic moment tensors in the framework of the source-type projections (either Hudson et al., 1989; Tape and Tape, 2015; or others). This procedure called NSSinv solves the linearized inversion for the best fitting eigenvectors for specific ratios of eigenvalues (source-type). The method is fast, improving

substantially on the brute force approach of Ford et al. (2010), and due to the direct inverse nature of the method it recovers the true maximum fit surface in source-type space. The approach is demonstrated through inversions of events occurring in a geothermal environment, those occurring as the result of the collapse of a brine cavity in a salt dome, and for a shallow mining related explosion.

3. TECHNICAL WORK

3.1. Source-Type Specific Inversion

The mapping of the fit of seismic moment tensor (MT) solutions in source-type space helps to characterize uncertainty and solution uniqueness. Current practice relies on the forward testing of a distribution of randomly generated MT in source-type space, which is slow and does not necessarily recover the true maximum fit surface. We design an iterative damped least squares inversion scheme to invert waveforms and/or P-wave first-motions (FM) for best-fitting MT solutions for specific source-types. An event associated with the sinkhole at the Napoleonville Salt Dome, Louisiana, an industrial quarry explosion and an earthquake at The Geysers geothermal field, Northern California are presented as examples. We find that the inversion method is more accurate and successful than the random search approach in recovering the region of best-fitting MT solutions or source-types and is substantially faster. The approach also enables the determination of the best-fitting MT for specified source-types such as pure double-couples, tensile cracks or explosions, as well as compound mechanisms in a single numerical framework. This section (3.1) has been published in the Bulletin of the Seismological Society of America (Nayak and Dreger, 2015).

3.1.1 Introduction

The 2nd order general seismic moment tensor (MT) is routinely used to describe source mechanisms of seismic events (Jost and Herrmann, 1989; Julian et al., 1998; Aki and Richards, 2002; Minson and Dreger, 2008). The general MT is mathematically defined to be a symmetric 3x3 matrix and has six independent components ($M_{XX}, M_{YY}, M_{ZZ}, M_{XY}, M_{YZ}, M_{ZX}$), which describe the seismic source mechanism in terms of moments of body force equivalents, i.e., double couples and linear vector dipoles. Recently, there has been renewed interest in the geometric representation, decomposition and interpretation of the general MT (Vavryčuk, 2011; Tape and Tape 2012a, b, 2013; Vavryčuk, 2015), which facilitate interpretation of seismic sources. Source-type discrimination and assessing confidence and uncertainties in source-type characterization of seismic events is of great importance, especially for monitoring of nuclear explosions (e.g., Ford et al., 2009a, b; 2010, 2012; Chiang et al., 2014) and analysis of induced seismic events (e.g., Šílený et al., 2009; Guilhem et al., 2014). In this study, we describe the concept of a source-type specific MT inversion. We provide the expressions for a general MT in terms of its normalized eigenvalues, eigenvectors and a moment scale factor. Then we describe an iterative damped least squares (LS) inversion scheme to invert for best-fitting eigenvectors and moment scale factor for an event using its displacement waveforms for a given source-type, i.e., its normalized eigenvalues that enables the construction of the maximum goodness of fit surface in the source-type space. We validate the inversion scheme by applying it on synthetic and observed seismic waveforms, and analyze the results. Finally, we also test a method to incorporate P–wave first motion (FM) polarities in the inversion.

3.1.2 Methodology

Let a given general MT, **M**, have eigenvalues, $\boldsymbol{\lambda_0} = [\lambda_{0,1}, \lambda_{0,2}, \lambda_{0,3}]$ and corresponding eigenvectors $\mathbf{e_1}, \mathbf{e_2}$ and $\mathbf{e_3}$ ($\mathbf{e_i} = [e_{i1}, e_{i2}, e_{i3}]$). The general MT being real and symmetric has eigenvalues and eigenvectors that are real and orthonormal, respectively. $\boldsymbol{\lambda_0}$ determines the seismic scalar moment and the source-type, and can be normalized to a unit vector, $\boldsymbol{\lambda}$, by its L2-norm, m_0^2 ($= \sqrt{\sum_{i=1}^{3} \lambda_{0,i}^2}$).

$$\lambda_i = \frac{\lambda_{0,i}}{m_0^2} \; for \; i = 1,2,3 \; (1)$$

m_0^2 is a moment scale factor, defined as a square so that it remains non-negative and characterizes the absolute size of MT eigenvalues (or of MT elements) independent of their sign. Substituting $\lambda_{0,i} = \lambda_i \times m_0^2$ in equation (22) in Jost and Herrmann (1989), each MT element, M_{ij}, can be expressed as a scalar function of the moment scale factor, normalized eigenvalues and orthonormal eigenvectors, where

$$M_{ij} = m_0^2 \left(\lambda_1 e_{1i} e_{1j} + \lambda_2 e_{2i} e_{2j} + \lambda_3 e_{3i} e_{3j} \right) for \; i = 1,2,3 \; and \; j = 1,2,3 \; (2)$$

in which 1, 2 and 3 represent X, Y and Z for the MT elements. The aim of this study is to assume specific values of $\boldsymbol{\lambda}$, and then solve for m_0^2 and MT eigenvectors $\mathbf{e_1}, \mathbf{e_2}$ and $\mathbf{e_3}$, using seismic waveforms and/or polarities. We also discuss the utility of MT inversions whose solutions are constrained to specific values of $\boldsymbol{\lambda}$.

Parameterization of Eigenvectors

The orthonormal eigenvectors $\mathbf{e_1}, \mathbf{e_2}$ and $\mathbf{e_3}$ can be expressed in terms of either spherical $(\theta_1, \theta_2, \theta_3)$ or cartesian $(a_1, a_2, a_3, b_1, b_2)$ parameters. In this study we develop the cartesian parameterization as we found it to have better convergence properties. In the electronic supplement, we provide the alternative parameterization in spherical coordinates and show that it can be used with the same inversion scheme to obtain nearly the same results, albeit with slower convergence towards the best-fitting solution.

Assuming the five unconstrained real parameters $(a_1, a_2, a_3, b_1, b_2)$ of the 3D cartesian system, we can define $\mathbf{e_1}$ and $\mathbf{e_2}$

$$\mathbf{e_1} = \frac{[a_1, a_2, a_3]}{r_1} \; (3)$$

$$\mathbf{e_2} = \frac{[a_3 b_1, a_3 b_2, -(a_1 b_1 + a_2 b_2)]}{r_2} \; (4)$$

$$r_1 = \sqrt{\sum_{i=1}^{3} a_i^2}, \qquad r_2 = \sqrt{(a_3 b_1)^2 + (a_3 b_2)^2 + (a_1 b_1 + a_2 b_2)^2} \; (5)$$

$$\mathbf{e_3} = \mathbf{e_1} \times \mathbf{e_2} \quad (6)$$

It is important to note that there is innate numerical non-uniqueness in solutions of orthonormal eigenvectors for a particular MT. There are 4 combinations ($\pm\mathbf{e_1}, \pm\mathbf{e_2}$) of $\mathbf{e_1}, \mathbf{e_2}$ and $\mathbf{e_3}$ that give the same MT (equation 2). In addition, the number of independent parameters required for defining 3 orthonormal eigenvectors is 3. For the cartesian formulation in equations (3.1.3-6), our model is over-parameterized in order to allow the model parameters to assume any value, as long as $\mathbf{e_1}$ and $\mathbf{e_2}$ are not zero vectors. As a result, there can be infinite combinations of $(a_1, a_2, a_3, b_1, b_2)$ that lead to the same values of $\mathbf{e_1}, \mathbf{e_2}$ and $\mathbf{e_3}$.

Inverse Problem Formulation

Elements of $\mathbf{e_1}, \mathbf{e_2}$ and $\mathbf{e_3}$ in equation (2) can be substituted by a_1, a_2, a_3, b_1 and b_2 to obtain scalar expressions of MT elements, M_{ij}, in terms of $m_0^2, \boldsymbol{\lambda}$ and the eigenvector parameters.

$$\mathbf{m'} = \mathbf{f}(\boldsymbol{\lambda}, m_0^2, a_1, a_2, a_3, b_1, b_2) \quad (7)$$

where $\mathbf{m'}$ and $\mathbf{f}$ are column vectors containing MT elements and their scalar expressions, respectively.

Now the MT elements in the expressions relating transverse ($\mathbf{u_T}$), radial ($\mathbf{u_R}$) and vertical ($\mathbf{u_Z}$) displacements to the MT and Green's Functions (GF) matrix ($\mathbf{G}$) in Minson and Dreger (2008) can be replaced by their functions in terms of $\boldsymbol{\lambda}, m_0^2, a_1, a_2, a_3, b_1$, and b_2.

$$\mathbf{u_{T,R,Z}} = \mathbf{Gm'} \quad (8)$$

$$\mathbf{u_{T,R,Z}} = \mathbf{G\,f}(\boldsymbol{\lambda}, m_0^2, a_1, a_2, a_3, b_1, b_2) \quad (9)$$

Equation (8) is valid for a point source that assumes the source-time function to be an impulse or a Dirac delta function in space and time that is common for all MT elements. For constant and known source-type $\boldsymbol{\lambda}$, we can invert for the six unknown parameters $(m_0, a_1, a_2, a_3, b_1, b_2)$. Since we know the exact expressions for f and its derivatives, we choose to solve the problem using an iterative damped LS inversion scheme as follows

$$\mathbf{du_{T,R,Z}} = \mathbf{G}\left(\frac{\partial \mathbf{f}}{\partial m_0} dm_0 + \sum_{i=1}^{3} \frac{\partial \mathbf{f}}{\partial a_i} da_i + \sum_{i=1}^{2} \frac{\partial \mathbf{f}}{\partial b_i} db_i\right) \quad (10)$$

Defining the model parameter vector $\mathbf{dx}$

$$\mathbf{dx} = [dm_0, da_1, da_2, da_3, db_1, db_2]^T \quad (11)$$

$$\mathbf{P} = \mathbf{G}\left[\frac{\partial \mathbf{f}}{\partial m_0} \; \frac{\partial \mathbf{f}}{\partial a_1} \; \frac{\partial \mathbf{f}}{\partial a_2} \; \frac{\partial \mathbf{f}}{\partial a_3} \; \frac{\partial \mathbf{f}}{\partial b_1} \; \frac{\partial \mathbf{f}}{\partial b_2}\right] \quad (12)$$

$$\mathbf{du_{T,R,Z}} = \mathbf{Pdx} \quad (13)$$

$$\mathbf{dx} = (\mathbf{P}^T\mathbf{P} + k\mathbf{I})^{-1}\mathbf{P}^T\mathbf{du_{T,R,Z}} \quad (14)$$

where k is a damping parameter. The data goodness of fit parameter is the variance reduction (VR; expressed in %), a measure of normalized goodness of fit between observed and synthetic

data (Pasyanos *et al.*, 1996). The expressions of partial derivatives in equation (12) are provided in Appendix.

Equation (9) is exact and the user can choose to solve it using any appropriate numerical inversion technique. This approach to the problem also implies that it would be possible to estimate the best-fitting source-type or eigenvalues, for specific orientation/eigenvectors, such as for a specific fault plane or DC focal mechanism.

Inversion Parameters

The iterative damped LS inversion procedure depends on many parameters like the damping parameter, initial model parameters and number of iterations. A few trials ($\lesssim 15$) with different initial model parameters are usually sufficient for convergence to the best-fitting MT solution. We use randomly generated real numbers of the order ~ 1 for initial values of a_1, a_2, a_3, b_1 and b_2. For m_0, we use initial values logarithmically distributed over an order of magnitude around ~ $\sqrt{M_0/1.0e13}$, where M_0 is the scalar seismic moment (in N.m) computed from preliminary analyses or general MT inversion using the definition of Bowers and Hudson (1999). It is important to note that the cartesian eigenvector model is over-parameterized and therefore, only 3 out of 5 columns in **P**, i.e. containing partial derivatives of **f** with respect to $(a_1, a_2, a_3, b_1, b_2)$, are linearly independent. Since **P** is a rank deficient matrix (rank(**P**) = 4), a non-zero damping value (k) must be used for $\mathbf{P}^T\mathbf{P}$ to be invertible. We have found from trial and error that k ~ 1E-10 performs well. Multiple solutions of $(a_1, a_2, a_3, b_1, b_2)$ give the same ($\mathbf{e_1}$, $\mathbf{e_2}$), and 4 combinations of $\mathbf{e_1}$ and $\mathbf{e_2}$ ($\pm\mathbf{e_1}, \pm\mathbf{e_2}$) give the same MT elements and therefore, the same waveform fits. Depending on the initial values, the inversion proceeds towards any of these solutions, minimizing the least square error between observed and predicted waveforms. With successive iterations, linearly independent MT elements (which are functions of model parameters and fixed $\boldsymbol{\lambda}$) converge towards their best-fitting values. We terminate the inversion if VR changes less than 0.01% over 2 successive iterations.

3.1.3 Tests on Synthetic Waveforms

We use synthetic waveforms to evaluate the effectiveness of the inversion procedure. We forward model synthetic three-component displacement waveforms at seismic stations in Northern California using equation (8) with 100 randomly generated MT assuming random eigenvectors and random values of m_0 (between 10^{-2} and 10^{+2}) for each of 4 source-types:, (1) pure DC ($\boldsymbol{\lambda} = [0.7071, 0, -0.7071]$), (2) a tensile crack in Poisson's solid ($\nu = 0.25$; $\boldsymbol{\lambda} = [0.9045, 0.3015, 0.3015]$), (3) explosion ($\boldsymbol{\lambda} = [0.5774, 0.5774, 0.5774]$), and (4) pure CLVD ($\boldsymbol{\lambda} = [0.8165, -0.4082, -0.4082]$). For these hypothetical events and the real seismic events described in the subsequent sections, the GF were computed using appropriate velocity and density models for each region and a frequency–wavenumber integration code based on Haskell (1964), and Wang and Herrmann (1980) as provided in Herrmann (2013). The frequency-wavenumber integration method computes complete three-component seismograms (including near-field terms) consisting of all body-wave and surface-wave phases for 1D layered velocity models. Table 1 shows the basic information on the seismic events in this study. For the randomly oriented hypothetical seismic events, filtered GF were used to compute synthetic waveforms with the randomly generated MT. The same GF were used for inversion to investigate convergence properties of the linearized inversion. Figure 1 shows the recording

stations for synthetic test events located at 8 km depth and one example source mechanism. In this study, we decompose all MT into a combination of isotropic, DC and CLVD MT assuming same principal stress orientations for DC and CLVD MT (e.g., Jost and Herrmann, 1989), and compute their relative contribution to the total M_0 (DC, CLVD and ISO expressed in % in Figure 3.1.3b). For all 4 source-types, all respective 100 iterative inversions, MT were recovered correctly with all MTVR (model goodness-of-fit comparing the inverted MT solution with the actual MT used to compute synthetic data) and waveform VR greater than 99.5% and 99.7%, respectively.
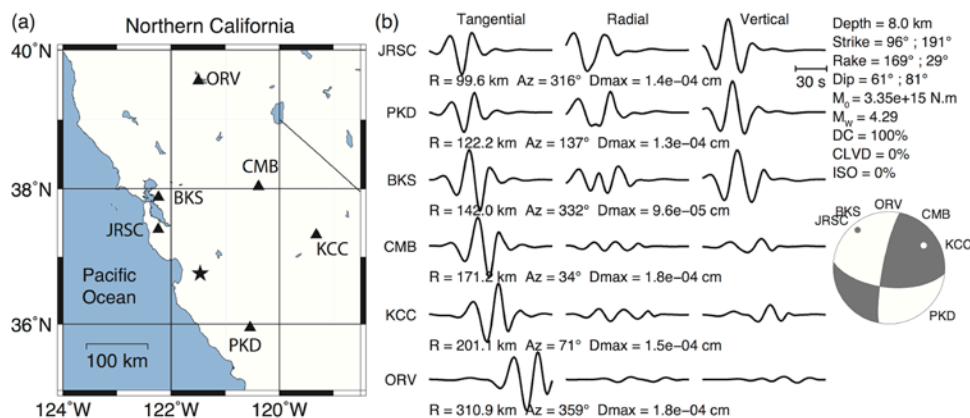
Figure 1. (a) Map shows the epicenter (black star) of a hypothetical seismic event, whose synthetic waveforms at Berkeley Digital Seismic Network stations (black triangles) were used for evaluation of the inversion procedure proposed in this study, assuming different source-types. (b) Three-component synthetic displacement waveforms (0.02-0.05 Hz) for one example random MT solution assuming a DC source-type. R = epicentral distance, Az = azimuth, and Dmax = maximum displacement amplitude at a station. Beach-ball represents lower hemisphere P-wave radiation pattern.

Table 1. Event information and parameters of MT inversion for the three events in this study.

	Hypothetical Events	Event TE1, NSD Sinkhole	Event TE2, HUMMING ALBATROSS	Event TE3, The Geysers, Northern California
Reference	-	Nayak and Dreger (2014, 2015)	Chiang *et al.* (2016)	Boyd *et al.*, (2015)
Date (yymmdd)	-	20120801	-	20110301
Origin time (hh:mm:ss.ss)	-	20:52:38.50	-	02:19:47.01
Hypocenter- Longitude (°E), Latitude (°N), Depth (km)	-121.464, 36.755, 8.0	-91.1422, 30.0112, 0.47	- Depth = 9 m	-122.8200, 38.8153, 3.5
M_W	-	1.36	1.89	4.50
Type of waveforms used	Displacement	Displacement	Velocity	Displacement
Filter (Butterworth)	0.02-0.05 Hz, p 2 n 2	0.1-0.2, or 0.1-0.3 Hz, p 1 n 4	1.2-2.0 Hz p 2 n 2	0.02-0.05 Hz, p 2 n 4
Recording network	Berkeley Digital Seismic Network	US Geological Survey Temporary Network	Temporary broadband and short period seismometers	Berkeley Digital Seismic Network, Northern California Seismic Network, Lawrence Berkeley National Laboratory Short Period Network at The Geysers
Velocity Model	gil7 (Pasyanos *et al.*, 1996)	Nayak and Dreger (2014)	Saikia *et al.* (1990)	gil7, SoCal (Dreger and Helmberger, 1993)
Number of stations used for waveform inversion	6	5	5	11
Distance range of stations for waveform inversion (km)	100-311	0.4-1.4	1.2-4.3	61-230
Number of first motion P-wave polarities	-	6	16	173
Inverse distance weights for waveform-only MT Inversion	yes	no; inverse variance weights used instead	yes	yes

3.1.4 Tests on a Real Event

Numerous seismic events were associated with the development of a sinkhole at the western edge of the Napoleonville salt dome (NSD), Louisiana in 2012. MT inversion of these events using a grid-search approach and separate preliminary 1D velocity models for the salt dome and the surrounding sediment sequence yielded large isotropic volume-increase components in the MT solutions (Nayak and Dreger, 2014). The centroid locations of these events were found to be at the western edge of the salt dome at ~ 470 m depth. Here we use the iterative damped LS inversion scheme to estimate the MT solution of one of these events (event TE1 in Nayak and Dreger [2014]) assuming various source-types. In this study, we consider pure opening cracks assuming sources in soft sediments ($\nu \sim 0.43$) and salt ($\nu \sim 0.24$), a pure DC source and a pure explosion. λ corresponding to these four sources are indicated in Figure 2. For the MT inversion of this event and other real seismic events described subsequently, three-component broadband velocity waveforms were first corrected for instrument response, integrated to displacement and then filtered in a low-frequency pass band appropriate for each seismic event. The horizontal, east-west and north-south components were rotated to radial and transverse components. GF were filtered in the same pass band as the observed waveforms.
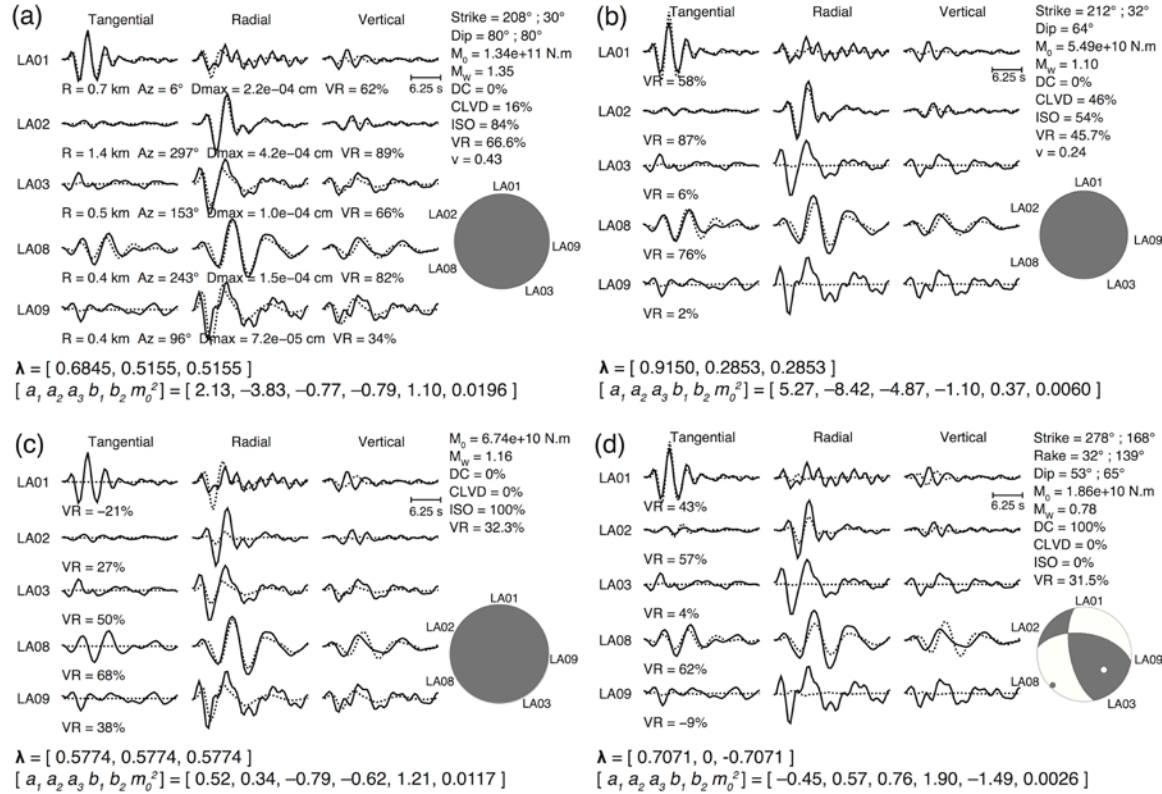
Figure 2. Best-fitting MT solutions of event TE1 described by normalized eigenvalues (λ), eigenvector parameters (a_1, a_2, a_3, b_1, b_2) and seismic moment scale factor (m_0^2) for various source-types: (a) tensile crack in sediment, (b) tensile crack in salt, (c) pure explosion and (d) a DC. The solid and dashed lines are observed and synthetic displacement waveforms, respectively. Meaning of other symbols is same as in Figure 1b. Station-specific R, Az and Dmax are same in all subplots. Waveforms were filtered in the pass band 0.1-0.3 Hz for stations LA01, LA02, LA03 and LA09, and in 0.1-0.2 Hz for station LA08. Final values of (a_1, a_2, a_3, b_1, b_2) are non-unique (see Figure A2, Appendix).

The best fitting MT solutions and waveform fits for various source-types for event TE1 are shown in Figure 2. A DC source, an explosion and a pure crack in salt fit the waveforms poorly at VR 31.5%, 32.3% and 45.7%, respectively. However, a pure crack in sediments fits the waveforms well at 66.6%, which is slightly lower than VR for the full MT solution, 68.3% (Nayak and Dreger, 2014). The uniform-phase nature of long-period S-waves observed in radial components at all stations favors a volumetric source, whereas the strong variation of amplitudes with azimuth, and the presence of SH waves favors a tensile-crack-type source rather than a spherically symmetric explosion. The strike of the tensile-crack plane for a crack in sediments (30° or 208°) agrees very well with the strike of the DC component in the full MT solution (17° or 232°) and with the strike of a shear-tensile source (crack + DC) in sediments (23° or 225°) estimated in Nayak and Dreger (2014). To verify our results, we estimated best fitting MT solutions for these source-types using a grid search, and found the results agreed very well with our inversion results. With this method separate constrained and linearized LS inversion formulations or grid search formulations for common source-types like explosions (Ford *et al.*, 2009b), DC (Herrmann *et al.*, 2011), crack and pipe (Nakano and Kumagai, 2005; Minson *et al.*, 2007) sources can be replaced by a single mathematical formulation and inversion procedure where the user is required to only specify appropriate normalized eigenvalues for a particular source-type. Moreover, the grid-search approach to estimate the best fitting values of M_0 and fault plane parameters (e.g., ϕ [strike], ζ [rake] and δ [dip] for pure DC MT solutions) is generally time consuming (Herrmann *et al.*, 2011).

3.1.5 Application to Maximum Fit Surfaces in Source-Type Space

The maximum fit surface in source-type space has been called the Network Sensitivity Solution (NSS) in Ford *et al.* (2010) due to its ability to assess recovery of source-type information under changing network topology. The NSS is also used to assess confidence in source mechanisms of seismic events that are obtained from MT inversion with respect to its source-type (or normalized eigenvalues). The NSS compares fits between observed and synthetic waveforms for a large population (usually on the order of tens of millions) of MT covering the entire source-type space (Ford *et al.*, 2010). MT are assembled from random populations of eigenvalues and orthonormal eigenvectors. The eigenvalues are randomly drawn from a population of real numbers uniformly distributed between $-nL$ and nL where $L = \frac{\|\mathbf{u_{T,R,Z}}\|}{\|\mathbf{G}\|}$ is a factor representing absolute size of the eigenvalues and the value of n (usually > 7) specifies the range of the eigenvalues with respect to L. Since the NSS depends on $\mathbf{u_{T,R,Z}}$ and $\mathbf{G}$, it takes into account the station distribution, frequency content of waveforms, and data quality and quantity for a given MT inversion scenario. It generates a distribution of VR in source-type space that allows us to identify the uniqueness of the source-type obtained from MT inversion, and the existence of possible tradeoffs commonly observed in nuclear explosions (Ford *et al.*, 2010; Chiang *et al.*, 2014). The eigenvalues are used to compute the two source-type parameters: ε and k (Hudson *et al.*, 1989). In the Hudson plot (Hudson *et al.*, 1989) the horizontal axis plots the ratio of the deviatoric eigenvalues (ε) and the vertical axis plots the relative isotropic component (k). For each coordinate (ε, k), the best VR value from all MT corresponding to a small area

around that coordinate is selected and plotted to generate the NSS (Ford *et al.*, 2010).
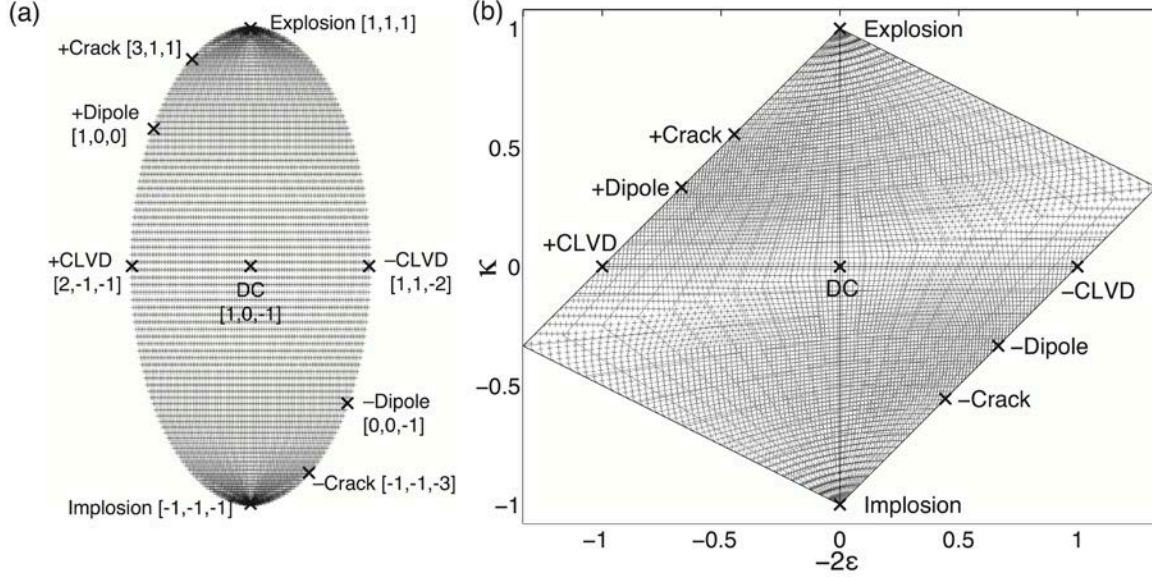
Figure 3. Grid of 7457 unique normalized eigenvalues (black '+' signs) or unique source-types on (a) the fundamental Lune (Tape and Tape, 2012a,b), and (b) on the Hudson source-type plot (Hudson *et al.*, 1989). Black crosses are positions of major theoretical source-types shown with their un-normalized eigenvalues.

The forward modeling of synthetic waveforms for millions of MT required to produce the NSS is computationally intensive and time consuming. Moreover, considering a 6D parameter space, the population of random MT needs to be very large in order to get some of the MT close to the true best-fitting solutions for a particular source-type, which can, at best, be approximate. However, we can use our source-type specific MT inversion method to compute the NSS with greater accuracy and efficiency. We first construct a grid on the fundamental Lune of the normalized eigenvalue sphere using equation (20) of Tape and Tape (2012a), which is reproduced in equation (15) with the radial coordinate set to unity.

$$\begin{bmatrix} \lambda_1 \\ \lambda_2 \\ \lambda_3 \end{bmatrix} = \mathbf{U}^T \begin{bmatrix} \cos\gamma\sin\beta \\ \sin\gamma\sin\beta \\ \cos\beta \end{bmatrix}, where\ \mathbf{U} = \frac{1}{\sqrt{6}} \begin{bmatrix} \sqrt{3} & 0 & -\sqrt{3} \\ -1 & 2 & -1 \\ \sqrt{2} & \sqrt{2} & \sqrt{2} \end{bmatrix} \ (15)$$

We keep the grid spacing in co-latitude β fixed at 1.8° and decrease the grid spacing in longitude γ linearly from ~ 1° at the poles to ~ 0.6° at latitudes ± 65°, keeping it fixed at ~ 0.6° around the equatorial region (Figure 3a). This grid, comprising of 7457 unique coordinates, representing unique sets of normalized eigenvalues or unique source-types ($\boldsymbol{\lambda}$), is projected on the Hudson plot (Figure 3b). The eigenvalue sets are arranged in a sequence having continuity in source-type space. For each $\boldsymbol{\lambda}$, we apply our iterative damped LS inversion scheme to estimate best-fitting values of m_0, a_1, a_2, a_3, b_1 and b_2. To estimate initial model parameter values for each $\boldsymbol{\lambda}$, we construct an initial population of ~50 solutions of m_0, a_1, a_2, a_3, b_1 and b_2 using values from inversion results of the previous $\boldsymbol{\lambda}$ (thus exploiting continuity of MT solutions in

source-type space) and additional values of m_0 logarithmically distributed over two orders of magnitude. This set of solutions is used to forward model synthetic waveforms and the solution that returns the best VR, is used as the initial model. Sequentially repeating this process for all $\boldsymbol{\lambda}$ in the grid generates best-fitting eigenvectors and moment scale factors for all $\boldsymbol{\lambda}$, yielding the best-fitting VR surface covering the fundamental Lune or the Hudson space. We also skip over one or two eigenvalue sets in the grid if VR at the previous $\boldsymbol{\lambda}$ is between ~20% and 30%, or less than ~20%, respectively. This increases the overall speed at the cost of VR resolution in those regions of the source-type grid that fit the waveforms poorly.

We compute NSS for: (1) event TE1 of the NSD sinkhole sequence (Nayak and Dreger, 2014) described above, (2) event TE2, a chemical explosion for industrial applications (Chiang, A., et al, 2015), and (3) event TE3, an earthquake at The Geysers geothermal field, Northern California (Table 1).

TE2 is shot 800 in HUMMING ALBATROSS, an industrial quarry blast experiment involving a set of chemical explosions at very shallow depths (~10 to 15 m) and recorded at distances up to several kilometers away (Chiang *et al.*, 2016). Data of these explosions have been analyzed in detail to study MT solutions in different frequency bands, depth dependence of MT solutions and source-type discrimination using both waveforms and FM polarities (Chiang *et al.*, 2016).

TE3 is an earthquake at The Geysers geothermal field in Northern California that has witnessed a considerable increase in number of small magnitude earthquakes (M_W 1.5 to 4.0) in response to steam production and water injection for reservoir recharge since the 1960s. Anomalous isotropic components have been detected in full MT solutions of many $M_W > 3.5$ earthquakes at The Geysers. The event we study (TE3) is a M_W 4.5 earthquake on 1 March 2011, that has a well constrained 30% isotropic volume-increase component in its full MT solution (Boyd *et al.*, 2015).

The NSS results for the three events are shown in Figure 4. MT solutions that produce the best fits for the sinkhole event TE1 are tightly clustered in a region between theoretical explosions and tensile cracks, quite far away from theoretical deviatoric mechanisms and the expected closing cracks for a collapse process, which produce fits only up to VR ≤ 35% (Figure 4a). Comparison of the shape of the NSS in Figure 4a computed using 0.1-0.3 Hz waveforms, with NSS in Figure 14a in Nayak and Dreger (2014) computed using 0.1-0.2 Hz waveforms, demonstrates that the constraints on source-type are stronger for NSS computed using waveforms in a broader frequency pass band.
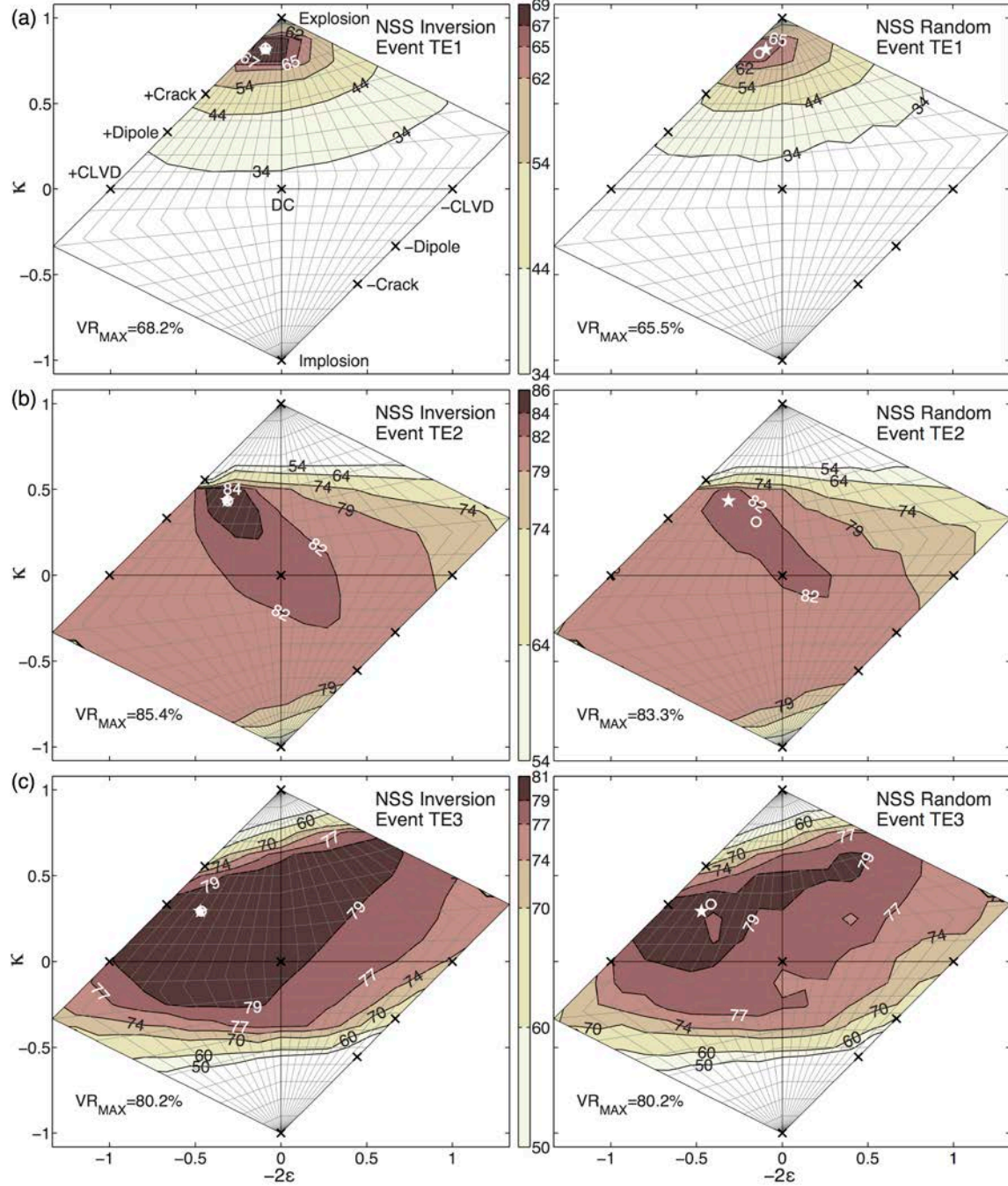
Figure 4. NSS of the three events using low-frequency displacement waveforms: (a) TE1, (b) TE2 and (c) TE3. Left panels (NSS Inversion) show NSS computed using the inversion approach in this study. Right panels (NSS Random) show NSS computed using randomly generated 80 million MT. The contours and shading represent absolute values of VR (%) whereas NSS plots in other studies usually show normalized VR (e.g., Guilhem *et al.*, 2014; Nayak and Dreger, 2014; Chiang *et al.*, 2014; Boyd *et al.*, 2015). For each event, the VR scale is same for both NSS plots (left and right) to enable better comparison. Black crosses are positions of major theoretical source-types. For each event the white star is the position of the best-fitting full MT solution from a time-domain full MT inversion of waveforms. In each plot the white circle is the source-type corresponding to the maximum VR recovered by each NSS (VR$_{MAX}$ in the lower left corner). The color version of this figure is available only in the electronic edition.

For event TE2, which is a chemical explosion, we observe that both DC and crack-like volume–increase MT solutions produce similar quality of waveform fits at VR 82%-85% (Figure 4b), which differs from common behavior of the explosion NSS. Usually CLVD sources with the vertical axis in compression provide similar quality of fits to explosion waveforms because an isotropic volume-increase MT solution and the vertically-oriented negative CLVD both have an isotropic Rayleigh wave excitation and no Love wave excitation (Ford *et al.*, 2009b, 2010, 2012). The very shallow depth of event TE2 (~ 9 m) causes the vertical dip-slip (DS) components of the GF, i.e., TDS, RDS, ZDS (Minson and Dreger, 2008), to be vanishingly small due to free-surface vanishing traction. This coupled with the fact that the source process also excited significant SH waves introduces spurious M and M components in the MT solution leading to the vertical dip-slip nature of best-fitting solutions near the DC region (Chiang *et al.*, 2016). This is further confirmed by inverting waveforms of event TE2 assuming a pure DC source, which returns a vertical dip-slip MT solution with M_W 1.41, VR 82.5 % and one of the fault plane solutions defined as ϕ, ζ and δ = 345°, 83° and 84°, respectively.

The best-fitting region of MT solutions for event TE3 (VR > 79%) covers a large area on the Hudson plot (Figure 4c), and therefore its source-type is poorly constrained by the NSS computed using low-frequency displacement waveforms alone. Its shape is different from that of a typical earthquake NSS (Ford *et al.*, 2010; Chiang *et al.*, 2014), which can be used to flag unusual events that warrant further investigation. Like many other events at The Geysers geothermal field the best-fitting full MT solutions of event TE3 show primarily positive isotropic components (Boyd *et al.*, 2015).

For comparison, we also compute the NSS for events TE1, TE2 and TE3 using the forward-modeling approach (e.g. Ford *et al.*, 2010) with a population of 80 million MT (i = 8) for each event (right panels in Figure 4). For the three events, we compare 1) the VR for the best-fitting randomly generated MT solution (VR_{MAX} in NSS Random plots in Figure 4), 2) the VR for the best-fitting MT solution obtained using our iterative damped LS inversion method (VR_{MAX} in NSS Inversion plots in Figure 4), and 3) the VR of the best-fitting full MT solution computed from time-domain full MT inversion of waveforms (Minson and Dreger, 2008). For the three events the best-fitting random NSS VR are 65.5%, 83.3% and 80.2%, respectively. For the NSS-inversion method, they are 68.2%, 85.4% and 80.2%, respectively. Best-fitting full MT solution (Nayak and Dreger, 2014; Chiang *et al.*, 2016; Boyd *et al.*, 2015) VR are 68.3%, 85.4% and 80.2%, respectively. The white circles and stars in Figure 4 show the respective best-fit solutions.

Even with 80 million MT, the best-fitting randomly generated MT solutions for events TE1 and TE2 fit their respective waveforms at VR lower than the VR of the best-fitting full MT solutions. The best values of VR recovered by the NSS computed using our iterative damped LS inversion approach are close to or the same VR as the best-fitting full MT solutions for all three events. We are also able to recover the source-type of the best-fitting full MT solution as seen in the overlap of the white star and the white circle on the NSS-Inversion plots for all three events. Overall, we observe that our inversion-based MT solutions produce better waveform fits than MT solutions from a population of randomly generated solutions by VR ~ 0–3% over a

substantial area on the Hudson plot for all three events.

Computing the NSS by estimating the best-fitting MT solution at each grid point on the Hudson plot also gives us the flexibility to make the grid coarser or finer depending on the purpose of our analysis since the number of grid points affects the computation time. We can also choose to evaluate only a portion of the source-type space. For example, we can compute the NSS only for source-types with positive sum of eigenvalues for the purpose of explosion monitoring. For event TE2, which has a total number of 7500 waveform samples (5 stations x 3 components x 500 samples per time series), a Fortran 90 code supported by LAPACK and Xcode running in Mac OS X 10.8.5 on a 3rd generation Intel 2.6 GHz i7-3720QM processor took little over 3 minutes in computing the NSS using the inversion-based approach. This opens up the possibility of near-real time source-type confidence analysis of seismic events after a general MT solution has been computed (and possibly reviewed by an analyst), using minimal computational resources. In comparison, the same computer took ~60 minutes for forward modeling waveforms with 80 million random MT.

The method to determine the NSS from a random population of eigenvectors and eigenvalues requires using a uniform distribution. Vavryčuk (2015) has shown that care is needed in the use of various MT norms applied to solution distributions in different source-type projections because a uniform distribution in one projection may not be uniform in a different projection. Moreover, distributions and uncertainties in MT elements are projected on source-type plots in complicated ways on different sections of the source-type plots (Vavryčuk, 2015). However, the NSS-inversion approach does not depend on any assumption on the distribution of MT eigenvalues. Instead the NSS-inversion systematically finds the best-fitting MT solution corresponding to each source-type (normalized eigenvalues) on a predefined source-type grid sufficiently covering the entire source-type space or a specific section under investigation, for any source-type projection.

3.1.6 Incorporating First Motions in the NSS

To better constrain the source radiation patterns of shallow explosion events, Ford *et al.* (2012) introduced the inclusion of teleseismic P-wave FM polarities in the NSS approach for better sampling of the entire focal sphere. Since waveforms used in MT inversion are usually of a low frequency nature, inclusion of P-wave FM polarities from regional or teleseismic distance stations provides independent high frequency information. Inversion of MT solutions from P-wave FM polarities using the derivative-based scheme that we have implemented for waveforms is problematic as the sign function is not differentiable at one point, and its derivatives are zero everywhere else in the domain. Therefore, we employ a continuous function to approximate the sign function.

P-wave FM polarity data, u_{FM}, which is -1 (down or dilation), 0 (zero) or +1 (up or compression), can be written as

$$u_{FM} = \frac{u_{0Z}}{|u_{0Z}|} \; for \; u_{0Z} \neq 0 \; and \; u_{FM} = 0 \; otherwise \quad (16)$$

where u_{0Z} is first arriving P-wave vertical component displacement amplitude that depends on MT elements, as well as azimuths and takeoff angles to individual stations (expression for far-

field P-wave radiation in equation 4.29 in Aki and Richards, 2002). u_{FM} can be approximated as

$$u_{FM} = \frac{u_{0Z}}{\sqrt{\epsilon + u_{0Z}^2}} \quad (17)$$

where ϵ is a small positive number. Figure 5 compares the sign function and its approximation with $\epsilon = 1\text{x}10^{-4}$ used in this study, which makes it continuous and differentiable. u_{0Z} can be expressed as

$$\mathbf{u_{0Z}} = \mathbf{G'm'} = \mathbf{G'} \, \mathbf{f}(m_0^2, \lambda, \mathbf{e_1}, \mathbf{e_2}, \mathbf{e_3}) = \mathbf{G'} \, \mathbf{g}(\lambda, a_1, a_2, a_3, b_1, b_2) \quad (18)$$

where $\mathbf{G'}$ is a function of takeoff angles and azimuths. Since we are considering only the polarities of the displacement, we can drop the moment scale factor, m_0^2, as a variable (or $\mathbf{g} = \mathbf{f}/m_0^2$). Therefore, for constant and known source-type λ, FM polarity information can be expressed as an approximate scalar function of five independent parameters. Similar to the procedure applied to waveforms, we can set up an iterative damped LS inversion scheme to estimate best-fitting values of $(a_1, a_2, a_3, b_1, b_2)$ for a given λ with $\mathbf{du_{T,R,Z}}$ and $\mathbf{P}$ in equations (10-14) replaced by $\mathbf{du_{FM}}$ and $\frac{\partial \mathbf{u_{FM}}}{\partial \mathbf{u_{0Z}}} \mathbf{G'} \begin{bmatrix} \frac{\partial \mathbf{g}}{\partial a_1} & \frac{\partial \mathbf{g}}{\partial a_2} & \frac{\partial \mathbf{g}}{\partial a_3} & \frac{\partial \mathbf{g}}{\partial b_1} & \frac{\partial \mathbf{g}}{\partial b_2} \end{bmatrix}$, respectively, with a different damping parameter k'.
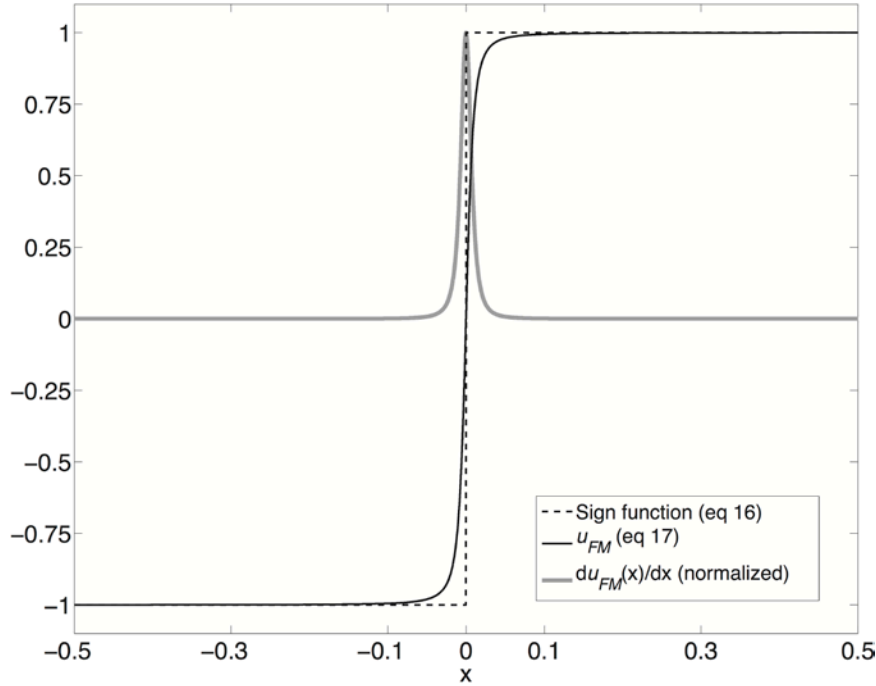
Figure 5. Figure showing the true sign function $sign(x)$ (equation 16), its approximation used in this study, $u_{FM}(x)$ (equation 17), and its normalized derivative $\frac{du_{FM}(x)}{dx}$, where $x = u_{0Z}$.

The derivatives, $\frac{\partial \mathbf{u_{FM}}}{\partial \mathbf{u_{0Z}}}$ are specific to each polarity data point. From Figure 5, it is obvious that the derivatives will be non-zero only for data points close to the P-wave nodes. Therefore,

for the FM polarity based inversion to proceed, there must be a sufficient amount of data, such that some data points are always close to zero and their derivatives are non-zero. So, this derivative-based scheme for inversion of MT solutions works best on large FM polarity data sets. The quantity of FM polarity data required will depend on the takeoff angles, azimuths and the source mechanism itself. We fixed the value of ϵ at 1E-4 from trial and error. Greater values of ϵ make the inversion more stable, but the derivatives are more approximate, making the final solution deviate from the true solution.

We use this inversion scheme to construct a first-motion polarity based NSS similar to that implemented for waveforms. We apply this scheme on FM polarities of event TE3 that has the largest amount of first-motion data among the three events (173 FM polarities collected from the stations of three networks in Northern California). For all events in this study, FM polarities were picked by analysts and assigned weights on a scale of 1 to 3 based on their quality. We also increase number of initial models for each λ-specific inversion to 100 and we proceed with the inversion with 30 best initial models after comparing the initial fits. From trial and error, $k' = $ 1E-2.

Prior to inversion of event TE3 polarity data, the inversion scheme was applied to synthetic P-wave FM polarity data sets for the 100 random MT of pure DC and pure CLVD that were used in the synthetic waveform tests. The azimuths and takeoff angles in event TE3 dataset were used to generate synthetic P-wave FM polarities. For both source-types, the inverted MT solutions are able to fit the polarity data perfectly (VR = 100%) for almost all (98 out of 100) random MT, while the final data VR for the remaining MT is > 98%. As there can be multiple similar eigenvectors or orientations that fit a polarity dataset equally, the MTVR corrected for m_0^2 varies from ~91% to 99.9%.

The results for event TE3 are shown in Figure 6. While the FM NSS constrains the mostly likely source-type to be close to DC or deviatoric, the maximum VR being only 51% indicating that there are no source-types that fit all of event TE3 FM data well. This might be indicative of a complicated initial rupture process, errors in FM picks, or possible errors in depth or takeoff angles. The misfit between observed and predicted polarities (beach-ball in Figure 6) is largely contributed by: (1) the anomalous polarities of Pn waves (polarities with steep equal takeoff angles in northeast and southeast quadrants) that are usually associated with uncertainties owing to their emergent nature; (2) and the section of the focal sphere towards south-southeast with both positive and negative polarities. Figure 6 also shows the NSS computed from forward modeling FM polarities using a population of 80 million randomly generated MT. Comparison of the two NSS plots in Figure 6 shows that our approximate inversion method works well on large FM polarity datasets. It can possibly be used along with FM polarity analysis software like FPFIT (Reasenberg and Oppenheimer, 1985) and HASH (Hardebeck and Shearer, 2002) to identify anomalous events in near-real time. The approximation to the sign function (equation 17) doesn't affect the values of VR as the approximation is used to only compute the derivatives whereas the actual sign function is used to forward model synthetic FM polarities to compute VR.
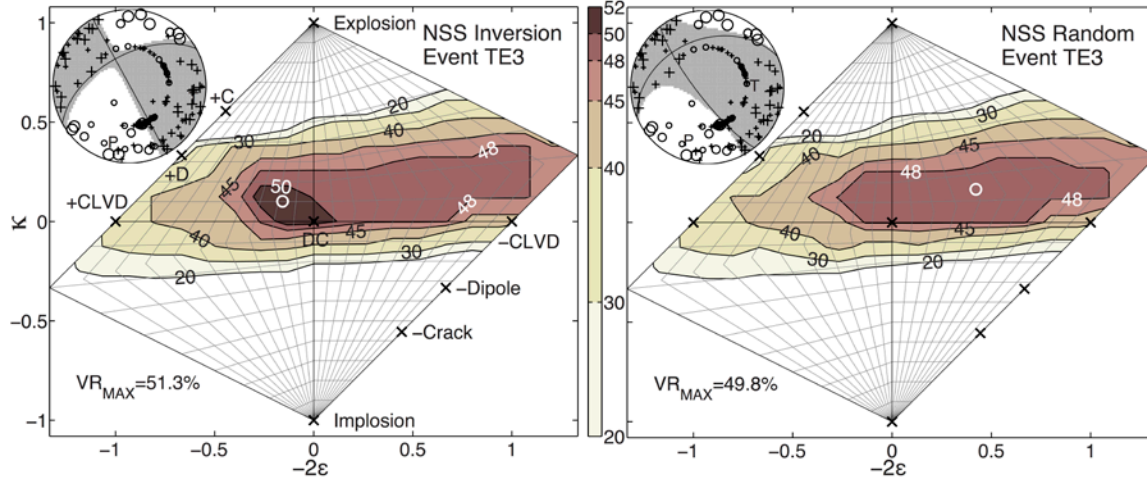
Figure 6. NSS of event TE3 using P-wave first motion polarities. '+Dipole' and '+Crack' are abbreviated to '+D' and '+C', respectively in the left panel. Beach-balls represent P-wave lower hemisphere radiation pattern predicted by MT solution corresponding to the maximum VR recovered by each NSS (white circle). In the beach-balls, black crosses and circles represent observed positive and negative P-wave FM polarities, respectively; the size of the polarity symbols is scaled by their quality weight (1, 2 or 3). 'P' and 'T' indicate pressure and Tension axes, respectively. Explanation of other symbols, shading and contours in NSS plots is same as in Figure 4. The color version of this figure is available only in the electronic edition.

In order to test if the inversion-based NSS approach works for a smaller quantity of FM polarity data, we randomly selected two sub-populations containing only 30 and 7 FM polarities, out of the original TE3 dataset containing 173 P-wave FM polarities. The analysis was repeated on the smaller datasets and the results are shown in Figure S5 available in the electronic supplement to Nayak and Dreger (2015). For both data subsets, our inversion scheme can compute an NSS nearly equivalent to one estimated by the forwarding modeling approach. Figure S5 also shows that ideally, a large quantity of FM polarity data is required to reliably constrain source-type of any seismic event. However, it is noted that the greatest benefit of our approach is the combination of waveforms and FM polarities, which as shown in previous studies (Ford *et al.*, 2012; Chiang *et al.*, 2014) only a few (3 to 10) FM polarity observations can greatly enhance the recovery of the source-type of events like nuclear explosions in sparse monitoring conditions.

3.1.7 Joint Waveform and First-Motion NSS-inversion

With the waveform and first-motion approaches it is now possible to perform a joint NSS-inversion of waveform and FM polarity data for events TE1, TE2 and TE3. The two types of data are first inverse weighted by their sum-of-squares to account for the difference between their amplitudes. We use 100 random initial models for each λ-specific inversion and test them against the data. 30 models with the best fits are then used as starting models in the inversion. The damping parameter from trial and error is set to 10. Figure 7 compares NSS computed using waveform and FM polarity data by joint inversion and forward modeling 80 million MT, which are very similar. For events TE1 and TE2 (Figure 7a,b), all FM polarities are positive and the

inclusion of FM polarities in the NSS constrains the best-fitting source type to be dominantly volume-increase. The maximum VR recovered from the NSS computed using the joint inversion of waveforms and FM polarities for events TE1 and TE2 (84.0% and 91.9%, respectively), are very close to the mean of separate maximum VR values for FM polarity data (100% for both events) and waveforms (68.2% and 85.4%, respectively) which demonstrates the success of the joint inversion scheme proposed in this study. For event TE3 (Figure 7c), the maximum VR recovered from NSS computed using the joint inversion of waveforms and FM polarities, 59.4%, is less than mean of maximum VR values (65.8%) for separate waveform (80.2%) and FM polarity (51.3%) NSS. Assuming NSS converged to the best-fitting solution, this suggests that MT solutions or source-types that best fit the low frequency displacement waveforms and high-frequency P-wave FM polarities separately are not in perfect agreement with each other. While FM polarities reflect the source mechanism at the beginning of the source-time history of the earthquake, low frequency waveforms reflect the average source mechanism of the event under a point source assumption in time and space, which might lead to disagreement between best-fitting MT solutions for the two data-types in case of complex events. For example, initial radiated energy in explosions is expected to be isotropic and explosive leading to all compressive FM polarities whereas tectonic release during the later part of the time history might lead to deviatoric components in the point source MT solution obtained from waveform inversion. Man-made explosions are suitable for joint analysis of waveforms and FM polarity data, because the initial mechanism must be explosive and volume-increase, leading to positive first motions irrespective of the nature of secondary mechanism responsible for non-isotropic components that are commonly found in MT solutions of explosions. For events in geothermal and volcanic environments, source-time functions could be complex and composite mechanisms could be diverse, and therefore, it might be difficult to reconcile FM polarity data with composite point source MT solutions. It is therefore expected that joint inversion of polarity data and low-frequency waveforms works best for small events with short duration impulsive source-time functions. Nevertheless, the analysis can identify potential discrepancies between the two data sets thereby raising caution and a need for further analysis.

For all events and all types of NSS, the maximum VR as well the size of the region of best-fitting MT solutions (highest contour levels in Figures 4, 6 and 7) recovered by the NSS-inversion approach are either same as or greater than those recovered by forward modeling 80 million random MT. For the waveform-only NSS the VR recovered by the NSS-inversion approach are the either same as or greater than those recovered by forward modeling random MT for almost all source-types (Figure 4). For the NSS computed using waveform and polarity data simultaneously, we recognize there are few eigenvalue sets for which VR values of the best-fitting MT solutions recovered by our inversion method are not as good as those from the large population of random MT solutions (for example, see outermost contours of Figure 7b). These differences are possibly caused by the inability of the inversion to converge further towards the true solutions on account of the derivatives of polarity data having near-zero values (see Figure 5 and its explanation earlier in this section). Comparing the results of multiple runs of joint waveform and FM polarity NSS inversion, we have observed that while the shape of VR contours in NSS are similar, the maximum VR recovered can vary by 1-2%. Further work is required to design an improved inversion scheme with a better way of incorporating polarities that converges to the true global VR maximum at each instance. The computation of NSS by joint inversion of waveforms and polarity data also takes 2-4 times longer than the computation when inverting waveforms alone. However, this increase in computation time can be remedied

by not inverting at source-type grid points where the waveform-only VR is less than a particular threshold (for example, 40%).
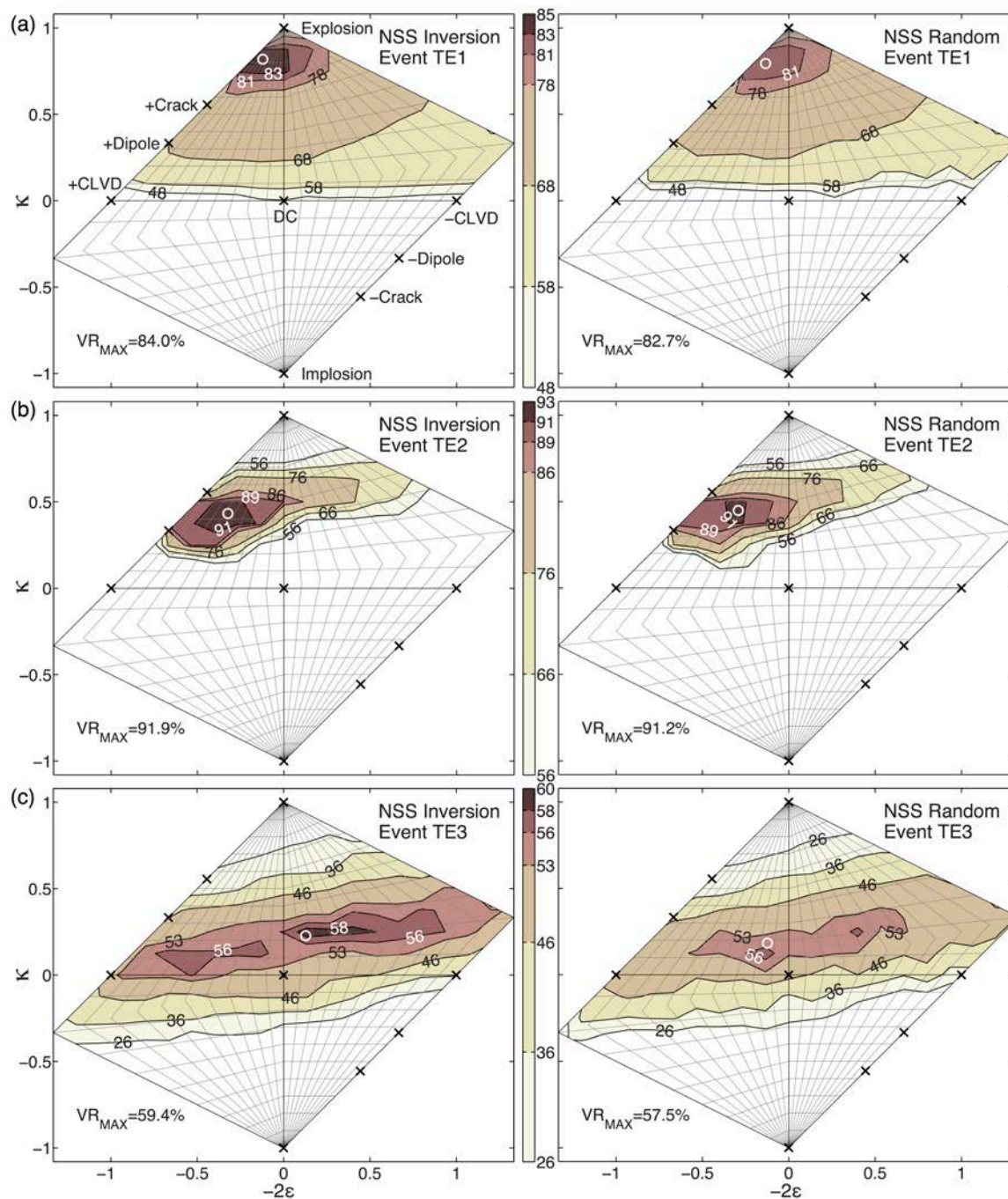
Figure 7. NSS of the three events using both low-frequency displacement waveforms and FM polarity data: (a) TE1, (b) TE2 and (c) TE3. Explanation of symbols, shading and contours is same as in Figure 4. The color version of this figure is available only in the electronic edition.

3.1.8 Conclusions

In this study, we define elements of the general MT in terms of: (1) its normalized eigenvalues that characterize its source-type, (2) a seismic moment scale factor that scales the normalized eigenvalues to appropriate size or scalar moment, and (3) its eigenvectors that specify its orientation. We utilize this formulation to implement an iterative damped LS inversion scheme to invert displacement waveforms for best fitting eigenvectors and the moment scale factor for specific eigenvalues, which results in the best-fitting MT solution for a specific source-type. However, the expressions are general and can be used with other appropriate inversion techniques as well. Our technique is successfully demonstrated by estimating best fitting MT solutions for synthetic data assuming various source types: cracks, explosion and DC. For low frequency displacement waveforms of the three example events, we find the NSS computed using the inversion approach to be faster and more accurate by VR ~ 0-3% compared to NSS computed by forward modeling 80 million randomly generated MT. To better constrain the source-types of these seismic events, we employ an approximation of the sign function in order to invert FM polarity data along with displacement waveforms using our derivative-based inversion scheme. We find that our inversion method is more successful than the random search approach in recovering the MT solution with the maximum VR as well as the region of best-fitting MT solutions or source-types for NSS computed using low-frequency displacement waveforms and P-wave FM polarities both separately and jointly. The inclusion of P-wave first-motion observations with long-period waveforms narrows the range of possible MT solutions in source-type space leading to improved source-type discrimination. It would be straightforward to also incorporate body wave amplitude ratios, and such a combination of data types could be useful in cases where individual data sets are very sparse, such as for small magnitude induced earthquakes.

3.2 Analysis of the Effects of Vanishing Traction for Shallowly Buried Sources

A potential issue for moment tensor inversion of shallow seismic sources is that some moment tensor components have vanishing amplitudes at the free surface, which can result in bias in the moment tensor solution. The effects of the free-surface on the stability of the moment tensor method becomes important as we continue to investigate and improve the capabilities of regional full moment tensor inversion for source-type identification and discrimination. It is important to understand these free surface effects on discriminating shallow explosive sources for nuclear monitoring purposes. It may also be important in natural systems that have shallow seismicity such as volcanoes and geothermal systems. In this study, we examine the effects of the free surface on the moment tensor via synthetic testing, and apply the moment tensor based discrimination method to the HUMMING ALBATROSS quarry blasts. These shallow chemical explosions at approximately 10 m depth and recorded up to several kilometers distance represent rather severe source-station geometry in terms of vanishing traction issues. We show that the method is capable of recovering a predominantly explosive source mechanism, and the combined waveform and first motion method enables the unique discrimination of these events. Recovering the correct yield using seismic moment estimates from moment tensor inversion remains challenging but we can begin to put error bounds on our moment estimates using the NSS technique.

A preliminary report of this section was provided in the final report for FA9453-10-C-0263. It is included here to report on the final results of the effort, which have been submitted for publication in the Bulletin of the Seismological Society of America (Chiang et al., 2016), and at the time of writing this report is accepted pending minor revision.

3.2.1 Introduction

Waveform inversion to determine the seismic moment tensor is now a standard method for determining the source mechanism of natural and man-made seismicity, and can identify, or discriminate different types of seismic sources. Such source-type identification is important for better understanding the physical processes of explosions as well as other man-made seismicity and earthquakes from geothermal Guilhem et al., 2014), and volcanic environments (Templeton and Dreger, 2006; Minson et al., 2007) and oil and gas operations (McNamara et al., 2015). For the nuclear explosion discrimination problem the uncertainty in a given solution is as important as the best fitting parameters and it is therefore necessary to fully understand and model possible bias that can result in such inversions. A potential issue for shallow seismic sources that are effectively at the free surface is that as the traction vanishes the associated vertical dip-slip (DS) Green's functions have vanishing amplitudes (Julian et al., 1998, Stevens and Murphy, 2001), which in turn can result in the indeterminacy of the M_{xz} and M_{yz} components of the moment tensor and therefore bias in the moment tensor solution. The free-surface effect was noted in a study on fundamental Love and Rayleigh waves for nuclear explosions and associated tectonic release (Given and Mellman, 1986). The effects of the free surface on the stability of the moment tensor becomes important as we continue to investigate and improve the capabilities of regional full waveform moment tensor inversion for source-type identification and discrimination. It is important to understand its effects for discriminating shallow explosive sources for nuclear

monitoring, but could also be important in natural systems that have shallow seismicity such as volcanic environments and geothermal systems, and other manmade shallow seismicity related to anthropogenic activities such as hydraulic fracturing and mining.

To investigate the potential issues that could arise in the estimation of moment tensors for shallow sources, we perform a series of synthetic tests to document and understand the effects of free surface vanishing traction (FSVT) on the total seismic moment, isotropic seismic moment and the source mechanism. We evaluate the sensitivity of the moment tensor solutions as a function of source depth, data quality, frequency and velocity model. Based on what we learn from the synthetic studies, we applied the moment tensor method to the HUMMING ALBATROSS quarry blast events, this is an excellent dataset in terms of understanding the effects of FSVT and evaluating the discrimination capabilities of the moment tensor method as a function of source depth and frequency. These small chemical explosions are approximately 10 m deep and are recorded at up to several km distances. Therefore the data represent rather severe source-station geometry in terms of vanishing traction issues. We show that the combined method utilizing both complete seismic waveforms and P-wave first motion polarities is able to obtain robust full moment tensor solutions that are comprised predominantly by an isotropic or explosive component. However, unlike the synthetic studies, yield estimation using the real quarry blast moment tensor inversion results remains challenging.

3.2.2 Methods

The seismic moment tensor consists of nine force couples that represent the equivalent body forces for seismic sources of different geometries (Jost and Herrmann, 1989) that due to conservation of angular momentum reduce to six independent couples and dipoles. The data (e.g. displacement waveforms) are represented by the convolution of Green's functions for a given Earth model, source term and the moment tensor elements. We obtain the individual moment tensor elements by inverting the 3-component, complete waveform data using a time domain, generalized least square inversion (Minson and Dreger, 2008), and the goodness of fit between the data and synthetics is measured by the variance reduction (VR):

$$\text{VR} = \left(1 - \frac{\sum_i w_i(d_i - s_i)^2}{\sum_i w_i d_i^2}\right) \times 100,$$ *(19)*

where d is the data, s is the synthetic waveforms and w is the distance weighting at each station i. Because the data are linear combinations of the Green's functions weighted by their associated moment tensor elements, one major source of error in the inverted moment tensor solution comes from the assumed velocity model. A well-calibrated velocity model is important to obtain robust estimates of the source parameters. For HUMMING ALBATROSS we used the 1D velocity model by Saikia et al. (1990) computed from Rg wave dispersion, and calculated the Green's functions using frequency-wavenumber integration (Wang and Herrmann, 1980; Herrmann and Wang, 1985; Herrmann, 2013). The inversion method also allows for small time shifts between the data and Green's functions to compensate for uncertainties in origin time, location, and velocity structure. To properly account for non-double-couple radiation we used the Bowers and Hudson (1999) formulation to calculate the moment magnitude.

To assess the full uncertainties in the moment tensor inversion and avoid the need to decide on a particular moment tensor decomposition scheme, we examine the moment tensor solution in terms of the maximum fit surface called Network Sensitivity Solutions [NSS] (Ford et

al., 2010). The NSS presents the goodness of fit between data and a suite of moment tensor solutions for a given station configuration, Earth model, and frequency band. We contoured the populations of best-fitting moment tensor solutions that have VR equal and above a certain threshold. In descending order, the contours map out the solutions that have VRs of 98%, 95%, 90%, 80%, 70%, 60%, and 50% of the maximum VR in the NSS population. From the NSS of a given event we can determine whether or not the best-fitting full moment tensor solution from the inversion is well resolved to make useful interpretations about the source. The maximum fit surface is parameterized and represented in the source-type space (Hudson et al, 1989; Tape and Tape, 2012a; Tape and Tape, 2012b; Vavryčuk, 2015). In essence the source-type diagram is a graphical representation of the full moment tensor eigenvalues. The source-type diagram has two key parameters γ and δ, which are the longitude and latitude of a lune on the unit sphere (Tape and Tape, 2012a; Tape and Tape, 2012b):

$$\tan\gamma = \frac{-\lambda_1 + 2\lambda_2 + \lambda_3}{\sqrt{3}(\lambda_1 - \lambda_3)}, \tag{20}$$

$$\cos\beta = \frac{\lambda_1 + \lambda_2 + \lambda_3}{\sqrt{3(\lambda_1^2 + \lambda_2^2 + \lambda_3^2)}}, \tag{21}$$

$$\delta = \frac{\pi}{2} - \beta. \tag{22}$$

β is the colatitude and λ_{1-3} are the eigenvalues of the full seismic moment tensor where $\lambda_1 \geq \lambda_2 \geq \lambda_3$. Equation (20) measures the deviation from a pure shear dislocation and equation (21) and (3.2.4) describes the volume change. In this convention when $\delta = 0$ (no volume change): $\gamma = 0$ describes a pure double-couple (DC) source and ±30 describes a pure compensated-linear-vector-dipole (CLVD) source; and $\gamma = 0$ and $\delta = \pm90$ represents a spherical explosion (+V) and implosion (-V), respectively. Understanding the relative contributions of the different moment tensor elements provides insights into the complex source processes of explosions as well as other seismic events. This representation of the seismic source has been shown to result in separate populations for explosions, underground cavity collapse and earthquakes (Ford et al., 2009a; Ford et al., 2009b; Dreger et al., 2008; Ford et al., 2008; Chiang et al., 2014) enabling discrimination capability.

Instead of the original forward-modeling approach by Ford et al. (2010) we implemented the damped least square inversion scheme by Nayak and Dreger (2015) to compute the NSS. This method significantly reduces the computation time, and recovers a true maximum fit surface in the source-type space. In addition to long period waveform data we include P-wave first motion polarities in the NSS calculations as additional constraints (Ford et al., 2012; Guilhem at al., 2014; Chiang et al., 2014). The damped least square inversion finds the moment tensor solutions that best fit both the complete waveform data and the P-wave first motion polarities. Similar to comparing synthetic waveforms to data, we compare the theoretical P-wave first motions against the observed polarities. We assign -1 for downward motion and +1 for upward motion, and each observed polarity is weighted by the quality of the pick. The first motion VR is calculated as:

$$VR = \left(1 - \frac{\sum w_i \left(Pol_{obs} - Pol_{synth}\right)^2}{\sum w_i Pol_{obs}^2}\right) \times 100. \tag{23}$$

The final combined VR is computed by weighing the two data sets equally. Incorporating the first motion data proves to be a powerful tool in reducing solution uncertainties. Constraints from first motion can reduce uncertainties due to the theoretical ISO-CLVD (Isotropic-CLVD) tradeoff (Ford et al., 2012; Chiang et al., 2014), sparse station coverage (Chiang et al., 2014), illuminate possible complexities in earthquake ruptures in geothermal environments (Guilhem et al., 2014), and as illustrated later in this study, free surface effects at shallow depths. We find that the additional polarity constraints assist by uniquely discriminating the events as predominantly explosive and greatly enhance the discriminatory power of the moment tensor-based method.

3.2.3 Free-Surface Vanishing Traction

We generate the ten fundamental Green's functions at a distance of 100-km from the source and with source depths ranging from 0.2 to 1.2 km. We apply an acausal bandpass Butterworth filter at 10 to 50 seconds to filter the Green's functions. As shown in Figure 8a we see a strong source depth dependency on the vertical dip-slip (DS) fundamental Green's functions associated with the M_{xz} and M_{yz} elements for all three components: vertical (ZDS), radial (RDS) and transverse (TDS) in which there is a systematic reduction in displacement amplitude with decreasing source depth. The averaged Fourier spectral amplitude shows a linear relationship between the source depth and DS waveform amplitudes (Fig. 8b). In contrast, the vertical strike-slip Green's functions for all three components (ZSS, RSS and TSS) and the explosion Green's functions for the vertical and radial components (ZEX, REX) show little to no variation in amplitude and waveform with respect to decreasing source depth. The vertical and radial 45-degree dip-slip Green's functions (ZDD and RDD) show variations in amplitude as well due to the constructive and destructive interference of waves interacting with the free surface. While the wave interference appears minor in the 10 to 50 second period passband (Fig. 8a) it is more pronounced in the unfiltered displacement Green's functions.
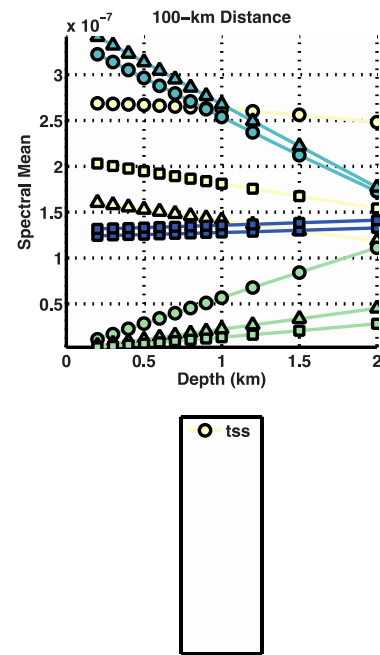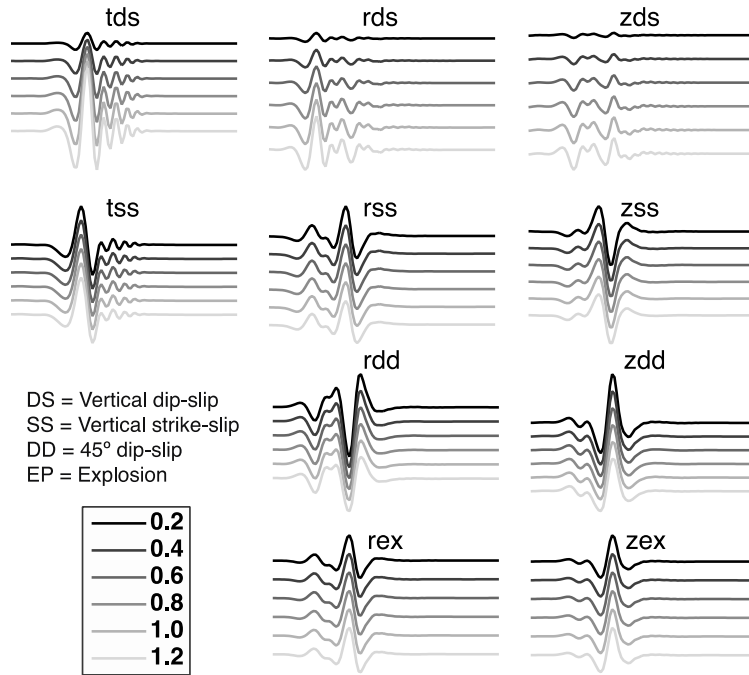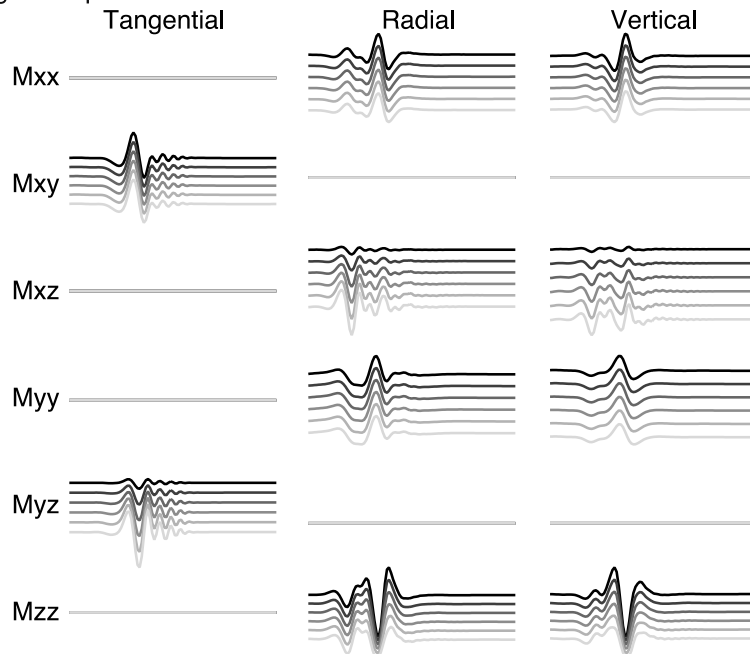
Figure 8. a) Green's functions (GF) computed using the Song et al., (1996) 1D western U.S. velocity model. GF are in displacement and filtered between 10-50 second period. The traces for each component, from top to bottom, are at 200, 400, 600, 800, 1000, and 1200 m source depths. b) Averaged spectral displacement amplitudes between 10 to 50 seconds for the ten fundamental Green's functions. c) Moment tensor elements computed using the same velocity model and filtered between 10-50 second period.

Since traction perpendicular to the vertical vanishes at the free surface, the inversion may not resolve the M_{xz} and M_{yz}, as well as the isotropic components M_{xx}, M_{yy}, M_{zz} of the moment tensor. It is important to note however that while there are strong effects on amplitude, the waveforms remain similar and there is little effect on the phase of the waveforms of these components. The systematic behavior of the Green's function suggests that it may be possible to scale the isotropic moment (M_{ISO}) to recover the correct moment, enabling a more robust estimate of the explosive yield. But because the ability to resolve seismic waveforms at the free surface depends on the velocity model, frequency band, station configuration and background noise level, it is necessary to understand the behavior of the moment tensor inversion for each particular monitoring scenario in order to correct for bias in the seismic moment. Poor station coverage and low signal-to-noise ratio (SNR) will decrease the method's ability to resolve the observed waveforms.

In the synthetic study we examine the ability to recover the correct moment tensor elements by generating a suite of velocity models derived from a 1D western U.S. velocity reference model (Song et al., 1996). We choose this particular model as a reference because it was used to model the NTS explosions in Ford et al. (2009). We generated the suite of models by splitting the top 2.5-km thick layer in the reference model into two separate layers. We systematically adjust the thickness and velocity of the two new layers (Figure 9), but constrain the perturbations of the two parameters (velocity and layer thickness) by maintaining the same vertical travel time as the reference model. The reason to maintain the same vertical travel time is to generate different but comparable velocity models and to minimize travel-time differences. For each 1D model, we generate displacement Green's functions at regional distances between 100 and 400 km with source depths ranging from 0.2 to 3.5 km. Using the same set of Green's functions we generate two types of synthetic data with different source mechanisms: 1) a pure explosion case (EXP) and 2) a composite source case (DC and EXP) with a DC to EXP ratio of 2:3. We compute the synthetic data following the expressions from Minson and Dreger (2008), and add random Gaussian white noise. We scale the amplitude of the random noise for a given SNR using the following equation:

$$SNR = 20 \log_{10}(\frac{RMS_{signal}}{C_{noise}RMS_{noise}}) . \tag{24}$$

The scaling factor C_{noise} is calculated for a given SNR using the root mean squared (RMS) amplitudes of the signal and noise, then the noise-included data and Green's functions are bandpass-filtered between 10 to 50 seconds using an acausal Butterworth filter. To model after real-life monitoring capabilities we use an SNR of 10 but also tested different SNRs. We implemented a semi-ideal four-station coverage for the moment tensor inversion, consisting of source-to-receiver distances at 100, 200, 300 and 400 km, and distributed in semi-regular azimuths.
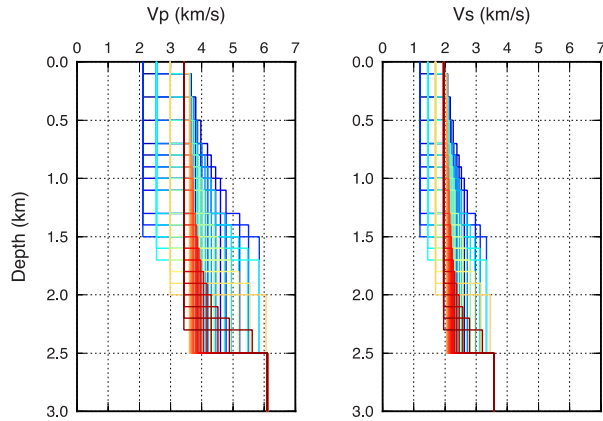
Figure 9. Velocity models derived from the Song et al. (1996) 1D model by keeping the top 2.5-km vertical travel time constant. The model parameters are the same below 2.5-km depth.

In this test we keep the source depths of the synthetic data and the Green's functions used in the inversion the same to isolate the effect of only vanishing traction for shallow depth of burial. Of the 59 velocity models tested the full moment tensor inversion successfully recovers the correct mechanism for both the pure explosion case and the composite case over the targeted depth range (< 1 km) for nuclear explosions, as well as at deeper depths. Given the same filter parameters and station configuration, models that have a thick continuous layer generally have larger deviations in the moment estimates, whereas the more gradient-like models show little to no change in their moment estimates (Figure 10). At the shallowest depths (< 0.5 km), for the pure explosion case the M_{ISO} estimates all fall within about 10% of the input values (Figure 10a), whereas the total moment varies even less. The composite case exhibits greater deviations from the input value at the shallowest source depths, however all moment estimates are within about 20% of the input values (Figure 10b). In general the seismic moment estimates approach the correct value as the source depth increases. The M_{zz} component is not as well constrained, thus affecting the method's ability to resolve the M_{ISO}. In most cases the FSVT has little effect on recovering the correct mechanism for models with a shallow velocity gradient. However, as the noise level increases the bias in the seismic moment and mechanism also increases. The key observation from the synthetic tests is that the bias in the recovered moment and source mechanism of very shallow sources depends on various factors, including the velocity model.
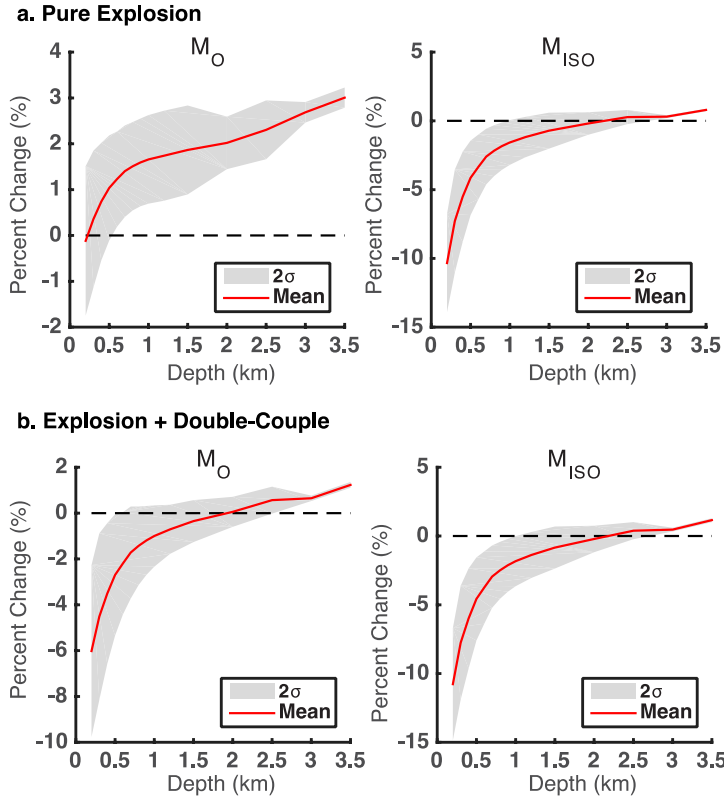
Figure 10. Isotropic moment and total seismic moment percent change for a) a pure explosion source and b) a composite source, plotted as a function of source depth. The average value of all 59 models is the solid red line, the shaded region is 2-sigma from the mean, and the dashed line represents no deviation from the input seismic moments.

In practice when we perform moment tensor inversions the source depth is also tested because we do not know the true source depth. Thus we also looked at synthetic comparisons where we fixed the source depths to 0.2, 0.5, 1.5 and 3.0 km and for each depth the full suite of Green's function depths are tested. The results for both source types are shown in Figure 11. In this synthetic test the deviation from the true seismic moment is much greater due to errors from incorrect source depth, the percent change in total and isotropic moment decrease as the Green's function depths approach the correct value. For the four source depths we examined, the mean percent changes in moments are similar but the spreads are different. For example when source depth is at 1.5 km the change in isotropic moment away from the true source depth encompasses a much wider range compare to other tested source depths. The change in VR is most prominent at source depth of 3.0 km because a boundary layer exists at 2.5 km for all the velocity models.
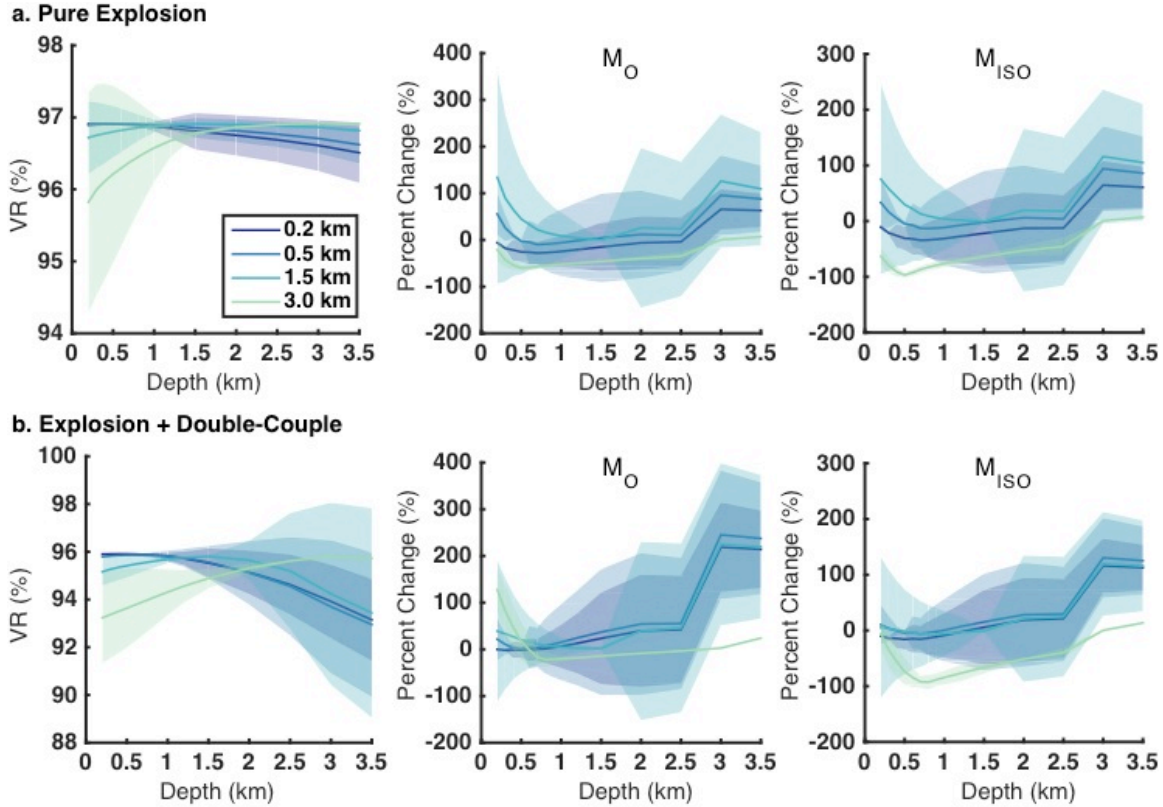
Figure 11. Fixed Source Depth Sensitivity Analysis. Source depth is fixed while we tested the full suite of Green's function depths (x-axis), and compare the VR, total moment percent change and isotropic moment percent change as a function of varying Green's function depth for (a) a pure explosion source and (b) a composite source. Similarly, the solid lines are the average values of all 59 models and the shaded regions are 2-sigma from the mean. The lines and shaded regions are color-coded according to source depths (data).

3.2.4 HUMMING ALBATROSS

The synthetic tests show although the loss of traction at the free surface can affect the method's ability to resolve the moment at shallow depths, the impact on the recoverability of the source mechanism is much less. We evaluate the performance of the moment tensor method using the data from the HUMMING ALBATROSS series. The data sets consist of twenty-six broadband, strong motion and short-period seismic recordings (Figure 12). The chemical explosions are denoted at very shallow depths (< 20 m) and recorded at stations up to the several kilometers. We apply the moment tensor based discrimination method to three of the five chemical explosions, the two smallest events in the series have poor SNR below 3 Hz and we cannot estimate the source parameters with high confidence. Weston Geophysical Corp. provided the instrument corrected velocity and acceleration data for HUMMING ALBATROSS, and we prepare the velocity waveforms for source analysis by rotating the horizontal recordings to radial and transverse components, and bandpass-filtered the data and Green's functions with an acausal Butterworth filter. Depending on the instrument response and data quality the bandpass filter applied to each station ranges between 0.4 to 1.25 seconds. Table 2 lists the source depth and filter corners used, and the moment magnitude (M_W), M_{ISO} and waveform fits (VR) from time domain full moment tensor inversions.
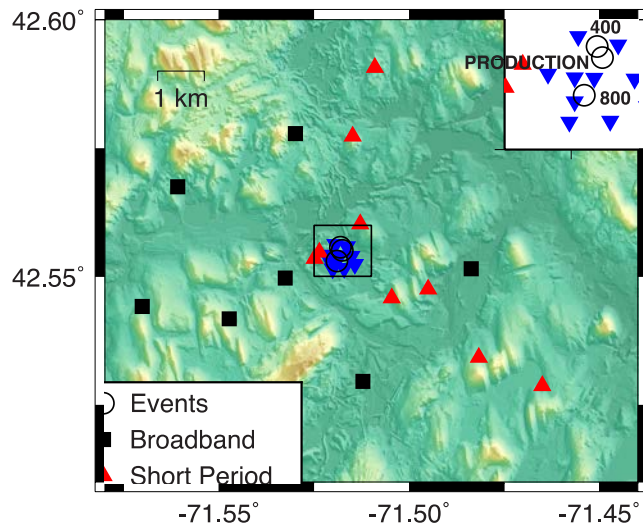
Figure 12. Event and station locations for the HUMMING ALBATROSS series. The seismic array includes broadband instruments (square), short period sensors (triangle) and accelerometers (inverted triangle). We looked at three of the five chemical explosions (circle) and the background colors represent the local topography where green is lower elevation.

Table 2. Moment Tensor Solution and Yield

Event	Centroid Depth (m)	Filter (s)	M_W	M_{ISO} (dyne-cm)	VR (%)	Estimated Yield (tons)	Yield (tons)
Production	Varied	0.5 – 1.25	2.5	3.24747×10^{19}	70	28.943	10.189
800	9	0.5 – 0.83	1.9	3.36495×10^{18}	72	2.999	0.394
400	11	0.4 – 1	1.4	9.91028×10^{17}	64	0.883	0.201

Following the results of Ford et al. (2012) and Chiang et al. (2014) we utilize full waveform data from broadband and/or short period stations for the time domain waveform inversion, and include both waveform and P-wave first motion polarities from all twenty-six stations into our source-type uncertainty analysis. We present results from moment tensor sensitivity analysis both as a function of depth and frequency for the largest, delayed-fire production shot.

The time-domain moment tensor inversion yield similar results for all three explosions in which the full moment tensor solutions all have relatively large isotropic components that are approximately between 40 to 50 percent of the total seismic moment, and the deviatoric inversions all result in vertical dip-slip-like mechanisms (Figure 13). The deviatoric solutions are thus dominated by the Mxz and Myz components, which as shown in Figure 8c, the TDS, RDS and ZDS Green's functions, show a marked reduction in amplitude with decreasing source depth. An example of the waveform fits and moment tensor solutions for the production shot is shown in Figure 14. All three explosions have strong shear wave energy in the transverse component, and many of them have amplitudes comparable to Rayleigh waves in the vertical component. We avoid using stations in the direction of the free face (quarry cliff) for the production shot because of spallation at the cliff face. For shot 800 we tried a combination of stations with and without

those in the direction of the free face and found the moment tensor solutions to be very similar.
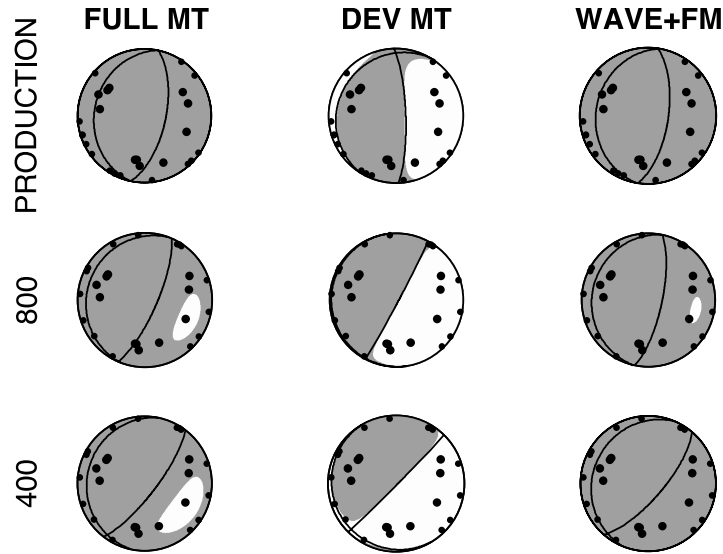
Figure 13. HUMMING ALBATROSS moment tensor solutions from time domain full and deviatoric inversion, and best solution from combined waveform and P-wave first motion (filled circle) Network Sensitivity Solutions. All polarities are up.

The production shot source parameter uncertainties using only seismic waveforms show the best-fitting mechanisms are mostly isotropic (Figure 15a). The source parameters are well constrained for solutions with VRs equal and above 95% of the maximum VR, but if we relax the threshold down to 90% of the maximum VR the population of well-fitted solutions extends across the DC/deviatoric line. Previous NSS studies of nuclear explosions have shown tradeoffs between ISO (+V) and –CLVD mechanisms, but generally not between ISO and DC mechanisms (Ford et al., 2012; Chiang et al., 2014). A combination of strong Love waves and free-surface effects most likely contributed to this apparent ISO-DC tradeoff and it is especially pronounced for the two smaller shots. To increase the confidence in our moment tensor solutions we bring in constraints from P-wave first motion polarities. We have excellent azimuthal coverage for the first motion observations that sampled the entire focal sphere, significantly reducing the NSS to a predominantly explosive mechanism (Figure 15b). The best solutions from the combined NSS are similar to the solutions from the waveform-only inversions (Figure 13) Moment tensor solutions that deviate away from a theoretical opening crack do not fit the observed polarities. NSSs for shots 800 and 400 show similar behaviors, namely the ISO-DC tradeoff using only waveforms, and a well-constrained solution when combining both waveform (dominated by surface waves) and P-wave first motion polarities. We also present an example of a first motion only NSS (Figure 15c), the maximum fit surface using only polarity data is extensive, therefore first motions only are not sufficient for event source-type discrimination.
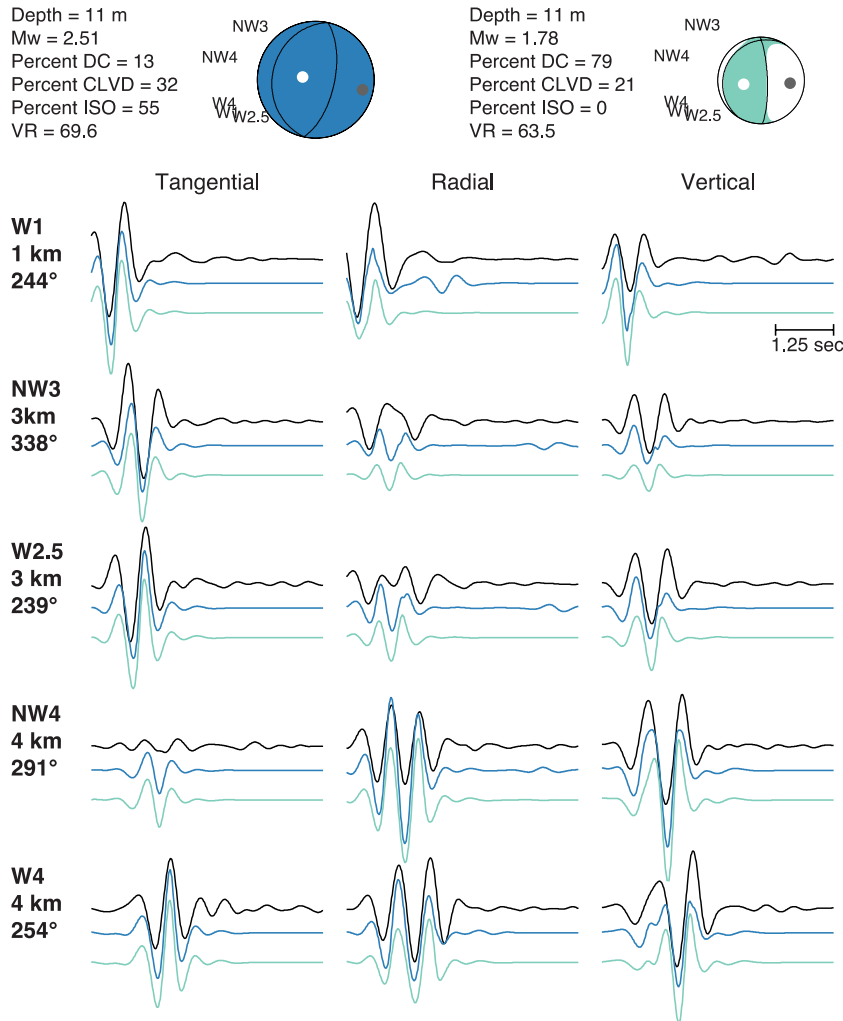
Figure 14. Production shot focal mechanisms and waveform fits from full and deviatoric moment tensor inversions.

Given the frequency band and source-receiver distance, the moment tensor inversion is not very sensitive to source depths shallower than ~100 m. We estimate source depth sensitivity by looking at the VR as a function of source depth and observe that the deviatoric VR drops sharply starting around 100 m, whereas the full VR shows a more gradual decrease in VR. If we have no prior knowledge on source depth, the sensitivity analysis shows we can constrain the depth to be shallower than ~100 m, indicative of possible manmade seismicity since natural earthquakes rarely occur at these depths. Although we do not have much sensitivity at the very shallow depths, the mechanisms remain stable and predominantly explosive at the borehole depths (Figure 16a-b). We start to see a tradeoff between the mechanism and incorrect source depth at around 100 m for the production shot, and around 50 m for 800 and 400; however the combined waveform and first motion inversion eliminates this tradeoff. Because we know the depth of the borehole where the explosions are detonated, we focus on the behavior of seismic moment at depths less than and equal to 20 m. Due to free surface effects the total and isotropic moment increases as source depth decreases (Figure 16c-d), and the increases in seismic moments are controlled by changes in the M_{zz} and M_{yz} components (Figure 16d), components that we anticipated to be strongly influenced by the free surface. The behavior of the moment

tensor solution as a function of depth is similar for shots 800 and 400, although the free surface effects are more pronounced at the shallowest depths, where the full moment tensor solutions become vertical dip-slip due to a greater increase in moment from the M_{yz} component.
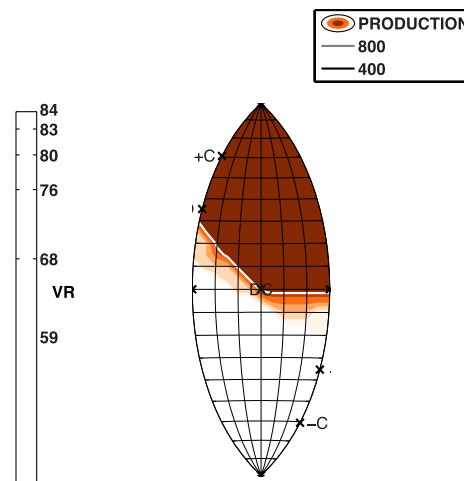
Figure 15. Network Sensitivity Solutions (NSS) using a) waveforms, b) waveform and first motions, and c) first motions. Best MT solutions from time-domain inversion (plus) and NSS (circle) are plotted in a) and b). Production shot NSS are plotted as shaded contours, and highlighted contours are populations of solutions with normalized VR of 95% relative to the maximum.

The Earth becomes very heterogeneous at high frequencies where the smoothed 1D model is no longer adequate in characterizing the complexities in high frequency wave propagation between the source and receiver. Therefore the reason for utilizing low frequency waveform data is to minimize the bias from unaccounted velocity structures. However, the challenge for moment tensor inversion at these very shallow depths for the HUMMING ALBATROSS data is that the free surface effect not only increases with decreasing source depth but also at longer periods. The production shot has relatively good SNR at periods up to 2.5 seconds, but if we fix the source depth to 11 m and look at the free surface effects on the inversion as a function of filter passband we see the solutions become vertical dip-slip at longer periods (Figure 17a-b). The total moment increases (Figure 17c) as we go towards longer periods due to rapidly increasing contributions from the M_{xz} and M_{yz} components (Figure 17d). Hence finding the optimal filter passband that minimizes both the effects of the velocity structure at high frequencies, and the free surface at low frequencies is especially important and potentially challenging for moment tensor analysis of shallow sources.
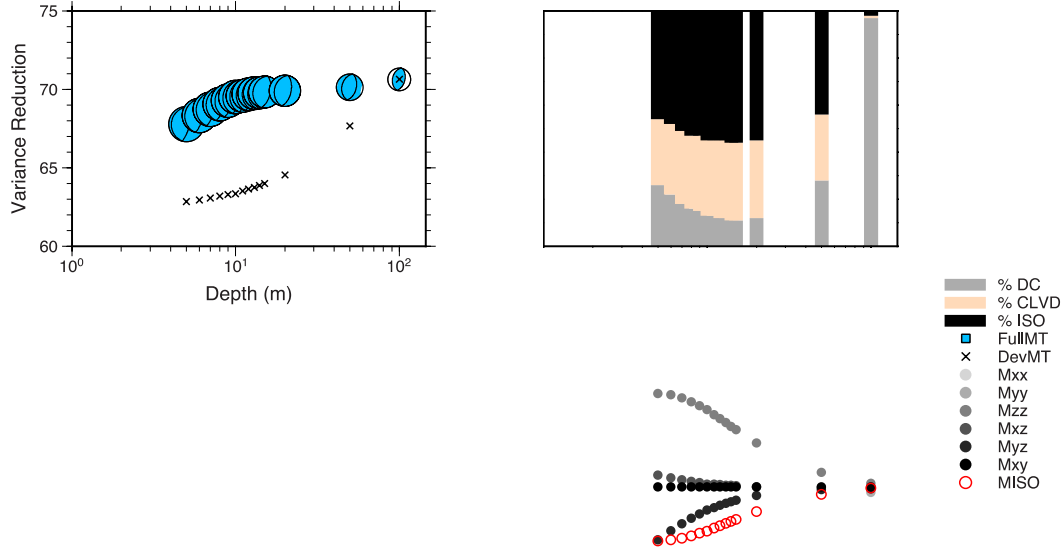
Figure 16. Production shot moment tensor solutions as a function source depth, using only waveform data. a) VR from full moment tensor inversion (focal mechanism) and deviatoric moment tensor inversion (cross), b) full moment tensor decomposition. Shaded bars are the percent DC, CLVD and ISO components, c) total moment from full inversion (square) and deviatoric inversion (cross), and d) moment tensor elements (filled circles) and isotropic moment (open circle).
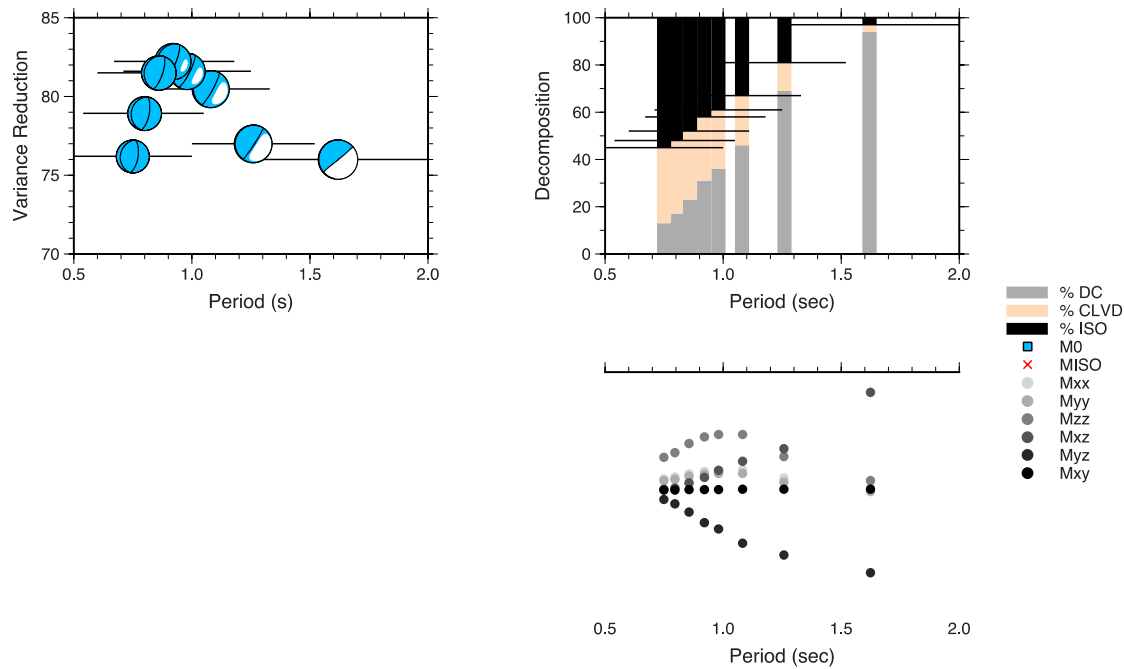
Figure 17. Production shot full moment tensor solutions as a function of filter passband, using only waveform data. a) VR and focal mechanism), b) decomposition, c) total moment (square) and isotropic moment (cross), and d) moment tensor elements (filled circle). Horizontal lines in a)-c) specify the filter passband used for each inversion at 11 m depth.

3.2.5 Yield Estimates

Empirically the magnitude-yield relationship can be described by the following equation:

$$M = A \log_{10} Y + C, \tag{25}$$

where M is the seismic magnitude, Y is the yield in kilotons and A and C are constants that depend on the magnitude measurement used. C may also include additional corrections to account for differences in source medium that are independent of the yield. Empirical relationships to estimate yield have been developed using body wave magnitudes (mb) and surface wave magnitudes [M_s] (e.g. Mueller and Murphy 1971; Murphy, 1977; Burger et al., 1987; Murphy, 1996) from past nuclear explosions with known yields. Given and Mellman, (1986) and Ekström and Richards, (1994) performed moment tensor inversions on the Shagan River explosions from the former Soviet Union and explosions from the U.S. Nevada Test Site (NTS), and computed the moment-yield relationships. Yield estimation using the M_{ISO} from moment tensor inversions can be challenging due to difficulties assessing the contributions from the isotropic and the non-isotropic radiation of the source as discussed in Stevens and Murphy (2001), as well as due to free surface effects at shallow depths. However as demonstrated in *Ford et al. (2012)* and *Chiang et al. (2014)* and the previous sections, source-type analysis (NSS), and the combination of waveform and first motion data can help to better constrain the isotropic radiation of the moment tensor.

We calculated the yields for HUMMING ALBATROSS using the waveform moment tensor results at the reported centroid depths, and the M_{ISO}-yield relationship $M_{ISO} = \log_{10} Y + 14.05$ from Stevens and Murphy (2001). The empirical relationship is derived from previously published moment tensor inversion results, and announced yields or estimated yields from Shagan and NTS explosions (Fig. 8). For comparison, we also calculated the linear regression by solving both the slope and intercept (A and C in eq. 3.2.7), using the same explosion dataset. To use Stevens and Murphy (2001)'s empirical relationship we extrapolate the curve down to very low values of yield and isotropic moment. Because the empirical relationship is derived from nuclear explosions, differences in the seismic coupling efficacy between nuclear and chemical explosions (Murphy, 1996) can also bias our yield estimates. We present our yield estimates and the true yields in Table 2. The moment tensor inversion at shallow depth overestimates the yields for all three explosions; the estimated values are 2.8 times, 7.6 times and 4.4 times greater than the true yield for the production shot, 800, and 400, respectively. However, from our combined NSS analysis, we can estimate the errors associated with our moment tensor solutions. We choose a population of moment tensor solutions with normalized VRs ≥ 90% and computed the mean and 2-sigma from the mean. For the Production shot, the mean is very close to the Stevens and Murphy (2001) scaling, and for the two smaller shots the lower error bounds overlaps with the empirical scaling.

From our synthetic studies on the effects of free surface at regional distances, we observe the recovered mechanism is less sensitive to the source depth, but there can be bias in the moment due to the loss of traction at the surface. Although the deviations from the true moment are all within 20% from our synthetic tests, the amount of deviation also depends on station coverage, frequency passband and station quality. Additional synthetic tests on varying the

station coverage, frequency band and noise level suggest that although the amount of bias in M_{ISO} varies, the asymptotic behavior as a function of depth remains similar, and that the recovered M_{ISO} approaches the true value as the source depth increases. Thus in order to minimize the vanishing traction effects, it may be possible to invert for the source parameters at a deeper depth where the synthetic tests show the M_{ISO} approaches the true value. Here we investigate the possibility to recover the correct yield by intentionally inverting for the source at a deeper depth.

We first perform similar synthetic tests for a pure explosion scenario using the production shot station configuration, filter passband and 1D velocity model to predict the depth range in which we can minimize both the effects from vanishing traction and incorrect source depth. We fix the depth of the data but vary the depth of the Green's functions (as what is done in practice when source depth is unknown or has large uncertainties), and found that the moment tensor inversion is able to recover the correct focal mechanism and seismic moment at depths between 0.02 and 0.05 km. This is an idealized case with no time shift in the inversion, high SNR and prefect knowledge of the Earth structure, the question remains whether this adjustment in the source depth can correctly estimate the yield from real explosions where we have imperfect knowledge of the Earth structure.

In Figure 18b the yield estimates for HUMMING ALBATORSS as a function of source depth are compared. In general because M_{ISO} decreases as source depth increases, the estimated yield also decreases. Yields computed from M_{ISO} obtained at 0.02 and 0.05 km depth do agree with the true yield, but as noted previously we start to see tradeoff between incorrect source depth and source mechanism around 50 to 100 km where the moment tensors are no longer predominately explosive using only waveform data. Unlike the synthetic case, with real data, introducing additional errors from incorrect source depth can have a greater impact on the recoverability of the mechanism, particularly for the smaller shots 800 and 400 where we use higher frequency waveforms.
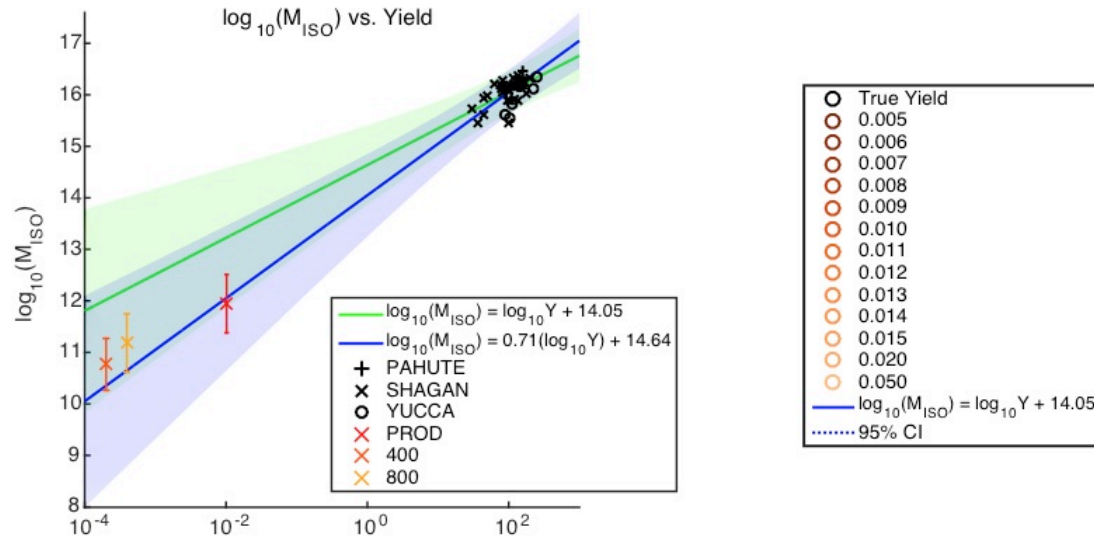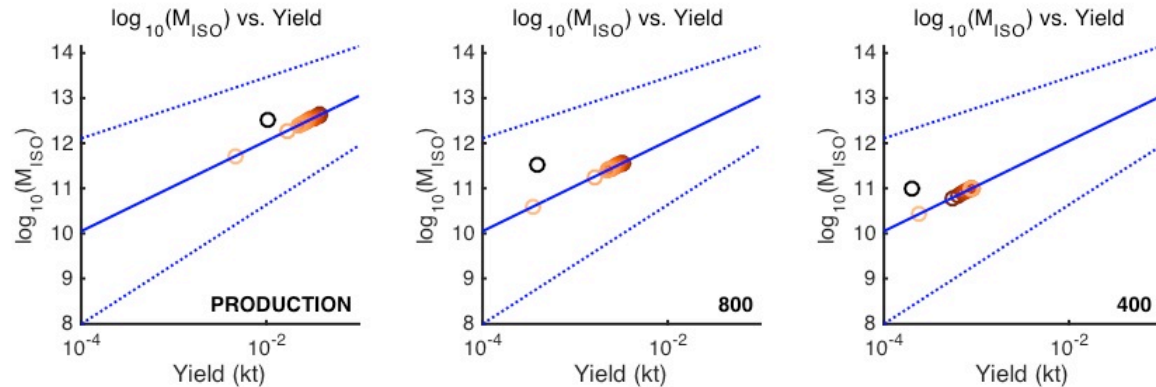
Figure 18. a) Isotropic moment vs. yield from nuclear explosions listed in Stevens and Murphy (2001) and HUMMING ALBATROSS chemical explosions. Two moment-yield scaling relations are shown, one with a slope of one (Stevens and Murphy, 2001) and one where we solve for both the slope and intercept. The shaded regions are the 95% confidence bounds. The mean isotropic moment and error bars (2-sigma) for the three HUMMING ALBATROSS events are computed from a population of moment tensors with normalized VRs $\geq$ 90% in the combined NSS, as shown in Figure 15b. b) Isotropic moment vs. yield for HUMMING ALBATROSS at various depths. The yields are computed using the empirical scaling relation by Stevens and Murphy (2001), and the isotropic moment (at the reported centroid depth) from waveform moment tensor inversion vs. the true yield is also plotted.

3.2.6 Discussion

Synthetic moment tensor inversion tests show that although the loss of traction at the free surface affects the moment tensor inversion's ability to resolve the seismic moment at shallow depths, the impact on the recoverability of the source-type (explosion, double-couple, composite mechanism) is substantially less. This is illustrated by the successful discrimination of the NTS, DPRK, Soviet JVE, Chinese Lop Nor and HUMMING ALBATROSS events as explosions. However, the degree in which free-surface vanishing traction affects the seismic moment

depends not only on the station geometry, noise levels and filter passband but also on the velocity model. Free surface effects are more pronounced when modeling longer wavelengths.

Non-isotropic radiation in the HUMMING ALBATROSS moment tensor solution is a combination of both the free-surface effects and strong SH waves. Love wave generation from chemical explosions is not an uncommon observation, and a number of studies on quarry blasts suggest that the non-isotropic radiation results from spall of material from the quarry face (Goforth and Bonner, 1995; Bonner et al., 1996), and the interaction of the wavefield with the severe topographic features of quarry benches (Barker et al., 1993). McLaughlin et al., (2004) modeled observed short period Love and Rayleigh waves from a Texas quarry and found that the horizontal throw of material from the free face (spall model) is the dominant mechanism. Our moment tensor analysis does not take into account the horizontal single-force component due to spall, the collapse of the quarry cliff face, and for the production shot, the temporal and spatial spread from the delay-firing scheme. These complications contribute to difficulty in unique source-type identification using long-period waveforms only (Figure 15a). The non-isotropic component of the inversion results is manifested as a reverse mechanism with either a near-vertical or near-horizontal dipping layer, and a vertical dip-slip mechanism in the deviatoric solution. Because the high frequency P waves may be more sensitive to radiated energy from the initial rupture (Pearce and Rogers, 1989; Guilhem et al., 2014), including P-wave first motion polarities are particularly useful to constrain the isotropic component of explosive events where the first arrivals come from the detonated explosion. As illustrated in Figure 15, the added constraints from first motion observations greatly reduce the ambiguity in source mechanism from waveforms and result in a unique identification of the events as having substantial volumetric components consistent with explosions.

Moment tensor based event discrimination for shallow sources is reliable when SNR is high, especially with the combination of data from waveforms and first motions. When we include errors in the isotropic moment estimated from the NSS analysis, we see although there is still a bias towards lager moment (800 and 400) even at such low yields and low magnitudes, the isotropic moments intersect with the empirical scaling relation. Although source inversions at greater depth reduce the effects of vanishing traction, in cases of extreme free-surface effects and complexities in the source such as the chemical explosions from this study, added errors from incorrect source depth can impact event discrimination (in the case of waveform only inversion). In addition to the uncertainties associated with the moment estimates, another factor that needs to be taken into consideration when estimating yield using magnitude-yield scaling laws is the nature of the explosive materials. For the same yield, nuclear explosions, single-fired buried chemical explosions, and ripple-fired quarry blasts exhibit differences in radiated seismic energy (Murphy, 1996), therefore additional scaling is required to factor in the differences in seismic coupling for different types of explosions. All three shots are partially confined but the production shot uses a ripple-firing scheme and the two smaller shots are single-fired chemical explosions. Traditionally single-fired shots are designed to maximize the strength of the seismic signal (Khalturin et al., 1998).

3.2.7 Conclusions

Theoretical vertical dip-slip Green's functions associated with the M_{xz} and M_{yz} components have vanishing amplitudes at shallow depths (< 1 km) due to the loss of traction at the free surface, while the Green's function waveforms look similar with little phase distortion. However synthetic calculations at shallow depths show moment tensor based event

discrimination is reliable and the resolvability of the moment tensor solution depends on station configuration, noise level, the frequency band and the velocity model.

We are able to recover a predominantly explosive source mechanism for the three HUMMING ALBATROSS chemical explosions from moment tensor inversions. Although the source-type uncertainty analysis shows that we cannot uniquely characterize the events as predominantly explosive using only waveform data, the combined waveform and first motion method enables the unique discrimination of these events. This method has been applied in previous studies which have shown the inclusion of P-wave first motions in addition to full waveform data eliminates the common ISO-CLVD tradeoff (Ford et al., 2012; Chiang et al., 2014) and reduces the uncertainties of sparsely recorded underground explosions with strong Love waves and reversed Rayleigh waves (Chiang et al., 2014). In this study we further demonstrate that incorporating the two data sets is particularly useful in constraining the isotropic component of explosions, and the method not only applies to large events, but also small magnitude, very shallow explosions that are effectively at the free surface. The combination of both low frequency full waveform data and high frequency P-wave polarities greatly enhances the capabilities of the moment tensor source-type discrimination method in cases of sparse station coverage, strong Love waves and free-surface effects.

The moment tensor method is capable of event discrimination, although yield estimation using the recovered absolute seismic moment from moment tensor inversion remains challenging and can have large uncertainties, we can begin to put error bounds on our moment estimates, and therefore yield, using the NSS technique and combining waveform and first motion. Pure explosion synthetic tests suggest source inversions at deeper depths reduce the free surface effects on the moment, but we cannot draw definite conclusions using the results from the HUMMING ALBATROSS data set due to not only free-surface effects, but uncertainties associated with imperfect knowledge of the Earth structure, unaccounted non-isotropic radiation due to the mass movement of the quarry face and differences in seismic coupling between different types of explosions. In addition, the moment-yield relationship derived from larger nuclear explosions may not be adequate for such low magnitude chemical explosions.

3.3. Synthetic Analysis of 3D Velocity Structure Effects on Moment Tensor Inversion

3.3.1 Introduction

We have established in the previous two chapters that the regional seismic moment tensor (MT) method is a robust and reliable technique to identify different seismic source types under sparse monitoring situations, at shallow source depths, and when the complexities in isotropic source processes are often not well understood (e.g. Massé, 1981). For this study we will explore possible biases associated with one of the most fundamental assumptions in seismic source analysis, which is the assumption that a 1D velocity model is a good approximation to real Earth structure.

The ground motion (u) recorded at the receiver is a linear combination of the source (seismic moment tensor, **M**) and the Green's tensor (**G**), where u = **GM**. The Green's tensor represents the impulse response of the medium, describing the seismic wave propagation between the source and receiver for a reference Earth model. Basic source types are typically comprised of fundamental fault representations (e.g. Jost and Herrmann, 1989), but they can also be fundamental single-couples and vector dipoles. In previous studies (e.g. Ford et al., 2009b; Walter et al., 2009; Nayak and Dreger, 2014; Chiang et al., 2014) simple but wellcalibrated 1D velocity models have been used to compute the Green's function and invert for the MT. This assumption is valid at relatively long periods where the wavelengths being inverted are much larger than the spatial dimension of the sources, and the source time history is short compared to the frequency passband of the inversion. However the limits of the definitions are not very well defined, nor are they thoroughly explored in the published literature.

The approach to compute Green's functions, especially in regions of low-seismicity where high-resolution velocity models are not available, is through waveform modeling of regional earthquakes to produce calibrated 1D velocity models (e.g. Dreger and Helmberger, 1990; Bhattacharyya et al., 1999; Baise et al., 2003; Kim et al., 2011). However, the 1D velocity model assumption can be the greatest source of error in the MT solution and has never been thoroughly investigated for the source-type discrimination application. In Ford (2009b), the sensitivity of full MT solutions for the 2009 Memorial Day DPRK nuclear explosion to 1D velocity structure was examined. In that study 880 1D velocity models for the region from the North Korean test site to regional distance broadband stations, derived from the Monte Carlo Markov Chain inversion results (Pasyanos et al., 2006), were tested to investigate the effect on the recovery of the seismic MT source type (e.g. Hudson et al., 1989; Ford et al., 2010). The results indicated that while there was a strong effect on the source-type and the ability of the Green's functions for the individual velocity models to fit the data, overall the velocity model uncertainty was not large enough to affect the discrimination of the seismic event as an explosion. The spread of the derived solutions in source-type space (e.g. Hudson et al., 1989) in that study does illustrate however that the effect needs to be examined further, particularly for cases where precise source-type determination is important, and for very sparse monitoring conditions where the range of acceptable solutions in terms of the

ability to fit the data can become large due to poor station coverage. From our study of explosions in Eastern Kazakhstan and Lop Nor (Chapter 2; Chiang et al., 2014) we also observe similar variations in waveform fits, moment and MT derived source-types as a function of velocity model. Thus, a comprehensive understanding of the uncertainties associated with the assumed 1D velocity structure is crucial in being able to apply the MT based discrimination method to new regions of interest in order to fully assess populations of MT results for explosions, collapses, earthquakes, geothermal and volcanic events.

There are some studies that have examined errors in regional MT inversions due to biases from velocity models. Wei et al. (2012) shift the theoretical seismograms used in their 1D Green's functions according to a 2D correction surface. Comparison with and without the time shift shows the solution improved when the authors incorporated the correction. This is similar to what Ford (2008) found in which when time shifts were employed the spread of MT solutions for different 1D velocity model Green's functions in source type space was reduced. In the Berkeley MT code (Dreger, 2003; Minson and Dreger, 2008) a time shift is applied for optimal alignment of the data with the applied Green's function which takes into account, to a degree, the discrepancy between the velocity model and the actual Earth structure (Pasyanos et al., 1996). Šílený (2004) has investigated the sensitivity of full regional MT inversion for an $M_W4.8$ earthquake in Italy to perturbed 1D velocity models and found that the DC mechanism is well-resolved from 10 to 50 second but not from 5 to 10 seconds. Liu et al. (2004) obtain MTs for three earthquakes in Southern California with a regional 3D model using the spectral element method and compare the 3D solutions with those obtained from body wave and surface wave inversions, and found that the solutions agree well. Covellone and Savage (2012) calculated 3D Green's functions for earthquakes in the Middle East and show improved waveform fits and a reduction of non-double-couple (non-DC) components. Panning et al. (2001) included near source 3D velocity heterogeneity and found its effect to be minimal in the bandwidth of interest, although small isotropic components ($\sim$10% of the total scalar moment) could arise due to the unmodeled near-source 3D structure. Although there have been studies on the effects of 3D structure on source inversions (e.g. Panning et al., 2001), to our knowledge, there has not been much work investigating the effect of 3D heterogeneity along the full source-receiver path on the full regional MT for earthquakes aside from the Covellone and Savage (2012) work. For non-DC sources, Tkalčić et al. (2009) determined the source parameters of a volcanic earthquake using data from 20 to 50 seconds and path-specific 1D velocity models to account for 3D heterogeneity. This work offers the first systematic investigation of potential bias due to unaccounted 3D structure on regional MT inversion.

As a result of the unprecedented coverage of the NSF EarthScope transportable array (TA), a number of high-resolution regional 3D Earth models have been published in the literature (Bensen et al., 2009; Moschetti et al., 2010; Porritt et al., 2014; Shen et al., 2013). The availability of these finer resolution regional tomography models, particularly the ambient noise surface wave models allow us to generate synthetic waveforms in the

frequency range relevant for regional waveform modeling of small to moderately-large events. Previous work by Ford et al. (2009a) studied a variety of events in the western U.S. with the majority of events near or at the Nevada Test Site (NTS). These events included nuclear and chemical explosions, earthquakes and mine and nuclear cavity collapses. For these events we study the impact of the 1D velocity model assumption on moment tensor results be means of a series of synthetic studies.   In the synthetic studies we compute 3D velocity model GFs using the anelastic finite-difference (FD) code, Seismic Waves, 4th order (SW4), developed at the Center of Applied Scientific Computing at Lawrence Livermore National Laboratory (Sjogreen and Petersson, 2012; Petersson and Sjogreen, 2014). We use the Moschetti et al. (2010) tomographic model for the western U.S. and station geometries from Ford et al. (2009a). We then invert these 3D synthetic data using GFs for a 1D model to determine the seismic MT and compare the results to the known input moment MT. The effects of the 1D velocity model assumption can then be interpreted via the difference between input and inverted solutions.

3.3.2 Velocity Model and Computation Setup

The synthetic experiment is set up to evaluate the effects of 3D heterogeneity along the source-receiver path. We simulate three-component velocity records using the Moschetti et al. (2010) 3D Earth model and the FD code SW4, and perform the standard MT analysis using Green's functions computed from a well-calibrated 1D Earth model for the Western U.S. (Song et al., 1996). The Moschetti et al. (2010) model spans the entire western U.S. and is constructed based on surface wave dispersion measurements from teleseismic earthquakes and regional-scale ambient noise measurements; the combination of data and dense station coverage better constrains the shear wave velocity structure in the crust and uppermost mantle than previous, earthquake only tomographic models. Moschetti et al. (2010) invert for both isotropic and anisotropic models but in this study we only consider the isotropic model. The 3D velocity model consists of a low velocity sediment layer and three crystalline crustal layers above the Moho, and a smoothly varying upper mantle below the Moho. The compressional wave velocity to shear wave velocity (Vp/Vs) ratio and density structure of the inverted 3D model are based on empirical relations between wave speed and density (Brocher, 2005). Focusing on California and Nevada (Figure 19 the California Coast Ranges have slow wave speeds in the upper and middle crust, and beneath the Central Valley of California the low wave speeds are associated with thick sediments in the San Joaquin Basin to the south and the Sacramento Basin in the north. In the Central Valley and southernmost end of Sierra Nevada the Moho varies between 20 to 40 km, and the crust thickens near the eastern edge the Sierra Nevada. Moschetti et al. (2010) attribute the low velocity anomalies of the lower crust beneath eastern California, the Basin and Range and the High Lava Plains to conductive heating. The Basin and Range in northern Nevada has relatively uniform crustal and mantle structure, as the relatively long-period surface waves used to construct the model are not sensitive to large impedance contrasts from very thin   layers.

For our FD simulation we did not include any water layers. We account for attenuation, Q, using a function of local Vs [km/s] (e.g. Graves et al., 2008; Olsen et al.,

2009), such that Qs = 50Vs and Qp = Qs. The FD code SW4 solves the seismic wave equation in a displacement formulation using a summation-by-parts principle and it is fourth-order accurate in space and time (Sjogreen and Petersson, 2012; Petersson and Sjogreen, 2014).
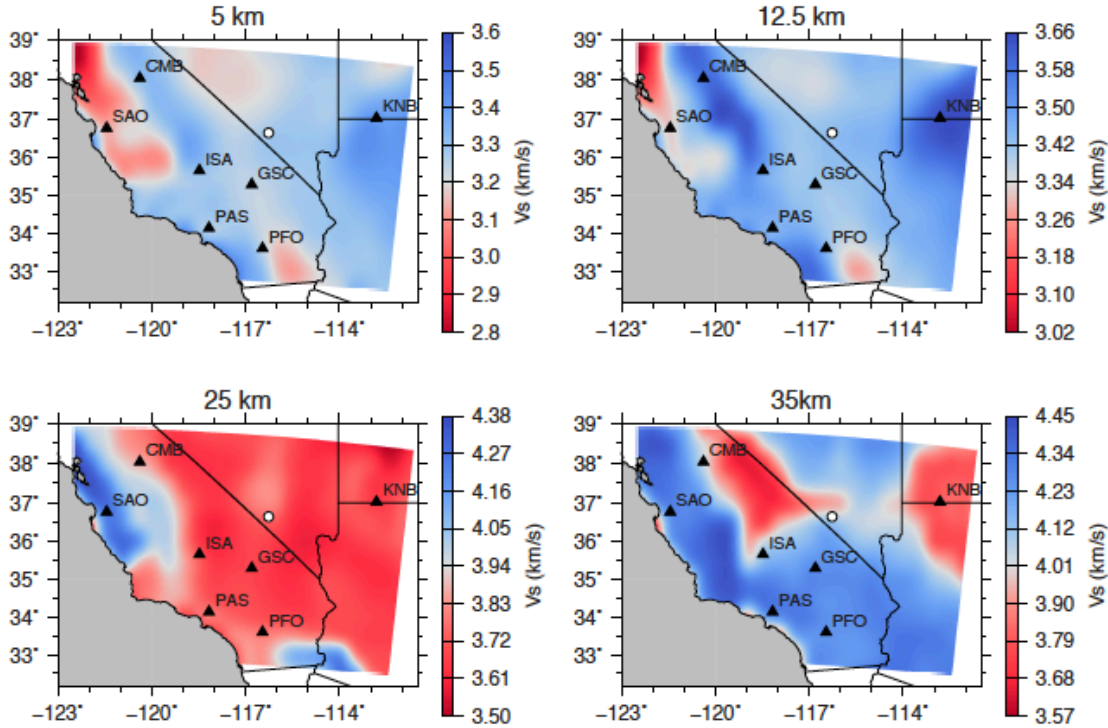
Figure 19: Background color represents the shear wave velocity (Vs) from Moschetti et al., (2010) at various crustal depths, white circle is the event location, and black triangles are the station locations.

The code utilizes a Cartesian mesh to solve the seismic wave equations and the mesh can be built using the PROJ.4 cartographic projections library (Developed by G. Evenden, https://trac.osgeo.org/proj/) to ensure accurate mapping between geographic and Cartesian coordinates. In contrast to a staggered grid finite difference scheme (e.g. Larsen and Shultz, 1995), SW4 uses a node-centered formulation to reduce computation memory. The computation domain consists of a free-surface boundary at the top with the option for irregular topography (Appelo and Petersson, 2009), and absorbing super-grid boundaries in the far field to minimize boundary reflections from the side and the bottom of the computation domain. We performed the calculations on the Livermore Computing Center (LC) 8-core Xeon 35-2670 Linux cluster, cab, consisting of 1,296 nodes, each with 16 cores per node and 32 GB memory. The velocity model is discretized on a Cartesian grid with 500 m grid spacing and a minimum Vs of 1.1 km/sec. SW4 internally resamples the coarser 3D tomographic model (0.5 degree grid spacing) on to the finer computation grid via 2-steps: (1) linear interpolation in the vertical direction and (2) Gaussian averaging in the horizontal directions. The model domain extends approximately 665 km x 950 km x 70 km,

and we apply a Dirac delta forcing function at the source to simulate a seismic source in our FD calculations. To avoid numerical artifacts due to grid dispersion we consider 10 grid points per minimum wavelength, and therefore the maximum resolvable frequency is 0.2 Hz for the given minimum Vs. Since we are inverting data between 0.01 to 0.1 Hz and given the magnitude range (M < 5) of the events we are investigating it is not necessary to consider a source time history beyond the basic Dirac delta function.

Prior to performing the synthetic sensitivity tests, we performed benchmark testing to validate the wave propagation simulated using SW4. We generated and compared 1D velocity waveforms using the two different methods: (1) the frequency-wavenumber (FK) integration method (Wang and Herrmann, 1980; Herrmann and Wang, 1985; Zhu and Rivera, 2002) and (2) the numerical FD method (SW4). The FK code is included as part of a software package called Computer Programs in Seismology (CPS3.30) developed by Herrmann (2013) at St. Louis University. We use a simple three-layer model with no attenuation and computed the synthetics at 100 km distance for the fundamental Green's tensor force couples (Figure 20 Both methods agree closely, where deviations are mostly due to small amplitude differences in the G_{XZ}, G_{YZ} and G_{ZZ} components.
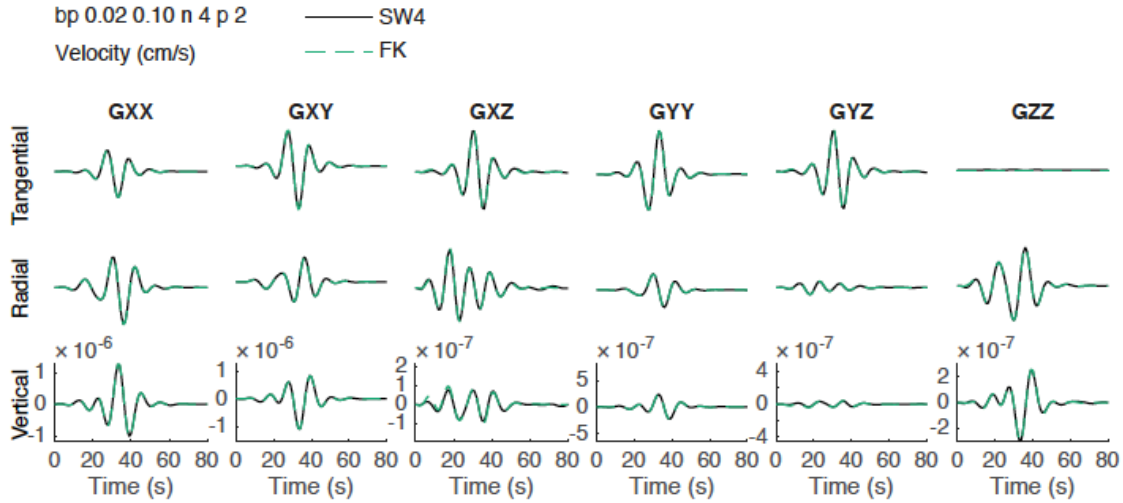
Figure 20: Waveform comparison between finite-difference (SW4, solid black line) and frequency wavenumber integration (FK, dashed line).

3.3.3 Sensitivity to 3D Velocity Structure

We set up the synthetic experiment to simulate the standard processing procedure used in regional MT analysis. The simulated 3D, three-component velocity records (north-south, east-west and up-down) from SW4 are treated as "data" in our synthetic test. For each station, we rotate the data to transverse, radial and vertical, and add random Gaussian white noise to the data by scaling the amplitude of the noise to 10% of the maximum amplitude of the three components. 1D Green's functions were calculated using the FK method Herrmann (2013). The 3D synthetic data and 1D Green's functions are both filtered between

10 to 50 seconds. Differences between the input and recovered MT reveals the bias due to 3D structure. A direct comparison of the 3D and 1D synthetics for a normal earthquake mechanism shows minor differences in the arrival times and waveforms, and almost no difference in the 20 to 50 second period range which is a commonly used passband in regional waveform source inversion Pasyanos et al. (1996). This is due to the large wavelengths in the 20 to 50 second passband and the smooth nature of the 3D tomographic model. Nevertheless, as regions of monitoring interest are calibrated the 3D models produced are likely to be with the same type of regional-scale surface wave approach used to construct the 3D tomographic model examined in this study. The following section describes the results for the three types of sources we have tested: (1) double-couple (earthquake), (2) isotropic (explosion) and (3) composite source mechanisms. We used the Little Skull Mountain mainshock station geometry of Ford et al. (2009a) for all of the synthetic sources in this experiment to reflect a real regional monitoring configuration.

3.3.4 Double-Couple Sources

First we examine the 1D model assumption for the double-couple (DC) sources. We tested two DC mechanisms: a normal earthquake and an oblique reverse event, both at 4.5 km depth. The normal faulting mechanism is taken from the Little Skull Mountain mainshock MT solution in Ford et al. (2009a). For the DC synthetics, both deviatoric and full MT inversions can recover the correct source mechanism (Figure 21 and the variance reduction (VR), a measure of the goodness-of-fit between data and synthetics, are very similar for both inversion schemes. Although the full MT results have up to 16% ISO component in the full MT inversion (Figure 21 the change in VR is not statistically significant as determined by an F-test (Menke, 1989; Templeton and Dreger, 2006; Menke, 2012), where the level of significance is only 57%. Similarly, the Network Sensitivity Solution [NSS] (Ford et al., 2010), a mapping of the goodness of fit parameter in the complete source-type space, shows an earthquake-like surface centered on the origin (pure DC). The CLVD components are 17% and 40% for the normal and oblique mechanisms, respectively (Figure 21 Interestingly the oblique earthquake was found to have larger variability in the non-DC components compare to the normal earthquake (Figure 22 The best solutions for the oblique mechanism are more widely distributed in the NSS. The differences in the NSS distribution and non-DC components between the two types of DC mechanisms are likely the result of different radiation patterns, and the non-uniform sampling of the radiation from the sparse station coverage. All stations except one are located to the west of the source (Figure 19).

Total moment from the full MT solution is quite close to the true value, estimates of seismic moment are all within 10% of the true value. The source depth can be determined from the goodness of fit curve (Figure 22 however there is some mechanism sensitivity. The source-type plots (Figure 22 illustrate the tradeoff between source depth and mechanism, shwoing that as source depth deviates from the true depth the ISO component also increases. But for both cases the MT solutions are stable with respect to source depth and the solutions with the best waveform fits (VR > 60%) are between 5 and 7 km. The best fitting solutions yield the correct mechanism and depths close to the correct source depth of 4.5

km. In summary for the two DC cases, we can recover the correct fault plane solution using only regional waveforms and it appears that the 1D model assumption is adequate, but one must be careful when trying to interpret the CLVD component. Apparently the effect of 3D heterogeneity is negligible at these periods for recovering the correct DC mechanism using a 1D model, but 3D heterogeneity can increase contributions from the CLVD. However, the NSSs show a pure DC mechanism fits the data equally well and can be used to quantify the level of variability in the non-DC components (Fig. 11a).
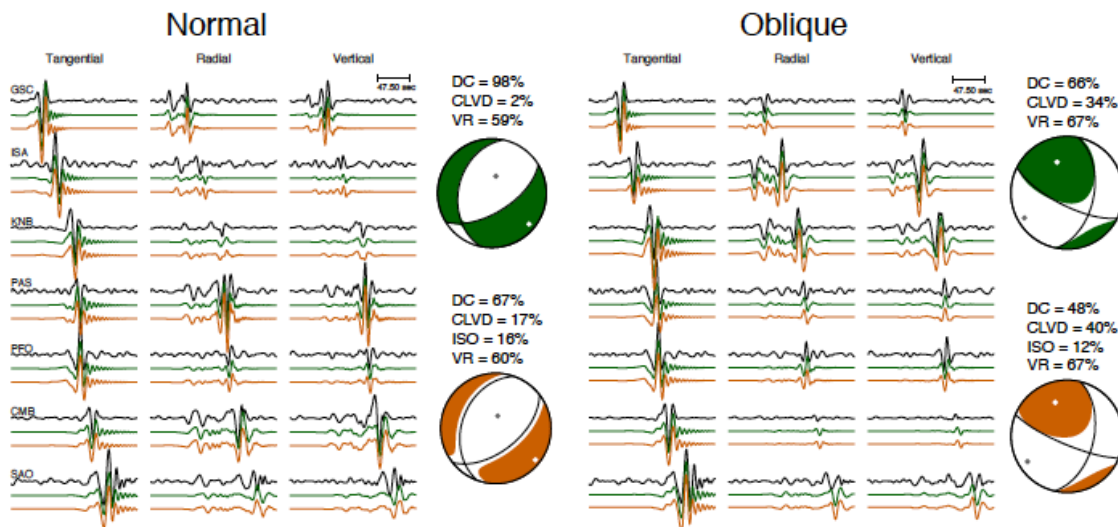
Figure 21: The simulated 3D data is in black, the deviatoric solution is in green and the full solution is in brown. All waveforms are in displacement (cm).
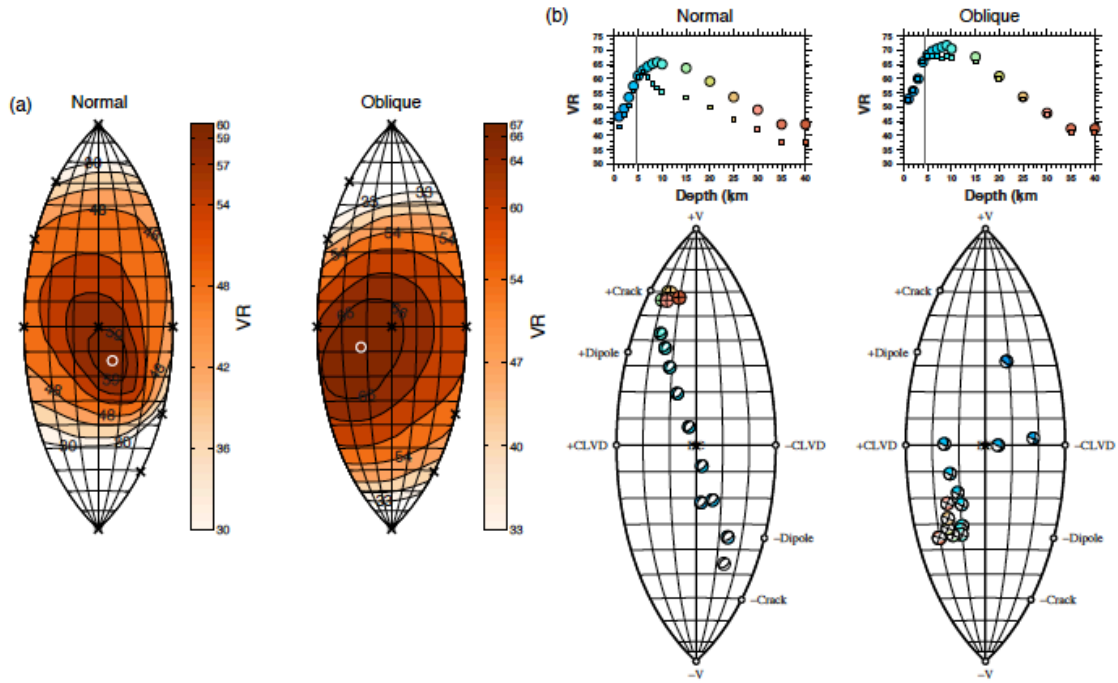
Figure 22: (a) Network Sensitivity Solutions color-coded by variance reduction (VR) presented on the Tape and Tape (2012a) and Tape and Tape (2012b) Lune. The white circle represents the location of the best full moment tensor solution in source-type space. (b) VR with respect to source depth for two different DC mechanisms and color-coded by source depth. The filled circles are full moment tensor solutions and the filled squares are deviatoric moment tensor solutions. The full moment tensor solutions are also plotted in source-type space and color-coded by source depth as well.

3.3.5 Isotropic Sources

A direct comparison between 1D and 3D synthetic data for the explosion case shows more variation in waveforms compared to the earthquake cases (Figure 23 which is likely due to the shallow explosion source depth that was considered (500 m). In addition, the averaged 1D model is less representative of the shallow structure in the 3D tomographic model. Since the isotropic source radiation pattern has no azimuthal dependence, variations in waveforms due to the 3D structure are more prominent; whereas an earthquake source imposes an order of magnitude variation in the radiation pattern as a function of azimuth. At long periods the source variation is large compare to the effects of 3D structure in this long-period passband. The recoverability of the explosion source depth is similar to what was found in the previous 1D synthetic studies (Fig. 11) and real explosions (Chiang et al., 2016) in that the source depth recoverability primarily depends on the frequency band used in the MT inversion. Because the source depth is much less than the wavelengths considered, we cannot resolve the source depth in detail and can only constrain it to be shallower than 1 km. The MT analysis shows the deviatoric MT solutions are stable at shallow depths (Figure 24c) but the isotropic component is not well constrained in the full

MT inversion since the isotropic component is very sensitive to the time shifts in the inversion. The full MT solutions alternate between an explosion and a CLVD mechanism with the major vector dipole in compression depending on the time shifts due to the fact that the long-period surface wave radiation of the isotropic source and a CLVD with a major vector dipole in compression are the same. The tradeoff between these two source types is seen in the NSS for this test (Figure 24c) where a pure explosion mechanism obtained from a grid-search method has a VR of 75% and the full MT has a VR of 76%.

The alternation between the two mechanisms is the manifestation of the classic tradeoff for an explosion source (e.g. Ford et al., 2009b). For an isotropic source, the level of false non-ISO components in the moment tensor results from unmodeled 3D structures and the theoretical ISO-CLVD tradeoff, and thus it is difficult to tease out how much of the CLVD component is due to unmodeled 3D structure. Combining waveform and first motion polarities can eliminate the tradeoff to get the best MT, and we obtain a solution located close to the theoretical explosion (Figure 24c). The best solution consists of a predominantly explosive mechanism with 60% ISO, 28% CLVD and 12% DC. The MT still has a relatively high CLVD component but the level of false-DC is low. This is an important result for discrimination because it shows that unmodeled 3D structure at the typical passband used in regional distance nuclear monitoring does not introduce false-DC in the inversion results.
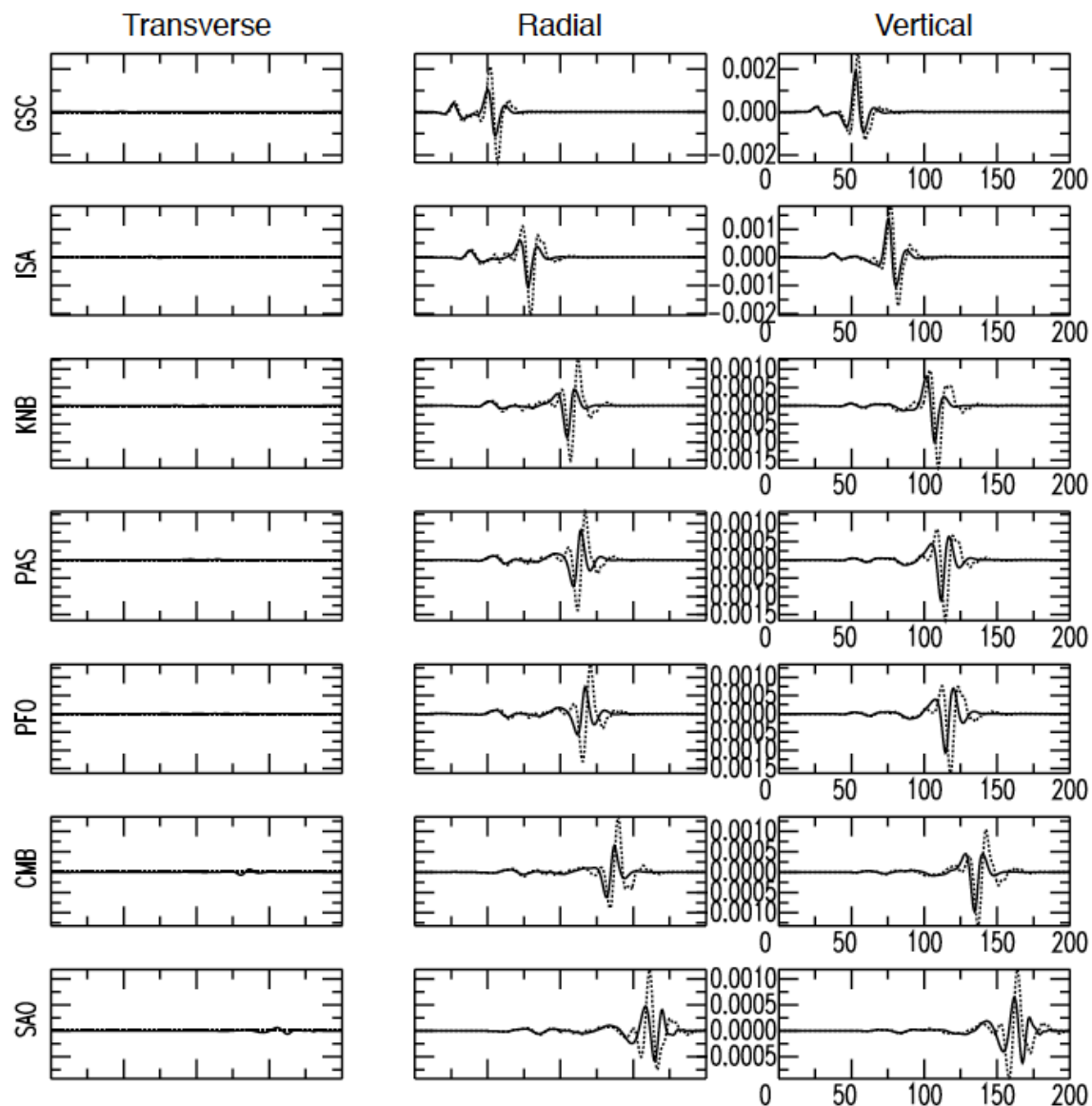
Figure 23: Dashed lines are waveforms calculated using a 1D Earth model and solid lines are waveforms calculated using a 3D Earth model. The waveforms are in displacement (cm) and band-pass filtered between 10-50 seconds.
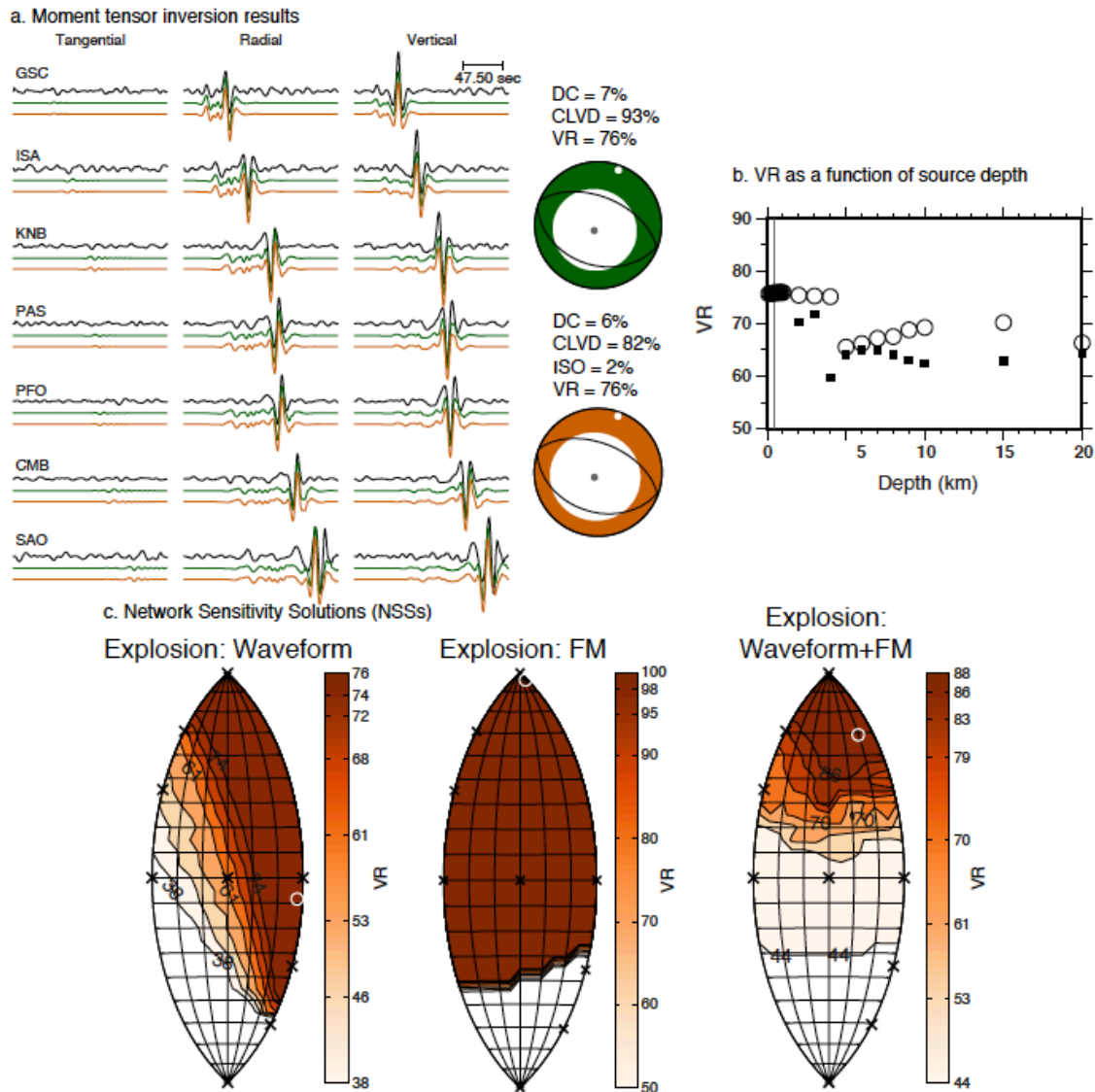
Figure 24: (a) Explosion moment tensor solutions and waveform fits from 10 to 50 seconds. The simulated 3D data is in black, the deviatoric solution is in green and the full solution is in brown. All waveforms are in displacement (cm). (b) Variance reduction (VR) as a function of source depth. Circles are full moment tensor solutions and the squares are deviatoric moment tensor solutions. (c) Network Sensitivity Solutions using only waveforms, only first motions or combining waveforms and first motions. The white circle represents the location of the best full moment tensor solution in source-type space.

3.3.6 Composite Sources

Explosion processes are often not purely isotropic, and they typically exhibit evidence of complex seismic radiation, particularly from the presence of long-period Love wave energy. Large non-ISO components have been observed in real explosion data, sometimes referred to as tectonic release (e.g. Massé, 1981; Ekstrom and Richards, 1994), and this component can become large enough to reverse the Rayleigh wave polarities (e.g. Walter and Rodgers, 1999; Chiang et al., 2014) which can complicate discrimination, as well as generate long-period (20 to 50 s) Love waves that can have the largest amplitudes of all three-components at a given station (e.g. Dreger and Woods, 2002; Ford et al., 2009a). In addition, shear failure is often seen in real explosions (Toksöz, et al., 1965; Toksöz and Kehrer, 1972; Burger et al., 1986; Day et al., 1987). Therefore it is necessary to examine whether the MT inversion method breaks down and can become biased when both the effects of complex source processes and unaccounted for 3D effects are included, and whether the ability to successfully identify a given seismic event as an explosion can be compromised.

The composite source considered here consists of a pure explosion and reverse mechanism (strike= 135; dip= 40; rake= 105) both at 500 m depth. We apply the same data processing procedure and station configuration used for the DC and ISO cases, and added random Gaussian white noise. For a composite source that is predominantly explosive, the combination of 3D effects and source tradeoff appears to have an impact on the inverted solution. The level of CLVD can be as high as 60% (for the case with 40% DC). The MT solutions and waveforms fits for a composite mechanism with 30% DC is shown in Figure 25a. The full MT solution is 45% CLVD suggesting that the solution is still dominated by the theoretical trade-off for explosive mechanism. Figure 25b shows that the solutions for composite sources with varying percentages of DC are still dominated mostly by the explosion-CLVD trade-off and the waveform NSS distributions remain more explosive-like even as the contribution from the DC increases. Although the recovered DC components for the MT inversions are close to the input value (30% DC), the inversions do not recover the correct DC mechanism. Instead of a reverse mechanism the full MT inversion for a composite source with 30% DC recovers a normal mechanism (strike= 169; dip= 72; rake= −104).

The inversion recovers a shallow dipping reverse component only when the DC contribution reaches 50% (Figure 25b). The orientation of the DC cannot be resolved for a predominately explosive composite source. The results of this test and the previous tests indicate that there can be substantial variability in the minor components of a recovered moment tensor. These minor components appear to be the most strongly affected from the unaccounted for 3D velocity model. It is good news, however that the primary moment tensor components, namely a DC for tectonic earthquakes, and the isotropic component for explosions are not strongly affected and therefore the discrimination of the two types of mechanism remains robust.
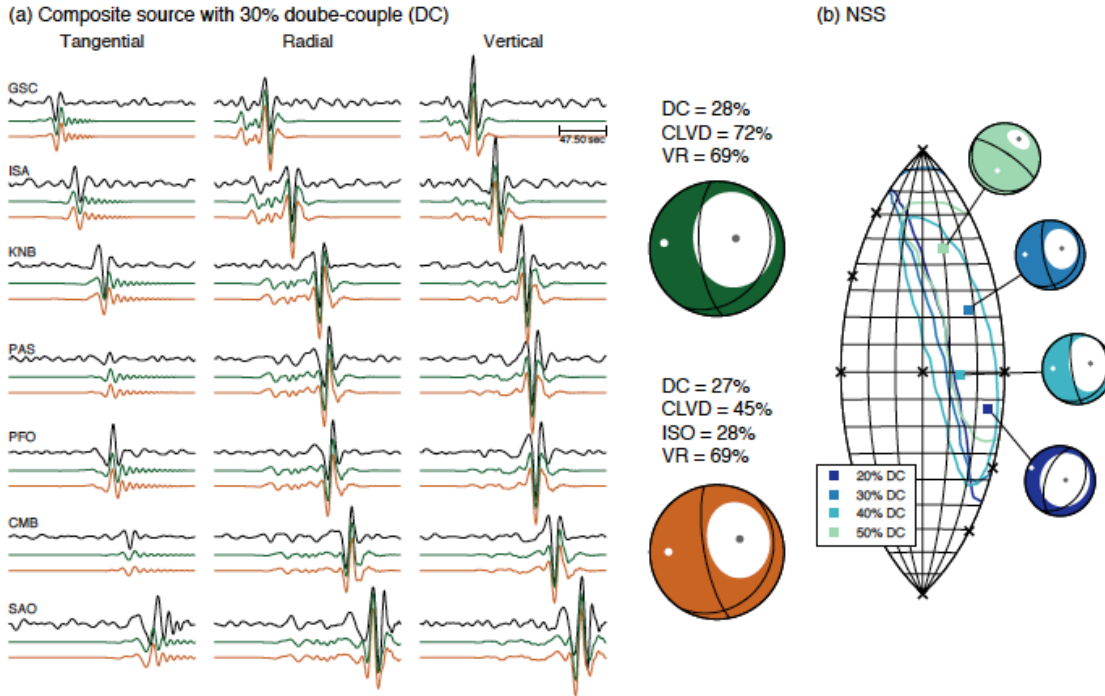
Figure 25: (a) Deviatoric (green) and full (brown) moment tensor solutions and waveform fits. The simulated data for an explosion plus reverse fault mechanism are in black. The example shown here is a composite source with 30% DC. (b) The best-fitting full moment tensor solution and NSS in source-type space for four composite sources. All solutions have the same mechanism (explosion + reverse fault) but different percentage of DC. The contours represent moment tensor solutions with normalized VR$\geq$ 98%.

3.3.7 Path Calibrations

One solution for trying to reduce possible MT solution bias due to unaccounted for 3D wave propagation effects is to develop source-receiver specific 1D velocity models. Given earthquake data in the source region and independent constraint on the focal mechanism, it would be possible to perform broadband waveform modeling either by forward modeling, genetic algorithm, or full grid-search approaches (e.g. Dreger and Helmberger, 1990; Bhattacharyya et al., 1999; Baise et al., 2003; Kim et al., 2011) to improve the source-receiver velocity. On the other hand if there is independent information from tomography and receiver functions the information can be used to compute path specific 1D models to improve seismic MT recovery in regions of large lateral heterogeneity (Tkalčić et al., 2009). Here we use the 3D synthetic data to evaluate the procedure of using source-receiver path specific 1D velocity structure extracted from tomographic models.

We use the averaged elastic properties and attenuation from the 3D tomographic model   for each source-receiver pair, with a total of seven path-specific 1D velocity models (Figure 26a) and compute the Green's functions for each of these models. The average 1D models have slightly shallower sediment layer and mantle velocities compared to the Song et al. (1996) model. But the Moho depths are very similar (within 5 km) for all the models.

Our synthetic study shows path-specific calibration does help in cases where one simple layered model cannot adequately characterize the underlying Earth structure between different source-receiver pairs, it reduces the non-DC components in earthquakes in the time-domain waveform inversion and increases the waveform fits. The MTs are 88% and 69% DC for the normal and oblique mechanisms, respectively. The biggest difference in the NSS using a universal 1D model for all stations and using path-specific 1D models for the pure DC sources is that for the path-specific models the goodness of fit distribution is centered on the pure DC solution and is not shifted along the deviatoric or isotropic axes. Comparing Figure 26b to Figure 22 we see that the region of best fitting solutions (normalized VR$\geq$ 98%) has a smaller distribution for the oblique mechanism whereas for the normal mechanism the area of the contoured region remains similar to the results using a single velocity model. For the explosion case, the tradeoff between explosion and CLVD persists although the best solution becomes more isotropic compared to the result without path calibration. For the composite source with 30% DC, the best MT is explosive and the CLVD has reduced to only 12%. However we still cannot recover the correct DC mechanism, which is surprising. The recovered fault plane solution is a shallow dipping normal mechanism. In this study, we found that the DC sources benefited more from the path-specific approach.
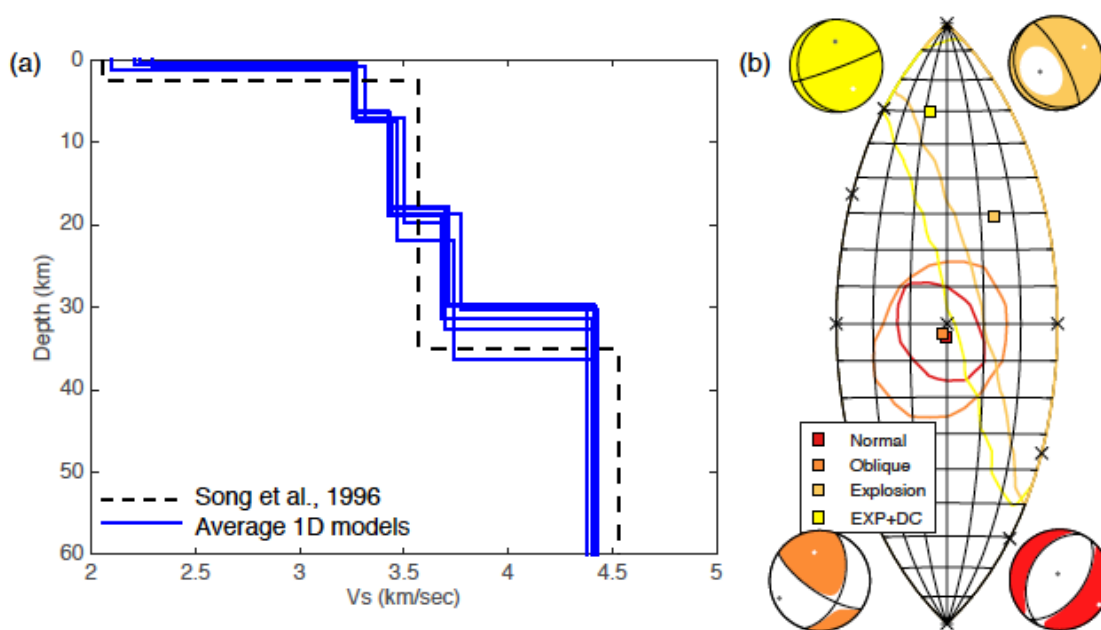
Figure 26: (a) Seven 1D models derived from the 3D model by Moschetti et al., (2010). (b) Full moment tensor solutions and NSS result using path-specific 1D models for each source-receiver pair. The contours are the best-fitting solutions with a normalized VR$\geq$ 98%.

3.3.8 Random Velocity Perturbations

Since the 3D tomographic models are smooth representations of Earth structure we wanted to examine a more severe case in which we apply random velocity perturbations in the model to increase the effects of scattering and multipath in the 3D synthetic data. A realistic description of the inhomogeneous Earth can be described by the von Karman correlation function (Goff and Jordan, 1988):

$$C(r) = \frac{r_v K_v(r)}{2_{v-1} \Gamma(v)} \tag{26}$$

K_v is the modified Bessel function of the second kind order v, where $0 < v < 1$. v is the Hurst number which describes the roughness of the medium, Γ is the Gamma function, x, y, and z are vectors in the 3D random field, and a_x, a_y, a_z are the correlation distances. The von Karman correlation function is self-variant and rich in short wavelength components, making it a common approach to model geologic structures with a fractal nature over a wide scale (Wu, 1982). The Hurst number, which controls the correlation decay, is typically less than 0.5 from modeling of seismic reflection data (e.g. Holliger and Levander, 1992; Nielsen and Thybo, 2006). Correlation distances on the order of a few kilometers to tens of kilometers have minimal effect on the 10 to 50 second waves, therefore very large values are necessary to observe changes in the synthetic waveforms relative to the smooth 3D model in the period range of interest. We use a Hurst number of 0.3 and horizontal and vertical correlation lengths of 250 km and 50 km, respectively, to perturb the crustal velocities. We apply velocity fluctuations up to 20% (Figure 27) and obtain a rough model with crustal velocities following a von Karman distribution. Figure 28a shows the perturbed model at 5 km depth. The velocity contrast between the California coast and the Basin and Range is preserved but with rough edges. Figure 28b shows a cross section of crustal velocities from the coast to the Nevada Test Site, near the location of the synthetic source (-116 degree longitude). The layers are well defined but with small-scale heterogeneities scattered throughout the crust.

We generate 3D synthetics using the perturbed model for a normal earthquake and an explosion, and compare the MTs to the solutions from the smooth model. A comparison between normal earthquake synthetics generated from the 1D model and perturbed 3D model low-pass filtered at 0.15 Hz shows the complexities due to scattering in the 3D synthetics (Figure 29) The scattering (ringing) on the tangential component in the 1D synthetics is due to the low velocity layer in the 1D model (Fig. 26a). When these data were inverted from 10 to 50 seconds a normal mechanism was obtained but the goodness of fit was lower than the typical level (VR > 60%) considered indicating a well-constrained solution. Figure 30a shows the deviatoric MT is 83% DC, which is 10% lower than the solution using the smooth model, whereas the full MT remains similar to the previous result (Figure 21 with 68% DC. But the NSS (Fig. 30b) shows the population of best-fitting

solutions (VR≥46%) deviates further away from a pure DC source and are more broadly

distributed compare to Figure 22 The increase in the area of the best-fitting MTs can be interpreted as increasing bias in the solution due to unmodeled   structure.

In contrast to results for the smooth 3D model, explosion deviatoric and full MTs (Fig. 31a) show false-DC components increased to almost 50%. VR is 57% for both deviatoric and full MTs, a value close to the level of fit for a well-constrained solution, and a pure explosion mechanism obtained using a grid-search method has a VR of 52%. Although   the waveform NSS (Fig. 31b) still shows an explosion-like distribution the best-fitting solutions encompass almost half of the area in the source-type space, including a pure DC source. The first motion constrained NSS eliminated the tradeoff and pure DC source types but compared to Figure 24c the uncertainties estimated from the constrained NSS are slightly larger. The first motion-constrained full MT solutions for the smooth and perturbed 3D model are both 60% ISO, but the solution for the perturbed model has a slightly greater DC of 31%. In   this study we show that the MT uncertainty increases when the 3D model becomes more heterogeneous and the false-DC component increases when an explosion source is considered.
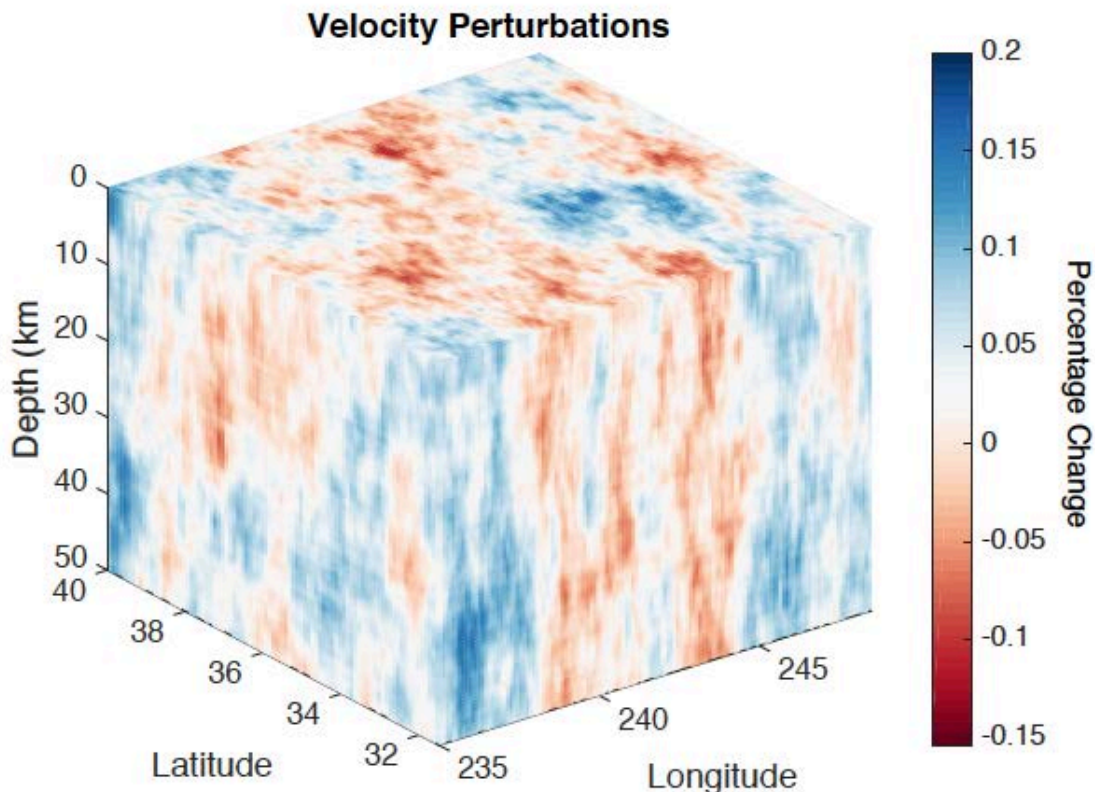
Figure 27: Velocity fluctuations following a von Karman distribution with a Hurst number of 0.3, horizontal and vertical correlation distances of 250 km and 50 km, respectively.

3.3.8 Conclusion

The results of the synthetic 3D model sensitivity tests show that using 1D velocity models to compute Green's functions for use in long-period (as short as 10 seconds) MT inversions is reasonable, and that at least synthetically we do not find significant bias in solutions, nor issues in being able to discriminate different types of sources. For the DC case, we can recover the correct mechanism and source depth using a universal 1D velocity model for all stations. The ISO component in the full MT is less than 20% for the two DC mechanisms explored. But for the oblique mechanism the inversion recovers a solution with a high CLVD component, resulting in a solution that is 50% DC. The observation of false non-DC components up to 50% for the earthquake source shows that although the correct fault plane solutions for the DC can be recovered at relatively long periods, the CLVD component can be large in full MT inversions, however the NSS remains earthquake-like focused at the origin of the source-type plot. For the explosion cases, the level of false non-ISO is dominated by the ISO-CLVD tradeoff, although the recovered MT consists of a CLVD solution the DC component is less than 10%, and the NSS exhibits the typical explosion-like signature in source-type space (e.g. Ford et al., 2010). Including additional data from first motion polarities can eliminate the trade-off and the correct solution can be recovered. The constrained MT solution is predominantly explosive and has a very low DC of 9%. Similarly, results for the explosive composite source show the tradeoff affects the recoverability of the MTs. The fault plane orientation of the DC component in a composite source cannot be constrained well, except for the case with 50% DC and 50% ISO. Results from synthetic tests using a more heterogeneous 3D model with crustal velocity fluctuations following the von Karman distribution show the full MT inversion can recover the correct DC mechanism. The percentage of non-DC remains the same compared to the result for a smooth model but the solution has higher uncertainties as indicated by lower waveform fits and larger variability in the NSS. When an explosion source is considered the false-DC component increases to almost 50% in the inversion. The NSS exhibits an explosion-like signature in the source-type space but with large variability that extends to a pure DC source. But considering the best solution with first motion constraints shows a predominantly explosive source with a slightly higher DC of 28% compare to the results from a smooth model. The false non-DC components in earthquakes and the false-DC components in explosions arising from unaccounted for 3D path effects can be reduced by using path-specific 1D Green's functions. The Green's functions are computed by taking the average 1D model for each source-receiver path from the 3D tomographic model. Path-calibration also reduces the large uncertainty in the NSS for the oblique mechanism.

Figure 28: (a) Shear wave velocities (Vs) at 5 km depth. Black line denotes the location of the cross section. (b) Cross section of the crustal velocities at depth.
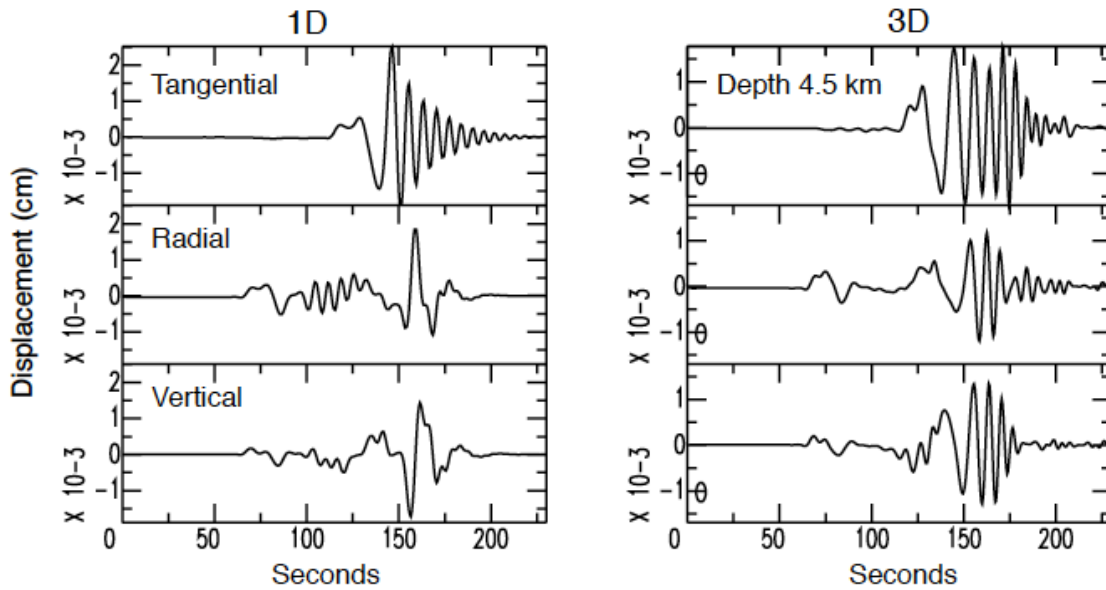
Figure 29: 1D and 3D synthetic waveforms for a normal mechanism (strike=202; rake=−100; dip=36) at SAO. 3D synthetics are computed from the perturbed model.
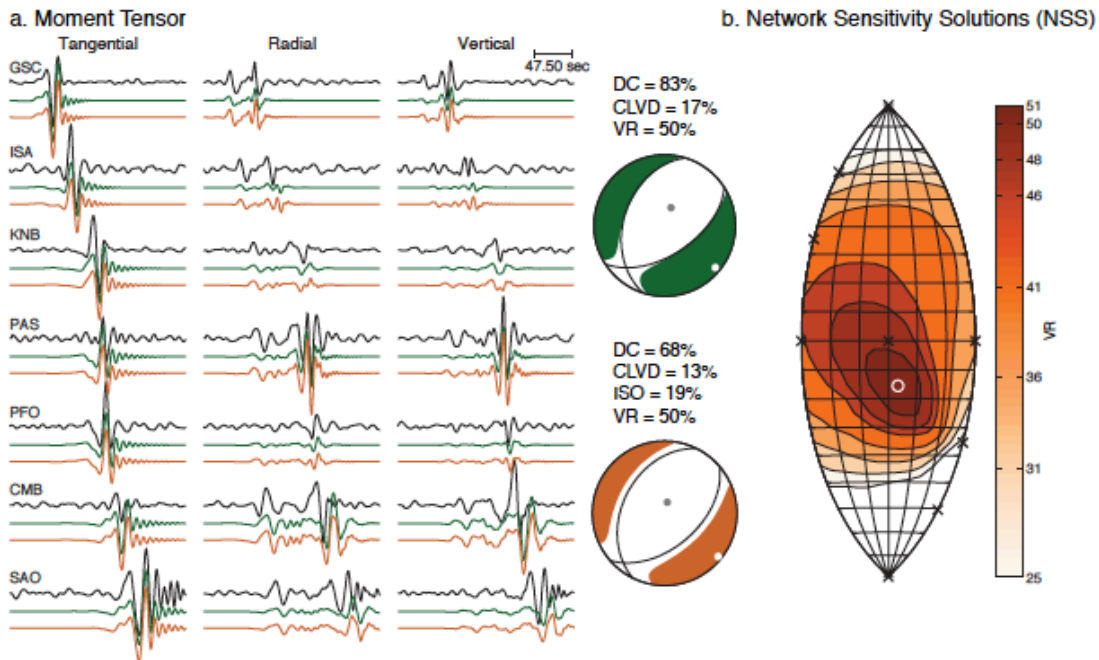
Figure 30: (a) Normal earthquake moment tensor solutions and waveform fits at 10 to 50 seconds. The simulated 3D data using the perturbed model is in black, the deviatoric solution is in green and the full solution is in brown. All waveforms are in displacement (cm). (b) NSS using only waveforms and combined waveforms and first motions. Solutions are color-coded by VR. The white circle represents the location of the best full moment tensor solution in source-type space.
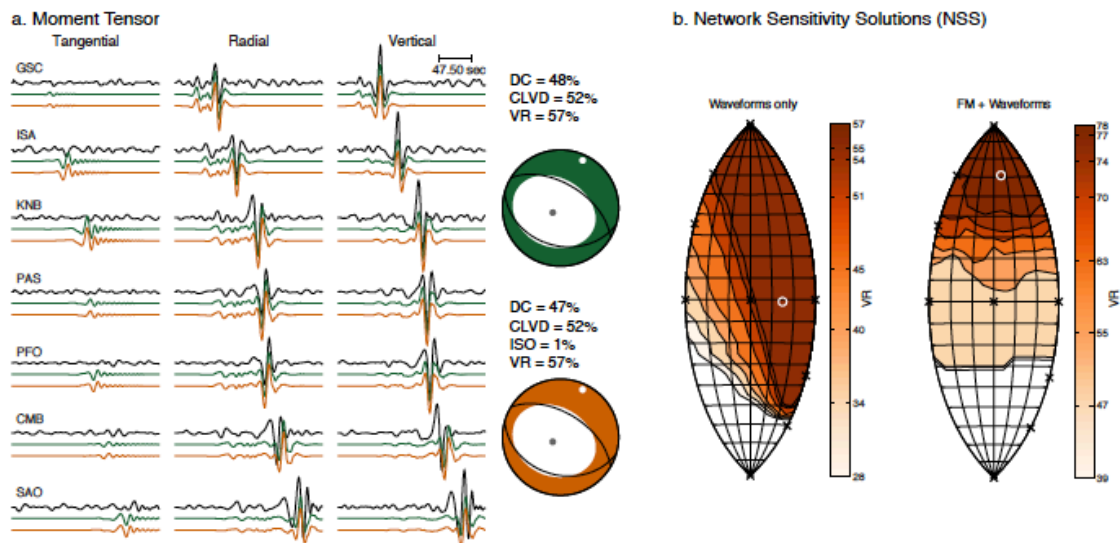
Figure 31: (a) Explosion earthquake moment tensor solutions and waveform fits at 10 to 50 seconds. The simulated 3D data using the perturbed model is in black, the deviatoric solution is in green and the full solution is in brown. All waveforms are in displacement (cm). (b) NSS using only waveforms and combined waveforms and first motions. Solutions are color-coded by VR. The white circle represents the location of the best full moment tensor solution in source-type space.

3.4 Application of 3D Green's Functions on Recovery of NTS Explosion Moment Tensors

3.4.1 Introduction

Obtaining reliable source mechanisms of small magnitude seismic events at regional distance can be challenging due to poor station coverage, high noise levels in the long period waves, or both. Commonly long period waveforms are utilized to minimize errors due to unaccounted Earth structure, but with small magnitude events the signal-to-noise ratios (SNR) of long period waves often degrade rapidly with increasing distance from the source. The need for regional distance monitoring of low yield explosions therefore necessitates the use of shorter period information that may have higher SNR, but which also requires Green's functions (GFs) that account for the more complex short period wave propagation. Recent advancements in waveform modeling and high-performance computing techniques have made the use of source inversions at relatively short periods and structurally complex regions an attractive and viable option, and has been shown in several studies (Ramos-Martínez and McMechan, 2001; Liu et al., 2004; Zhao et al., 2006; Walter et al., 2010; Covellone and Savage, 2012) to be effective. However, there has not been a systematic analysis of the impact of 3D velocity structure on the estimation of seismic source parameters for the purpose of explosion monitoring.

The efficacy of GFs depends on the accuracy of the 3D model. Using a 3D reference model to account for complex wave propagation in and near the Los Angeles Basin, Liu et al. (2004) and Lee et al. (2011) computed source mechanisms of small to moderate-sized earthquakes in Southern California using the spectral element method and finite-difference method, respectively, and found good agreement between the 1D and 3D solutions. Hingee et al. (2011) observe improvements in 3D synthetics over 1D synthetics for some regions in Australia. The reduction in waveform misfit is limited to certain regions suggesting the 3D model for the Australian region needs further improvement. Covellone and Savage (2012) computed deviatoric and full moment tensors (MTs) for 195 $Mw{\sim}5.5$ earthquakes in the Middle East and found little difference among the solutions due to the fact that a large number of observations are available to provide good constraints in the full MT inversion. They compared the deviatoric 1D and 3D MTs and found that there is an improvement in waveform fits and a reduction in the non-double-couple (non-DC) components when using 3D GFs. Although it is important to note that in their comparison study, the 3D synthetics were evaluated against 1D synthetics computed from the preliminary reference Earth model (PREM; Dziewonski and Anderson, 1981).

The focus of most studies has been on earthquakes, the application of 3D source inversions on non-DC events have not been thoroughly investigated. Walter et al. (2010) computed full MT solutions for icequakes near the base of the Swiss Alpine Glacier and determined seismic events are results of near-horizontal tensile cracks. The authors concluded the 1D models provided robust estimates of the source parameters, although the more complex 3D model improved the fits between data and synthetics, particularly for

reflections from the basal moraine and rock. There has not been a systematic study of the effects of 3D GF on the recovery of seismic MT of explosions and the effect on discrimination capability.

The purpose of this study is to develop a platform to perform routine 3D MT inversions and to compare source-type discrimination results for explosions and earthquakes using both 1D and 3D GFs. The same techniques (e.g. Ford et al., 2010) developed to evaluate the quality of 1D models can also be applied to 3D models. Ford et al. (2009a) obtained full MT solutions using a well-calibrated 1D model (Song et al., 1996) for explosions, earthquakes and mine collapses in the western United States. In this study we compare 1D and 3D full MT solutions at two frequency bands: 20 to 50 seconds and 8 to 20 seconds. The high frequency cutoff is limited by the resolution of the Earth model. We use the 3D surface wave tomography model by Moschetti et al. (2010) determined from surface wave dispersion measurements at periods as short as 6 seconds. Of the 32 explosions, earthquakes and collapses previously studied by Ford et al. (2009a), we select six explosions and earthquakes in the vicinity of the former Nevada Test Site (NTS) for source inversions. The events are listed in Table 3 where the earthquake event information comes from the Northern California Seismic Network (NCSN) and the explosion event information comes from Springer et al. (2002). We apply the source-receiver reciprocity principle to compute 3D GFs using the finite-difference (FD) method (Eisner and Clayton, 2001; Graves and Wald, 2001). The advantage of seismic reciprocity is a drastic decrease in computation cost, especially when the number of sources outweighs the number of receivers, because for a set of three FD simulations in which unit forces are applied at the receiver location in the north, east and vertical directions the complete MT GF can be determined at all interior points in the model. Thus in the monitoring of a region it is possible to develop GF over the desired depth range for a calibrated 3D model obtained independently from tomography or other methods.

Table 3: Event Information

Name	Date	Latitude	Longitude	Depth (km)	Magnitude
Amargosa	1996/09/05, 08:16:56.09	36.6827	-116.3378	5000	3.38 (Md)
Little Skull Mt.	2002/06/14, 12:40:45.82	36.6438	-116.3448	8750	4.32 (Md)
METROPOLIS	1990/03/10, 16:00:00.08	37.112	-116.056	469	4.94 (Md)
COSO	1990/03/10, 16:00:00.08	37.104	-116.075	417	4.50 (Md)
HOYA	1991/09/14, 19:00:00.08	37.226	-116.429	658	5.40 (Md)
JUNCTION	1992/03/26, 16:30:00.00	37.272	-116.361	622	4.82 (Md)

3.4.2 Method

We perform the MT inversion in the time-domain using three-component displacement seismograms for receivers located in the western United States (Figure 32). The data are instrument corrected, rotated to the radial, transverse and vertical components and bandpass filtered between 8 to 50 seconds period using an acausal 4-pole Butterworth filter. For the 3D MT inversions, an additional step is taken by convolving the data with the Gaussian source time function used to compute the 3D GFs via the FD method. This is done since it is more stable to convolve the finite-difference source time function with the data, essentially applying a filter, than it is to deconvolve the source time function from the computed Green's functions. We use data recorded at stations from the Berkeley Digital Seismic Network (BSDN), Southern California Seismic Network (SCSN) and the Lawrence Livermore Seismic Network. The United States Geological Survey, Berkeley Seismological Laboratory and California Institute of Technology jointly manage the networks in California. BDSN and SCSN data and instrument responses can be obtained from the Incorporated Research Institutions for Seismology Data Management Center (IRIS DMC, http://ds.iris.edu/ds/nodes/dmc/) and the Northern California Earthquake Data Center (http://www.ncedc.org/).
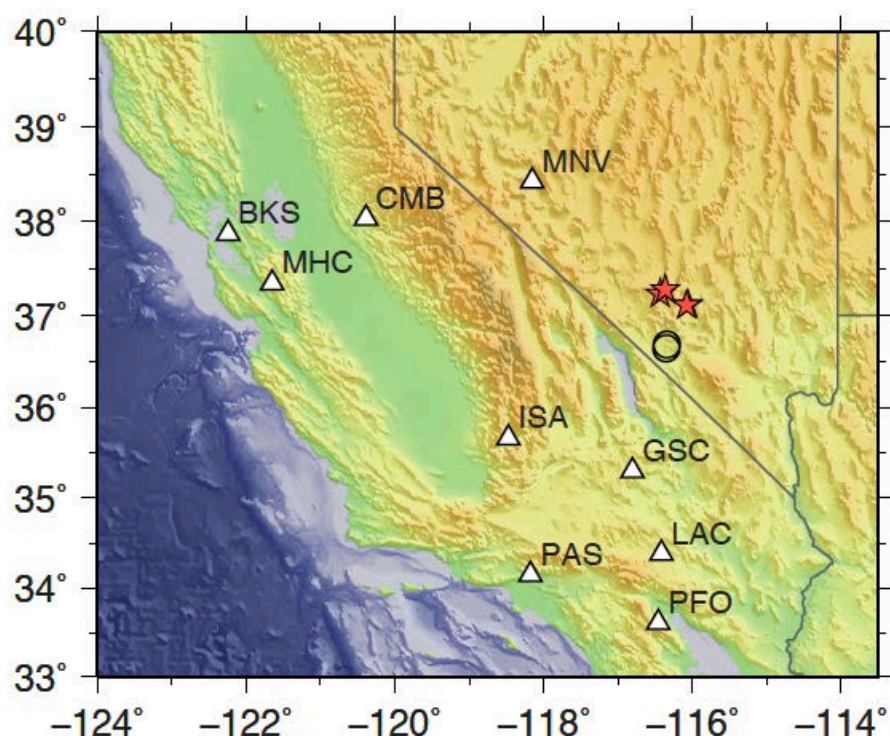
Figure 32: Map of the western United States. Red stars are Nevada Test Site (NTS) explosions, black circles are earthquakes and the white triangles are broadband seismic stations.

3.4.3 Inversion Procedure

The MT inversion follows the method developed by Minson and Dreger (2008) where the complete waveform is inverted in a weighted linear least square formulation. The displacement waveform is expressed as a linear combination of the GFs weighted by the MT elements. The first step is data preparation where the hypocenter and station location are specified, and the data are processed as described in the beginning of this section. After reading the data files, the MT inversion algorithm then loads the pre-computed GFs for each station, and performs a waveform cross-correlation between the data and GF at each station to determine the initial time shifts (Pasyanos et al., 1996). A more detailed description on computing the GF is provided in the next subsection. The time shift that gives the highest correlation between data and GFs is selected (Pasyanos et al., 1996). We do not allow for time shifts greater than half a cycle of the minimum wavelength to avoid cycle shifting. Applying time shifts prior to the actual inversion is a common procedure used to account for imperfect travel time predicted by the model and errors in event origin time. The final step is the inversion where we do not constrain the inversion to have zero trace, instead it solves for all six components of the seismic MT.

3.4.4 Reciprocal Green's Functions

We compute elastodynamic GFs for each source-receiver pair using 1D and 3D Earth models. The GFs are the impulse response whose orientation is given by the basic MT elements or by the fundamental fault types (e.g. Helmberger, 1983; Jost and Herrmann, 1989). The three basic faults types are the vertical dip-slip (DS), 45-degree dip-slip (DD), and vertical strike-slip (SS). Any arbitrary (full) MT can be described as a linear combination of the six basic MT elements (*Mxx, Mxy, Mxz, Myy, Myz, Mzz*), where the first index represents the direction of the force, and the second the direction of a spatial derivative. Thus *Mxx, Myy* and *Mzz* represent the strength of vector dipole forces, and *Mxy, Mxz, Myz, Myx, Mzx* and *Mzy* represent the strength of force couples. Conservation of angular momentum leads to symmetry of the MTs, where *Mxy = Myx*, yielding the 6 independent elements. For the deviatoric MT, where the trace is zero, five basic tensor elements or the three fundamental fault types can describe the seismic tensor (e.g. Langston, 1981; Langston and Helmberger, 1975).

The GFs are computed for each source-receiver pair and processed the same way as the data. The 1D GFs are computed using the western US velocity model (Song et al., 1996) and frequency wavenumber integration method (Wang and Herrmann, 1980; Herrmann and Wang, 1985; Herrmann, 2013). The 3D GFs are computed using the anelastic FD code, SW4, developed at the Center of Applied Scientific Computing at Lawrence Livermore National Laboratory (LLNL; part of the Computational Infrastructure for Geodynamics). The conventional approach to compute 3D GFs using FD is computationally expensive because we need to simulate wave propagation at regional distances with attenuation and at shorter periods. For each receiver, the number of simulations required to compute 3D GFs is six times the number of sources to compute the

six basic MT elements. Therefore to reduce the computation cost we apply the reciprocity principle to compute the 3D GFs. Source-receiver reciprocity for seismic waves is given by the Betti's theorem (Aki and Richards, 2002; Dahlen and Tromp, 1998) which states that the location of the source and observation can be switched but still produce the same exact elastic response. Eisner and Clayton (2001) and Graves and Wald (2001) implemented source-receiver reciprocity using the FD approach to simulate ground motion for any number of arbitrary sources from a set of stations. The advantage of using reciprocity rather than the forward approach is that it is only necessary to run three calculations at every receiver location. Commonly there are fewer stations than sources in a typical monitoring scenario. We compute the elastic response at the source due to a single force in three orthogonal directions (X, Y and Z) at the receiver. For each reciprocal single force the numerical spatial derivative of the displacement in the interior of the model can be computed. Then it is possible to combine the derivatives to construct the individual MT components. For a single force oriented along the X direction:

$$G_{xx}^{X} = \frac{\partial u_x^X}{\partial x}$$

$$G_{yy}^{X} = \frac{\partial u_y^X}{\partial y}$$

$$G_{zz}^{X} = \frac{\partial u_z^X}{\partial z} \qquad (27)$$

$$G_{xy}^{X} = \frac{\partial u_y^X}{\partial x} + \frac{\partial u_x^X}{\partial y}$$

$$G_{xz}^{X} = \frac{\partial u_z^X}{\partial x} + \frac{\partial u_x^X}{\partial z}$$

$$G_{yz}^{X} = \frac{\partial u_z^X}{\partial y} + \frac{\partial u_y^X}{\partial z}$$

There are similar equations for unit forces oriented in the Y and Z directions. We call the elastic response computed via reciprocity the reciprocal Green's functions

(RGF) to distinguish them from the conventional (forward) approach. We can then compute the X component of displacement for an arbitrary source as the weighted sum of the RGFs:

$$u^X = M_{xx}G^X_{xx} + M_{yy}G^X_{yy} + M_{zz}G^X_{zz} + M_{xy}G^X_{xy} + M_{xz}G^X_{xz} + M_{yz}G^X_{yz} \qquad (28)$$

The capitol superscripts refer to the component of motion, which corresponds to the direction of the applied unit force at the receiver position. Given the strike, rake, dip and scalar moment of the fundamental fault types we can compute the M_{ij} coefficients (Eq.1 in Box 4.4 of Aki and Richards, 2002), and substituting them into Eq. 5.2 we can construct the displacement response for each fundamental fault type Green's function for the moment tensor inversion.

The 3D isotropic model by Moschetti et al. (2010) is linearly interpolated in the vertical direction and smoothing is applied in the horizontal direction using Gaussian averaging. The smoothing is necessary because the velocity model is much coarser than the computation grid. For the reciprocal FD calculations we use a grid spacing of 250 m and a Gaussian source function with a duration of 0.5 seconds. We did not include any water layers or topography in the 3D calculations, and implemented attenuation using a function of local Vs [km/s] (e.g. Graves et al., 2008; Olsen et al., 2009), such that Qs = 50Vs and Qp = 2Qs. Figure 33 shows a comparison between a forward FD calculation and a reciprocal calculation. In this case, the source depth is 1 km and the receiver is 100 km away and at the surface. There is excellent agreement between the forward and reciprocal simulations.

The FD calculations were performed on the Livermore Computing Center (LC) 8-core Xeon 35-2670 Linux cluster, cab, consisting of 1,296 nodes, each with 16 cores per node and 32 GB memory. Ideally we should use the same computation domain for all the reciprocal calculations but the run time increases rather quickly at large distances due to a drastic increase in the number of grid points and the duration of the simulation. Because the 3D model is smooth and we are only comparing waveforms as short as 8 seconds, we justify using different computation domains by positioning the source and receivers to be at least 250 grid points away from the boundary and use a sufficiently large absorbing boundary layer (30 km in all directions) to minimize boundary reflections. Running on 512 processors, the run time for one RGF calculation with approximately 1.2 billion grid points and 1,1924 time steps takes about 10 hours.
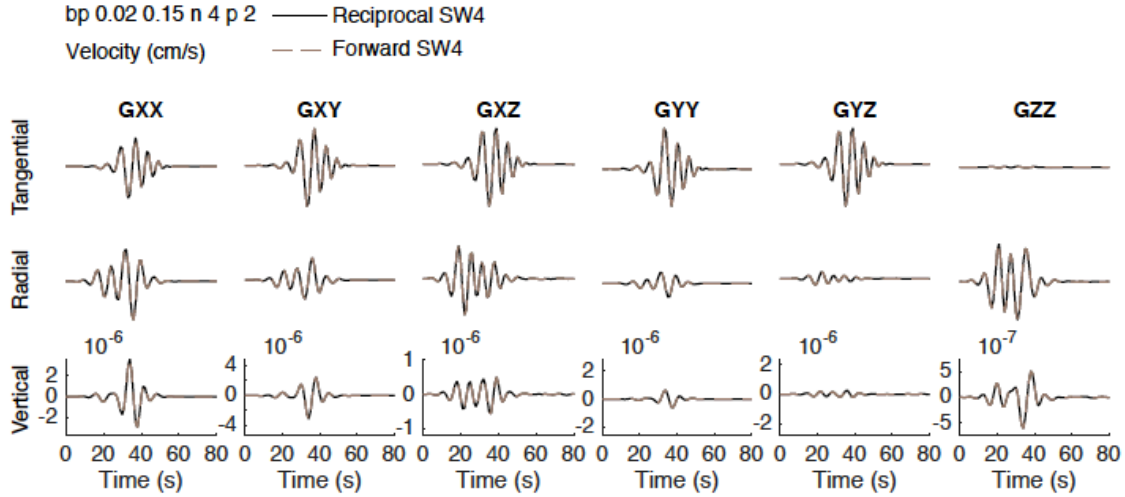
Figure 33: A comparison between forward and reciprocal finite-difference calculations at 100 km distance. The waveforms are in velocity (cm/s) and bandpass-filtered between 0.02 and 0.15 Hz with a 4-pole acausal Butterworth filter. The black lines are the reciprocal calculations and the brown dashed lines are the conventional (forward) calculations.

3.4.5 Moment Tensor Inversion Results

We perform 1D and 3D MT inversion and compute Network Sensitivity Solutions [NSS] (e.g. Ford et al., 2010) for all events. For four out of the six events, we also compare the source properties in two different frequency bands. For the earthquakes (Armagosa and Little Skull Mountain), we search for the best depth using the 1D model and invert for 1D and 3D MT solutions at these depths, whereas for the explosions (METROPOLIS, COSO, HOYA and JUNCTION), we fix the source depth at 1 km for both 1D and 3D GFs. For the comparison at different frequency bands, we use data from the BDSN and SCSN networks, and when available, we also compute solutions including the LLNL network stations but since the raw data and instrument responses for these stations are currently not open we cannot compare the solutions in the different frequency bands.

Low Signal-to-Noise Events

COSO and Amargosa have relatively low SNR compare to the other events in this study, therefore we did not compare the 1D and 3D inversion results at different frequency bands, instead the inversion is done between 10 to 50 seconds. Figure 34a shows the full MT inversion results for COSO. The 1D solution fits the data slightly better than the 3D solution, while the moment magnitude (M_w) using the 3D model is slightly higher than that of the   1D model. Both the 1D and 3D GF inversions recover solutions that are dominated by the explosion component, representing 65% and 68% of the total seismic moment, respectively. On the other hand, the off-diagonal components of the MTs are quite different, where the 1D solution has a deviatoric component that is mostly a normal DC mechanism and the   3D solution is a mixture of vertical DS and CLVD mechanisms. Thus while the

explosive nature of the event is clearly recovered in both cases there is velocity model dependence on the lesser "tectonic" release component of the source.

For the Amargosa earthquake (Figure 34b) the 1D solution is fitting 17% better than the 3D solution, a much greater difference compared to COSO. This is interesting in of itself because it clearly shows that the use of a 3D velocity model, including one that is constrained by data (surface wave dispersion) will not necessarily lead to improved ability to fit the data. The 1D and 3D fault plane orientations are also quite different where the 1D solution is closer to a normal mechanism. In contrast, the 3D solution has a vertical DS component that is significantly rotated with respect to the 1D solution. In addition, the 3D solution results in   a relatively large "false" ISO of 36% of the total seismic moment. However, the ISO component is not statistically significant as determined by the F-test (Menke, 1989; Menke, 2012; Templeton and Dreger, 2006), where the level of statistical significance with the additional degree of freedom in the full MT inversion is only 50%. Nevertheless, this illustrates that imperfect 3D velocity models can also increase the ISO moment in earthquakes, contrary to the results of Covellone and Savage (2012). Although we see an increase in ISO component for short period inversions the 1D (Figure 35a) and 3D NSS (Figure 35b) exhibit a typical earthquake-like signature with a bullseye pattern (Ford et al.,   2010).

Little Skull Mountain Earthquake

The Md 4.3 2002 Little Skull Mountain earthquake occurred near NTS, approximately 6 km southwest of the 1992 Little Skull Mountain mainshock.   At 20 to 50 seconds, we have data from five stations with an azimuthal coverage of $89°$. For the comparison at long period (Figure 36a-c), both 1D and 3D MT solutions fit the data equally well, and have similar mechanisms. The solution is a normal mechanism and is predominantly DC. The DC component for the 3D solution is slightly higher than the 1D solution, and unlike the explosions the 1D solution M_w is higher than the 3D solution.

For the inversion at short period we did not include MHC due to low SNR. Using data from 8 to 20 second yields 1D and 3D MTs with only 50% and 16% DC, respectively (Figure 36a) considerably lower than solutions from the 20 to 50 second passband. The low DC   in the 3D solution is particularly alarming. The 3D solution also recovers a rotated normal mechanism with respect to long period MTs (about 40 degrees).   The M_w is similar for   all solutions and the 1D model performs better than the 3D model mainly because the 3D model cannot fit the tangential component as well as the 1D model (Figure 36d-e). We also see an increase in variance at CMB using the 3D model. We identify ISA to be a problematic station in the 3D inversion because the synthetics cannot fit the data well with time shifts less than half the minimum wavelength (4s). Therefore the solution with the highest VR within the 4-second window is a solution with zero shifting. Considering a three-station inversion without ISA (Figure 37) we obtain a solution with 52% DC and a normal mechanism consistent with long period MTs and the 1D short period MT.

a. COSO

	FULL MT	Deviatoric	Mw	DC	CLVD	ISO	VR
10–50s 1D			3.57	30%	4%	65%	40% (40%)
3D			3.98	21%	11%	68%	36% (35%)

b. Amargosa

	FULL MT	Deviatoric	Mw	DC	CLVD	ISO	VR
10–50s 1D			3.65	85%	2%	13%	58% (58%)
3D			3.61	43%	22%	35%	41% (39%)
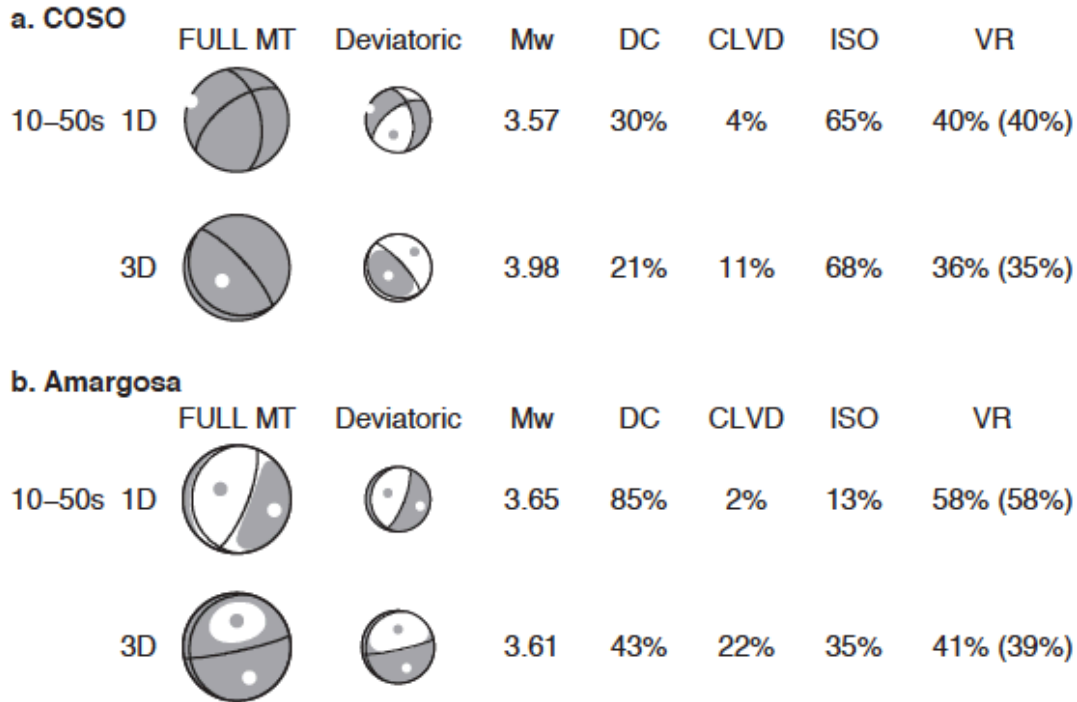
Figure 34: COSO and Amargosa full moment tensor inversion results with 1D and 3D Green's functions filtered between 10 to 50 seconds. Full moment tensor focal mechanism and the deviatoric component of the solution are plotted as well as the moment magnitude (M_w), percent double-couple (DC), percent compensated linear vector dipole (CLVD), percent isotropic (ISO) and variance reduction (VR). VR from deviatoric inversion is in parentheses.

Whether or not we include ISA in the 3D MT inversion, the ISO component remains high, up to 40%, which is quite large for an earthquake. However the F-test reveals the ISO component is not statistically significant with a 50% confidence level of significance for inversions with and without ISA. In addition, 1D (Figure 38a) and 3D NSS (Figure 38b-c) all exhibit an earthquake-like distribution and similar level of solution uncertainty where the normalized VR≥95% (67%, 43% and 54%, respectively) are about the same size. Similar to Amargosa, the results show that imperfect 3D velocity models can also increase the ISO moment in earthquakes.

Larger NNSS (NTS) Explosions

We compare 1D and 3D MT inversions for three NTS explosions METROPOLIS, HOYA and JUNCTION. Of the three explosions HOYA has strong SH radiation on the tangential component, indicative of a larger tectonic release. For METROPOLIS we have data from three stations PAS, CMB and MHC where we can compare the solutions at different frequency bands. Additionally, we are able to compute a solution including two additional stations, MNV and LAC from the LLNL network, increasing the azimuthal

coverage from 75˚ to 123˚. Data from MNV and LAC are filtered between 10 to 30 seconds. PAS and CMB have high SNR at both long and short periods whereas MHC has relatively noisy data at long periods for the two horizontal components, but relatively high SNR for the vertical component. At 20 to 50 seconds, we see very little SH energy in the tangential component and essentially none at CMB. The deviatoric part of the solution is very similar for both 1D and 3D MTs; however, the 3D solution has a much higher ISO component, 16% higher than the 1D solution (Figure 39a). Again, the 3D solution has a higher Mw that is closer to the reported magnitude (Md) in the catalog (Table 5.1). Although the VR improved slightly for all three stations from 1D to 3D (Figure 39b-c) the increase is only a few percent. At 8 to 20 seconds, the ISO component of the 3D solution decreased to 59%, in contrast the ISO component of the 1D solution, which increased to 81%. The deviatoric part of the solution changed significantly from long period to short period, instead of a reverse sense of motion for both solutions at long periods, at short periods the 1D solution is mostly DS and the 3D solution has a large CLVD component. In terms of waveform fits (Figure 39d-3) overall the 1D model is fitting the data better than the 3D model due to significant increase in VR at CMB. On the other hand, the 3D model performs better along the path to MHC. Mw decreased for both solutions from the long period case to short period case, but again the 3D solution has a higher Mw. The best solution is the inversion using data from five stations and filtered between 10 to 50 seconds (Figure 39a). Both 1D and 3D results have high ISO components and similar mechanisms for the off-diagonal components. Mw for the 3D solution is 0.3 magnitude units higher than the 1D solution, and overall the 3D model is fitting a few percent better than the 1D model.
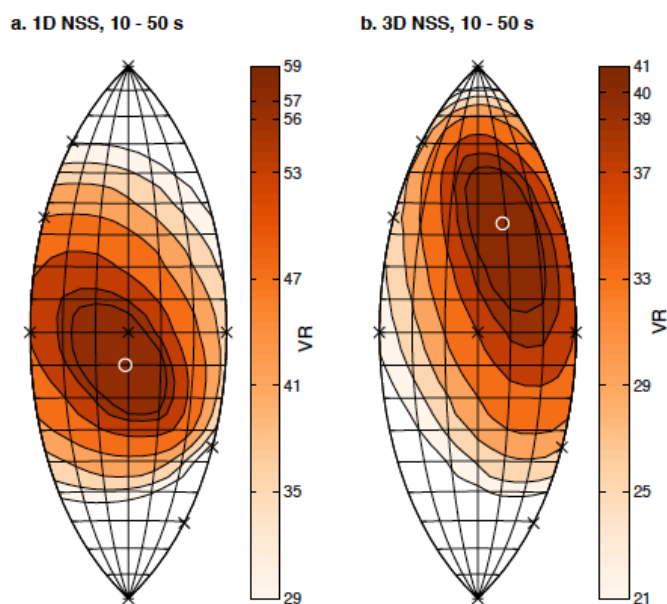
Figure 35: Amargosa NSS for (a) 1D and (b) 3D Green's functions filtered between 10 to 50 seconds. White circle marks the location of best full moment tensor in source-type space.

Figure 36: 2002 Little Skull earthquake full moment tensor inversion results with 1D and 3D Green's functions and at different frequency bands. (a) Full moment tensor focal mechanism and the deviatoric component of the solution are plotted as well as the moment magnitude (M_w), percent double-couple (DC), percent compensated linear vector dipole (CLVD), percent isotropic (ISO) and variance reduction (VR). VR from deviatoric inversion is in parentheses. (b-e) Data (solid line) and synthetic waveforms (dashed line) plotted from left to the right are the tangential, radial and vertical components.

a. 2002 Little Skull Mountain Moment Tensor Solutions (3-station)

	FULL MT	Deviatoric	Mw	DC	CLVD	ISO	VR
8–20s 3D			4.51	52%	12%	36%	57% (55%)

b. 3D 8-20s

GSC, 144 km, 197°, VR=69

32.00 sec

PAS, 313 km, 212°, VR=67

32.00 sec

CMB, 395 km, 296°, VR=45

32.00 sec

Tangential   Radial   Vertical
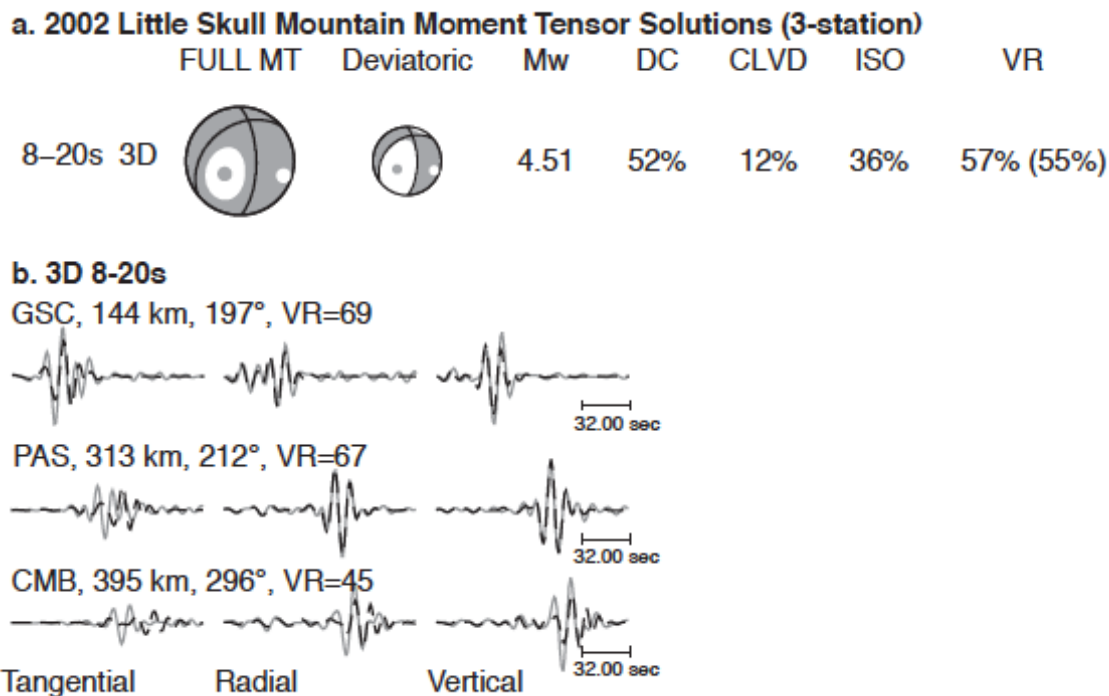
Figure 37: 2002 Little Skull earthquake three-station inversion using 8 to 20 second 3D Green's functions. (a) Full moment tensor focal mechanism and the deviatoric component of the solution are plotted as well as the moment magnitude (M_w), percent double-couple (DC), percent compensated linear vector dipole (CLVD), percent isotropic (ISO) and variance reduction (VR). VR from deviatoric inversion is in parentheses. (b) Data (solid line) and synthetic waveforms (dashed line) plotted from left to the right are the tangential, radial and vertical components.

Unlike the other explosions in this study, HOYA has strong Love wave energy across all stations. The data also have high SNR in the frequency band we examined and better station coverage compare to the other explosions. The azimuthal coverage for HOYA is 100° for the five-station inversion, and the best solution including two additional LLNL stations MNV and LAC has an azimuthal coverage of 132°. For solutions from 20 to 50 seconds (Figure 40a-c), the ISO component is around 60% for both velocity models; however the 3D solution has a larger DC component and a higher Mw. The non-ISO mechanism is quite different between the two models, the 1D case is a normal mechanism and the 3D case is a vertical DS mechanism. The 3D model fits the data better than the 1D model. As seen in Figure 40b-c the amplitudes between the data and synthetics at stations PAS, PFO and BKS are in better agreement when we use a 3D model.
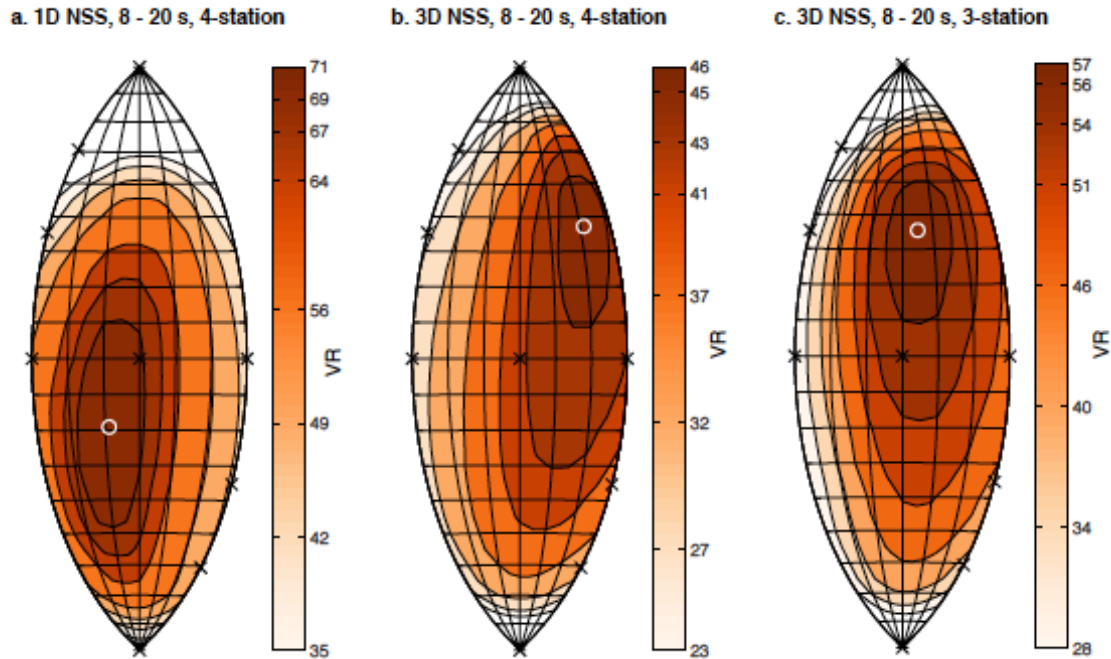
Figure 38: 2002 Little Skull Mountain NSS using 8 to 20 second Green's functions for (a) 1D 4-station inversion, (b) 3D 4-station inversion and (c) 3D 3-station inversion. White circles mark the location of best full moment tensor in source-type space.

From 8 to 20 seconds (Figure 40a,d-e) the 3D solution has an ISO component of 73% whereas the 1D solution has an ISO component of 54%. The 3D model cannot fit the data well on the tangential components at all stations except for BKS. We can see the waveform fits are significantly better along the path to BKS when using 3D GFs instead of 1D GFs, resulting in higher overall VR for the 3D solution. At short periods the deviatoric part of the solution has a different mechanism compared to the long period solutions. Although the 3D case still consists of a vertical DS mechanism the fault orientation has rotated about 45° towards the southwest. In contrast to the other explosions the M_w is slightly higher when using 1D GFs at short periods. The long period solutions are more consistent with the seven-station inversion because the frequency band used for the best solution is between 10 to 50 seconds. We use inverse variance weighting instead of inverse distance weighting for the seven-station inversion because data from MNV and LAC are filtered between 10 to 30 seconds, resulting in higher amplitudes, while the rest of the stations are filtered between 20 to 50 seconds. For the seven-station inversion, the 3D solution has a higher M_w and ISO component, and a vertical DS mechanism instead of a normal mechanism for the deviatoric part of the full MT.

For JUNCTION, we have data from four stations BKS, PAS, PFO and ISA for the comparison at different periods, and there is an additional LLNL station LAC in the five-station inversion. For the five-station inversion, all data from the BDSN and SCSN network stations are filtered between 10 to 50 seconds and LAC is filtered between 10 to 30 seconds. Comparing the results at 20 to 50 seconds (Figure 41a) full MT solutions using either model

have excellent waveform fits; the 3D solution has a VR of 95% and the 1D model has a VR of 83%. VR increases for all stations using 3D GFs but the biggest improvements are along the paths to BKS and PFO (Figure 41b-c). Similar to HOYA, the amplitudes between data and synthetics on the radial and vertical components agree well when 3D GFs are used but not   as well on the tangential component for BKS and PFO. Both solutions are predominantly ISO but the 3D solution has an ISO component 17% higher than the 1D solution. Mw from the 3D solution is also higher than the 1D case. The deviatoric component of the solutions have different fault orientations and sense of motion between the 1D and 3D case; the 1D solution consists of a normal mechanism and the 3D solution consists of a CLVD mechanism with the major vector dipole in tension   (+CLVD).

Comparing the solutions at periods between 8 and 20 seconds, we see again that the paths to BKS and PFO are well modeled using 3D GFs, which are consistent with the results at long periods. However, the VR decreases for the paths to ISA and PAS when using 3D GFs (Figure 41d-e). Different than the results at long period, the 1D solution has a larger ISO component of 75% while the 3D solution has an ISO component of 69%. The non-ISO part of the MT consists of a DS mechanism but with different orientations between 1D and 3D cases. Jackknife resampling of different station combinations shows PAS is a key station in the inversion at short period, the ISO component decreases when we remove PAS, especially for the 1D case where the ISO disappears and the solution is a CLVD mechanism with the major vector dipole in compression ($-$CLVD). The best solution using data from five stations are mostly ISO but for the 1D case the ISO component is reduced to 56%. In terms of M_w, the 3D solution overestimates the magnitude when we compare it to the reported ML in Springer et al. (2002). The deviatoric part of the solution comprises of a vertical DS mechanism for the 1D case and a +CLVD mechanism for the 3D case. The drop in VR for the   1D solution is due to lower fits at station LAC whereas all other stations have VR above 70%.
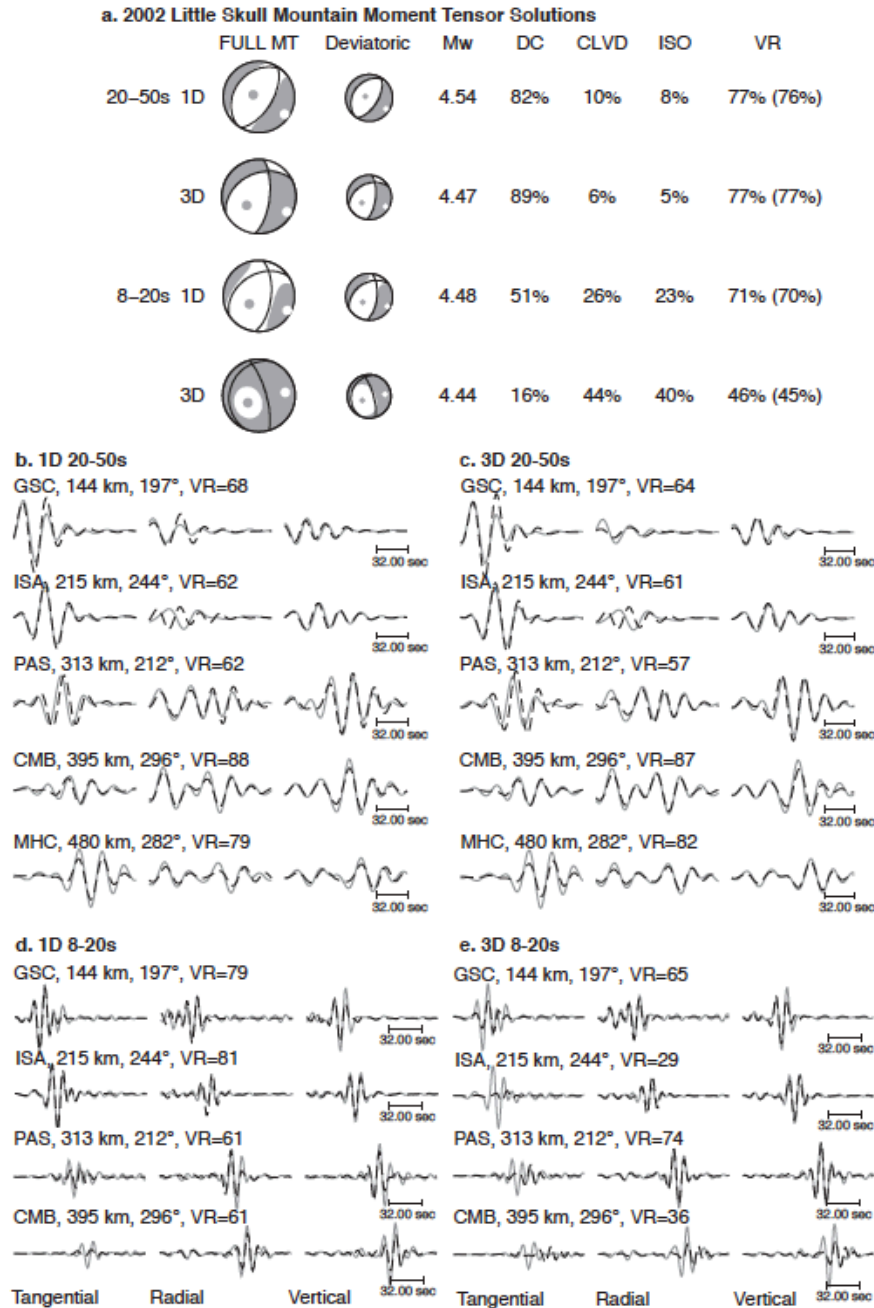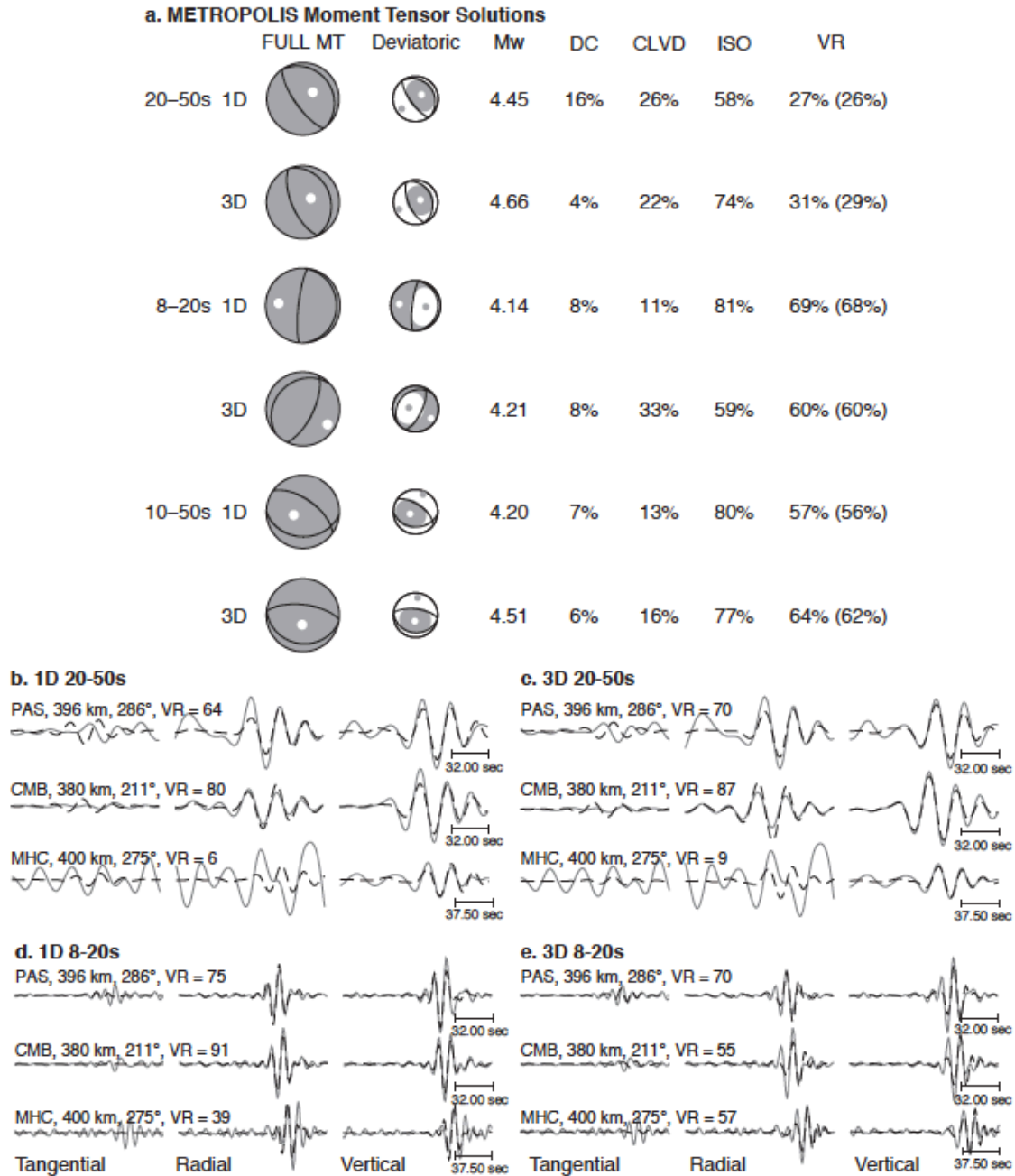
Figure 39: METROPOLIS full moment tensor inversion results with 1D and 3D Green's functions and at different frequency bands. (a) Full moment tensor focal mechanism and the deviatoric component of the solution are plotted as well as the moment magnitude (M_w), percent double-couple (DC), percent compensated linear vector dipole (CLVD), percent isotropic (ISO) and variance reduction (VR). VR from deviatoric inversion is in parentheses. (b-e) Data (solid line) and synthetic waveforms (dashed line) plotted from left to the right are the tangential, radial and vertical components.
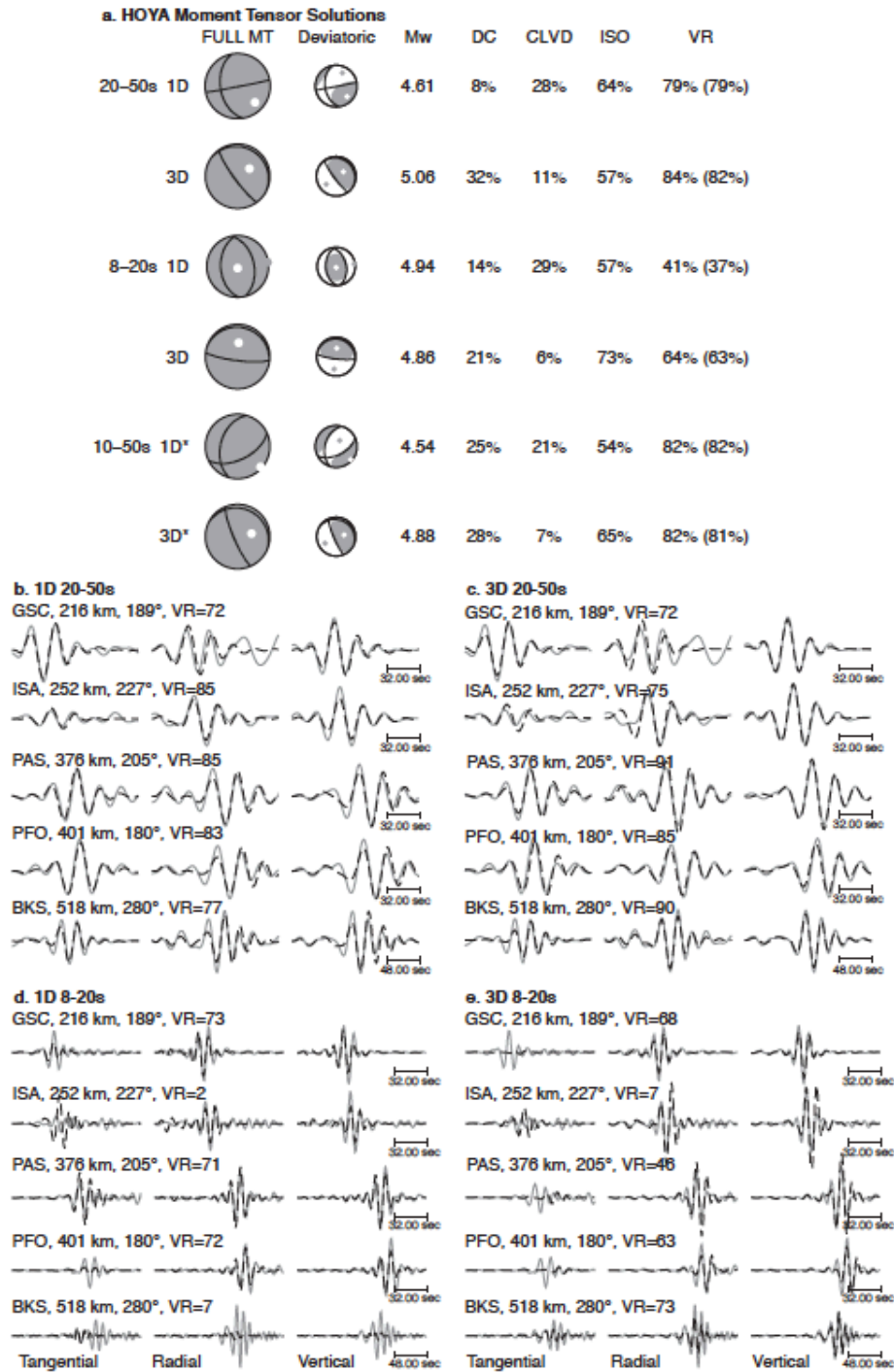
Figure 40: HOYA full moment tensor inversion results with 1D and 3D Green's functions and at different frequency bands. (a) Full moment tensor focal mechanism and the deviatoric component of the solution are plotted as well as the moment magnitude (M_w), percent double-couple (DC), percent compensated linear vector dipole (CLVD), percent isotropic (ISO) and variance reduction (VR). VR from deviatoric inversion is in parentheses. (b-e) Data (solid line) and synthetic waveforms (dashed line) plotted from left to the right are the tangential, radial and vertical components.

a. JUNCTION Moment Tensor Solutions

		FULL MT	Deviatoric	Mw	DC	CLVD	ISO	VR
20–50s	1D			4.40	30%	6%	64%	83% (82%)
	3D			4.79	7%	12%	81%	95% (93%)
8–20s	1D			4.42	7%	20%	74%	47% (46%)
	3D			4.69	26%	5%	69%	70% (69%)
10–50s	1D			4.70	27%	16%	56%	68% (66%)
	3D			5.02	4%	21%	76%	87% (78%)

b. 1D 20-50s

BKS, 523 km, 279°, VR=76

ISA, 260 km, 227°, VR=93

PAS, 383 km, 206°, VR=81

PFO, 406 km, 181°, VR=79

c. 3D 20-50s

BKS, 523 km, 279°, VR=94

ISA, 260 km, 227°, VR=97

PAS, 383 km, 206°, VR=96

PFO, 406 km, 181°, VR=92

d. 1D 8-20s

BKS, 523 km, 279°, VR=3

ISA, 260 km, 227°, VR=85

PAS, 383 km, 206°, VR=81

PFO, 406 km, 181°, VR=69

Tangential   Radial   Vertical

e. 3D 8-20s

BKS, 523 km, 279°, VR=68

ISA, 260 km, 227°, VR=64

PAS, 383 km, 206°, VR=76

PFO, 406 km, 181°, VR=72

Tangential   Radial   Vertical
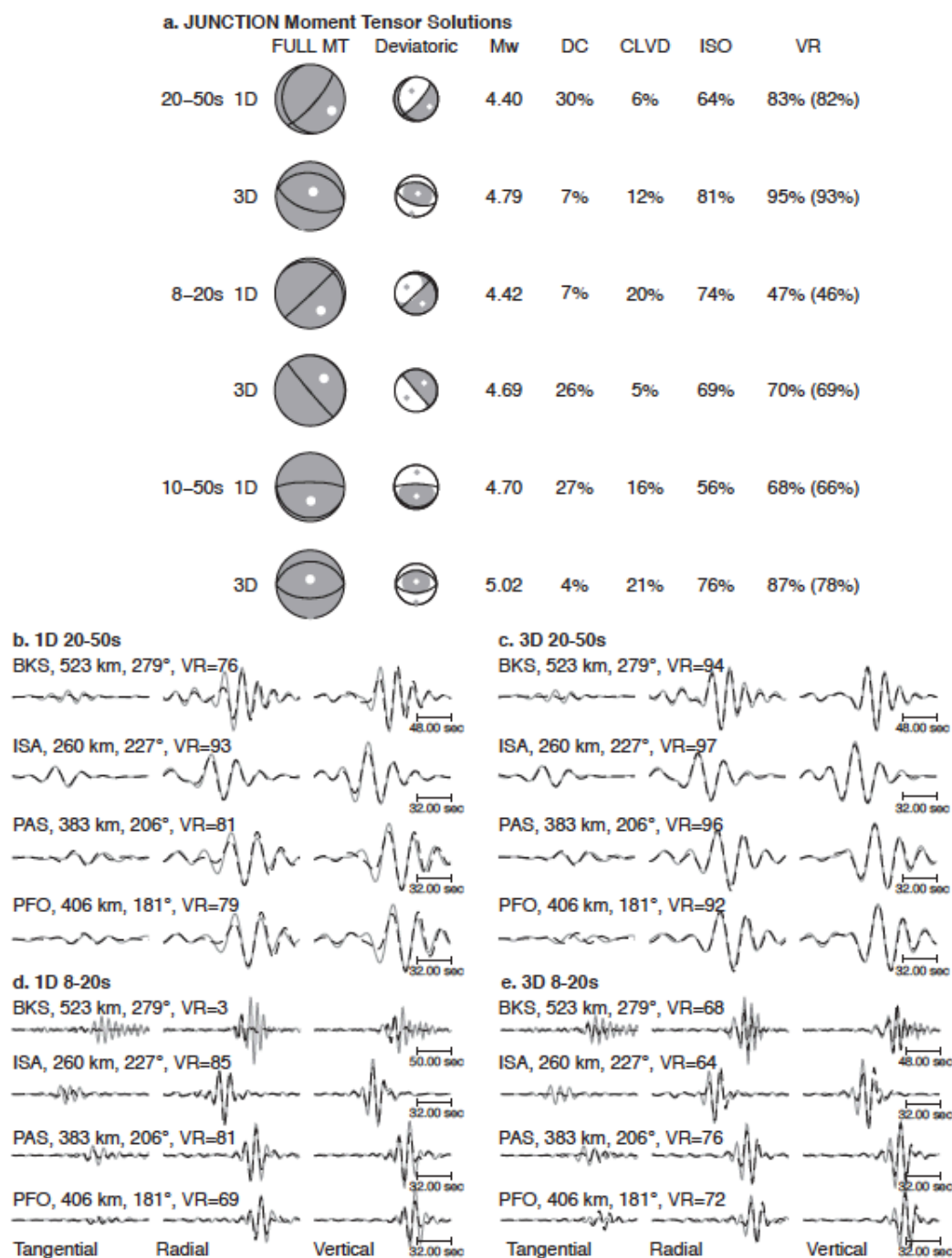
Figure 41: JUNCTION full moment tensor inversion results with 1D and 3D Green's functions and at different frequency bands. (a) Full moment tensor focal mechanism and the deviatoric component of the solution are plotted as well as the moment magnitude (M_w), percent double-couple (DC), percent compensated linear vector dipole (CLVD), percent isotropic (ISO) and variance reduction (VR). VR from deviatoric inversion is in parentheses. (b-e) Data (solid line) and synthetic waveforms (dashed line) plotted from left to the right are the tangential, radial and vertical components.

Comparison in Source-Type Space

Network Sensitivity Solutions (NSS) utilizing source-type representations proposed by Hudson et al. (1989) and Tape and Tape (2012a) and Tape and Tape (2012b) have been developed and used in previous studies to estimate uncertainties in source inversions (e.g. Ford et al., 2010; Guilhem et al., 2014; Chiang et al., 2014; Nayak and Dreger, 2015). We would like to compare the estimated uncertainties in the source-type space between 1D and 3D GFs to see if the 3D model reduces the source-type uncertainties, therefore providing better constraints on source mechanisms and increasing confidence in discrimination. We compute the NSS for Little Skull Mountain, METROPOLIS, HOYA and JUNCTION using the same station configuration and filter parameters in the MT inversion analysis. The results comparing 1D and 3D NSS at two frequency bands are presented in Figure 42, where we plotted solutions with normalized VR≥95%. The comparison for the 2002 Little Skull Mountain earthquake shows at long periods (20-50 seconds) the spread of the MT uncertainties are larger using 3D GFs, but at short periods (8-20 seconds) the spread is about the same between the two models. If we look at the distribution of the source-type parameters γ and δ (Figure 43a) we see a wider distribution in the volumetric component (δ) of the MT when inverting using 3D GFs. At higher frequencies, the two NSS populate different areas of the source-type space; the 3D NSS extends into the region of positive volume change while the 1D NSS extends into the region of negative volume change. There are noticeable shifts in the mean of the distributions for both 1D and 3D NSS (Figure 43a), where the distributions at short periods deviate away from a pure DC mechanism. For the explosions, 1D and 3D NSS (Figure 42) at long periods show the spread of the estimated uncertainties associated with source inversion varies between events: the uncertainties for JUNCTION are similar using either 1D or 3D GFs, for HOYA the solutions are better constrained using 3D GFs but the results are opposite for METROPOLIS. At short periods we see little difference between the 1D and 3D NSS, except for HOYA where the solution is very well-constrained using 1D GFs. The distribution of γ and δ for explosions are negative skewed (Figure 43b) meaning they have a long tail in the negative direction, for both 1D and 3D models and at both long and short periods, the exception is the HOYA 1D NSS where γ is positive skewed resulting in a population of solutions near the theoretical explosion/opening crack mechanisms. All explosion NSS have a mean δ around 30° and we do not see a large difference in the mean δ values between 1D and 3D NSS.
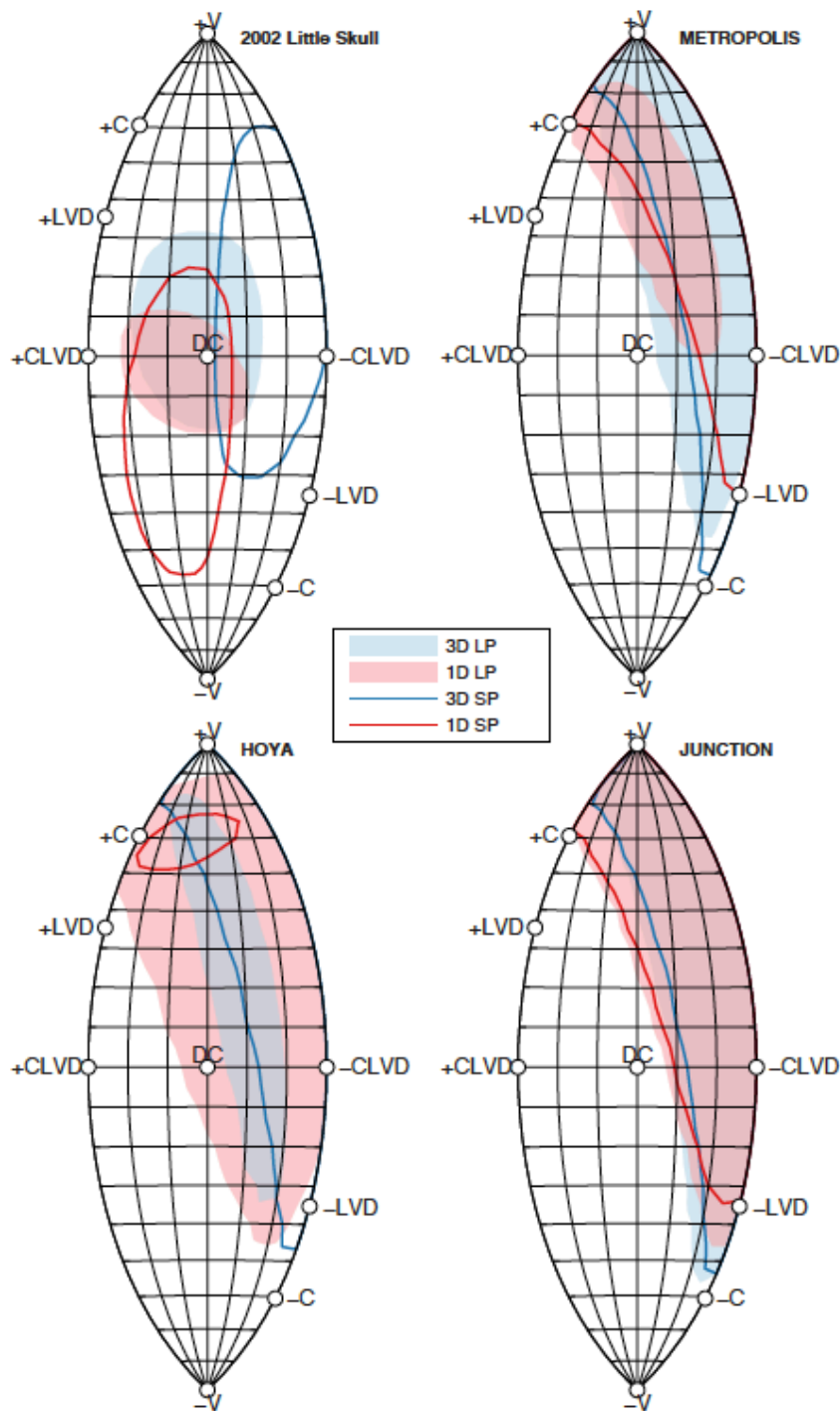
Figure 42. Comparison of Network Sensitivity Solution (NSS) of four different events: 2002 Little Skull earthquake, METROPOLIS, HOYA and JUNCTION. The shaded regions and contour lines show the populations of solutions with normalized VR≥95% for long period and short period waveform inversions, respectively. The blue and pink colors are solutions computed using 3D and 1D Green's functions, respectively.
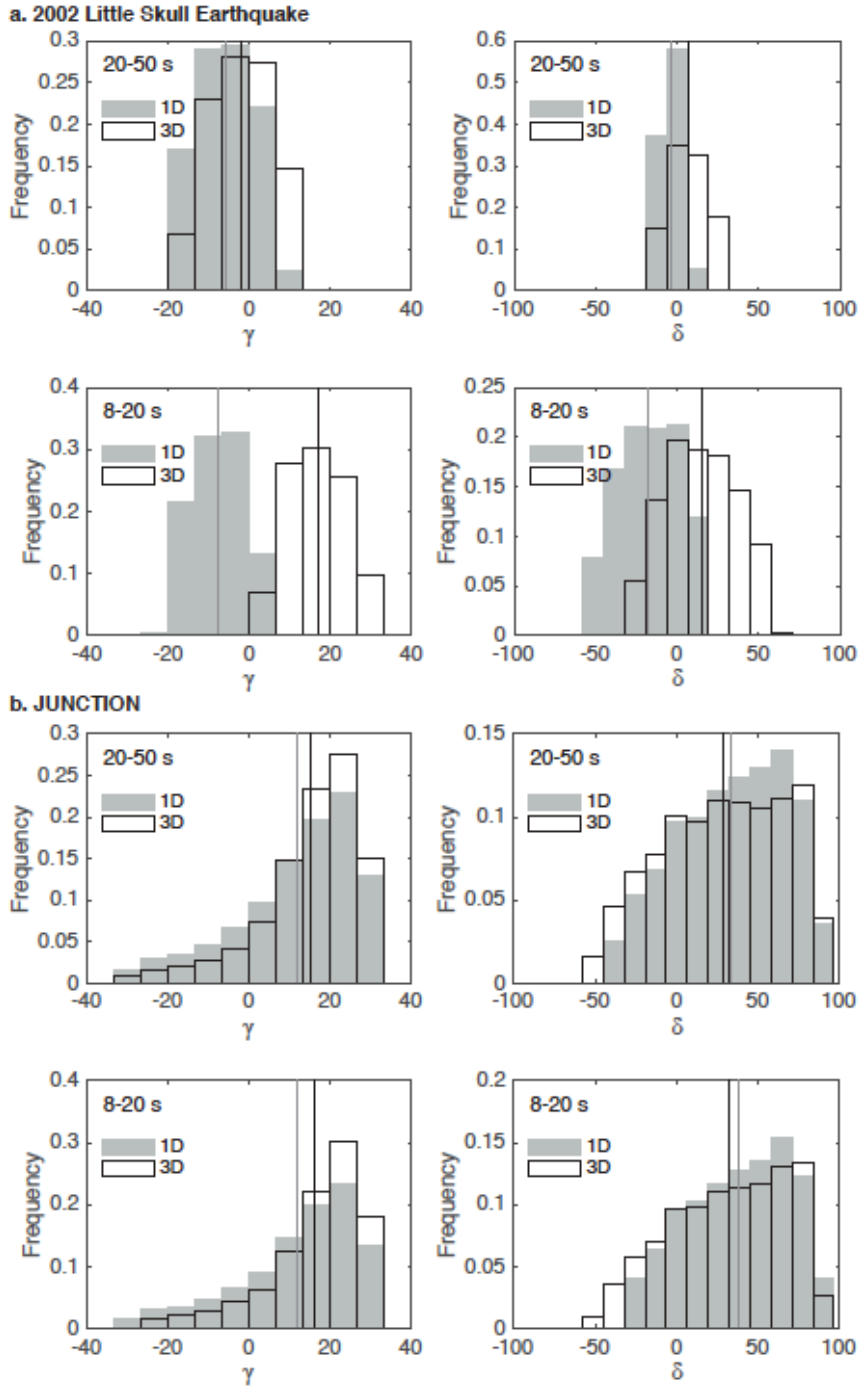
Figure 43: Comparisons of source-type parameters γ and δ for two events (a) 2002 Little Skull Mountain earthquake and (b) NTS explosion JUNCTION. Histograms show γ and δ from waveform inversions at two frequency bands, the gray bars represent the use of 1D Green's functions, the white bars represent the use of 3D Green's functions, and the gray and black lines are the mean values from 1D and 3D inversions, respectively.

3.4.6 Discussion

Comparisons between 1D and 3D source inversions show differences in source mechanism in both the long period and short period cases. For the 20 to 50 second case, the 1D and 3D solutions for the 2002 Little Skull Mountain earthquake show minimal difference in source mechanism and magnitude. In contrast, the explosions show an increase in magnitude and waveform fits from 1D to 3D inversions. The off-diagonal components are not well-constrained and vary depending on the frequency band and velocity model used. Contrary to Hingee et al. (2011) and Covellone and Savage (2012), where MT solutions were compared from 40 to 200 seconds and 25 to 125 seconds, respectively, in general we see a reduction in waveform fits for the 3D inversions at relatively short periods (8 to 20 seconds) and for the two earthquakes we see an increase in non-DC components, suggesting finer details of the Earth's structure may not be well-represented by the 3D model. The exceptions are the paths to BKS and MHC, particularly BKS, where we see significant improvements in waveform fits when 3D GFs are used in the short period inversions. Paths crossing the extensional regimens and low velocity sediments (Figure 44a) are better represented by the 3D model, where stations BKS and MHC are situated on top of the low velocity zone (Figure 44b). Based on the four events analyzed in this study, the long period time domain MT inversion results in higher waveform fits when 3D GFs are applied, however we do not see a significant reduction in uncertainties associated with the MT using synthetics derived from the 3D model. JUNCTION has little difference in source uncertainties between the 1D and 3D case, Little Skull Mountain and METROPOLIS show higher uncertainties for the 3D case whereas HOYA shows lower uncertainties for the 3D case. A larger sample size is required to make more useful interpretations about the use of 3D models in estimating MT source uncertainties.
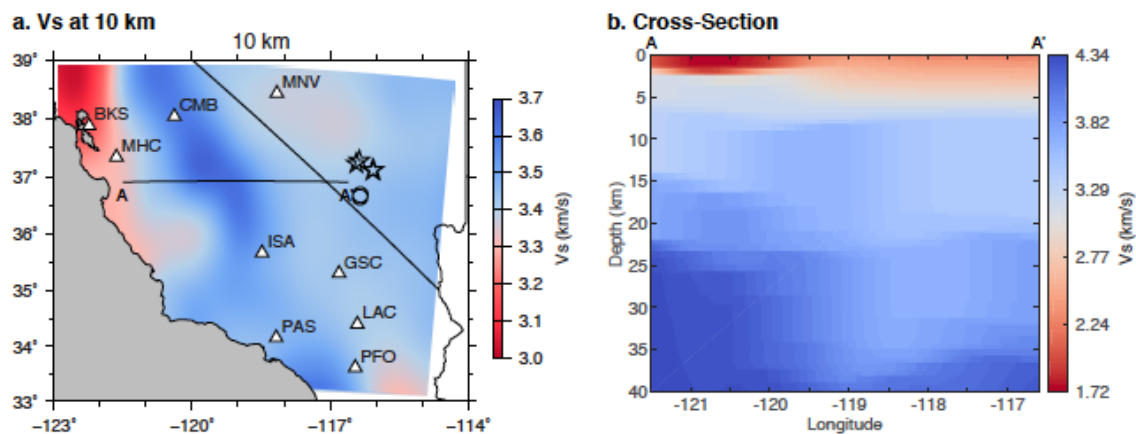
Figure 44: (a) Vs at 10 km depth where surface waves are most sensitive to the structure at these period ranges. (b) A cross-sectional view of crustal and upper mantle velocities across A-A'.

Moschetti et al. (2010) noted the surface wave model has larger uncertainties in shear wave speeds in extensional regions across the western US, near the Moho (lower

crust) and the shallowest parts of the crust. There is a significant trade-off between crustal thickness and shear wave speed resulting in an increase in shear wave uncertainties around the Moho (between 35 to 45 km depth). In our 3D short period inversions, Rayleigh waves are fitting better than the Love waves. The 3D model used was determined using dispersion data from Rayleigh wave group and phase velocities and Love wave phase velocities, Love wave group velocities are not included due to large uncertainties. Also, the Love wave dispersion maps are in period bands of 8 to 32 seconds whereas the Rayleigh wave dispersion maps are in period bands of 6 to 40 seconds. Therefore in addition to a priori constraints on sediment and crustal thicknesses (Laske and Masters, 1997; Gilbert and Fouch, 2007) the details of the 3D model were constrained mostly by short period Rayleigh wave data. In comparison, Hingee et al. (2011) used a 3D radially anisotropic model constructed from full waveform tomography. The full waveform model (Fichtner et al., 2009 and 2010) is derived from a large variety of observations including both surface waves and body waves. They also implemented a realistic 3D Q model by Abdulah (2007). Covellone and Savage (2012) also used a 3D model (Kustowski et al., 2008) computed from a combination of data sets that included surface wave phase velocity measurements, long period waveforms and body wave travel times. This suggests tomography models derived from full waveform modeling are preferred for short period inversions.

Since our results indicate the use of 3D GFs at short periods has limited benefit for the particular 3D model that was employed, a more attractive option to evaluate 3D models than the costly 3D simulations may be using path-averaged 1D velocity models derived from the 3D model. We compute MTs for Little Skull Mountain, HOYA and JUNCTION using 1D averaged velocity models for each source-receiver path. In general, the averaged structures have a Moho ranging from 30 to 37 km and a very thin low velocity layer (<1 km thick) when compared to the 1D Song et al. (1996) model. Here we present results for Little Skull Mountain (Figure 45) and HOYA (Figure 46). Overall the MT solutions from 20 to 50 seconds Figure 45a-b and Figure 46a-b are similar to previous 1D and 3D MTs, the differences are in the short period inversions. For JUNCTION the results are similar to the 3D inversion except the path to BKS cannot be modeled by the averaged 1D structure, and the solution has a lower ISO of 52%. For Little Skull Mountain, the short period inversion with averaged 1D models have better fits to the data at ISA and CMB, however the resulting mechanism is an incorrect oblique strike-slip earthquake (Figure 45a). The overall lower goodness of fit with averaged 1D MTs and 3D MT suggest paths from Little Skull Mountain to the stations need further refinement. For HOYA, the averaged 3D structure is actually a better representation for the paths to GSC, ISA and PFO, the fits to the data at these stations are higher compare to the 3D solution due to better agreement in the Love waves; whereas again the paths to BKS cannot be modeled by the path-averaged 1D model. 1D and 3D comparisons indicate that, in many cases, well-calibrated average 1D representations of the Earth structure may be a more attractive option at periods as short as 8 seconds, but 3D models do need to be considered as shown by the modeling results for the path to BKS.
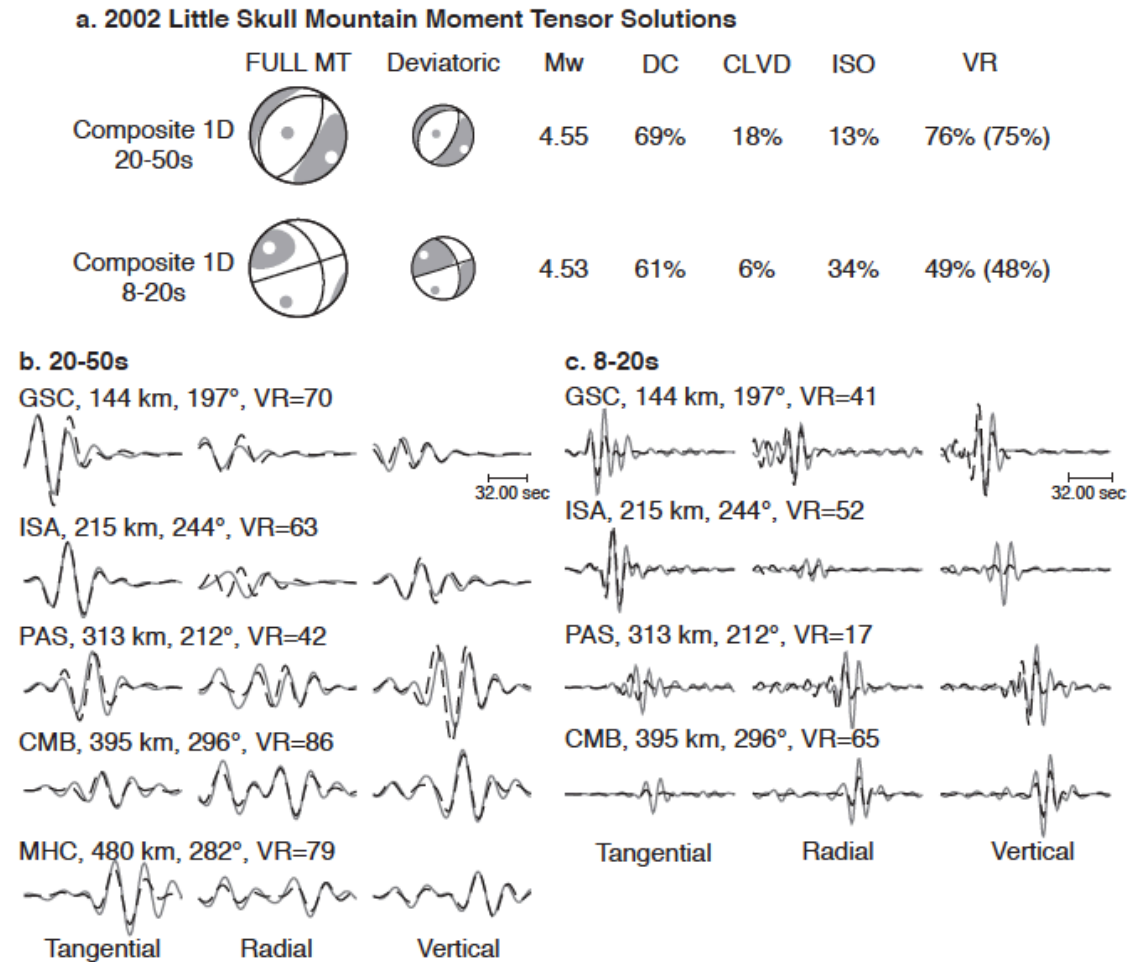
Figure 45: 2002 Little Skull Mountain full moment tensor inversion results with path averaged 1D Green's functions at different frequency bands. (a) Full moment tensor focal mechanism and the deviatoric component of the solution are plotted as well as the moment magnitude (M_w), percent double-couple (DC), percent compensated linear vector dipole (CLVD), percent isotropic (ISO) and variance reduction (VR). VR from deviatoric inversion is in parentheses. (b-c) Data (solid line) and synthetic waveforms (dashed line) plotted from left to the right are the tangential, radial and vertical components.
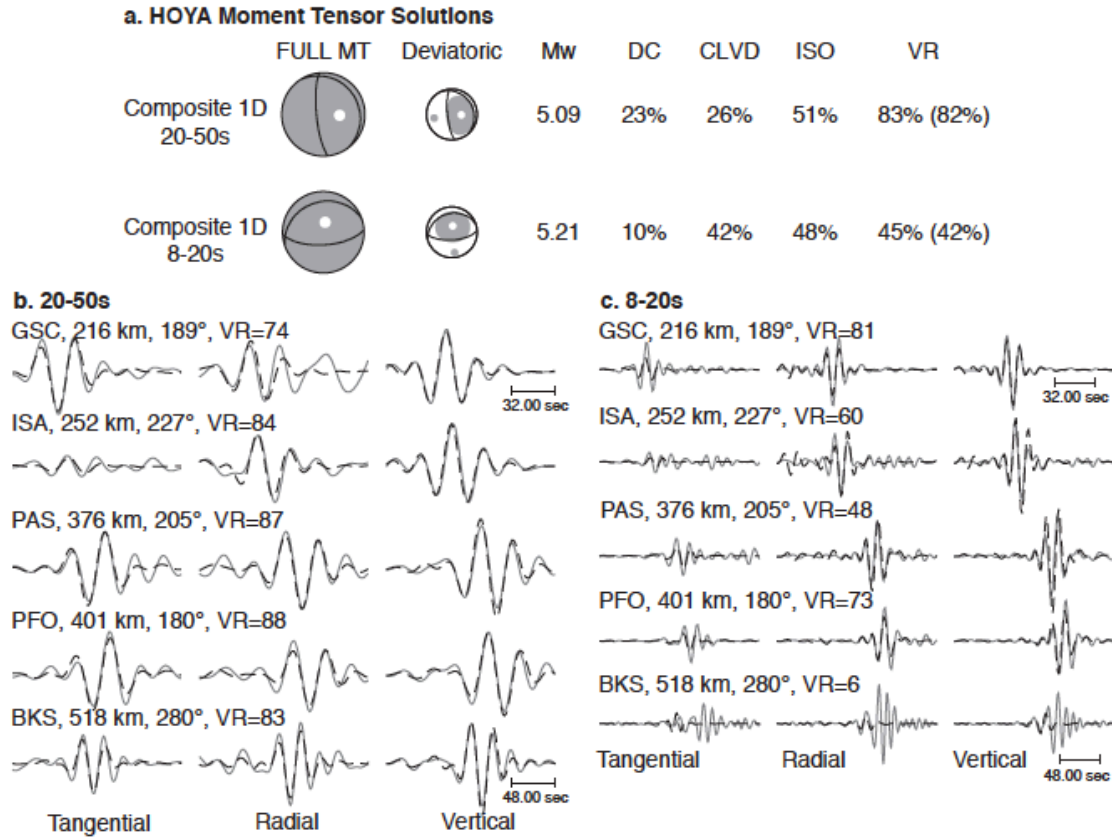
Figure 46: HOYA full moment tensor inversion results with path averaged 1D Green's functions at different frequency bands. (a) Full moment tensor focal mechanism and the deviatoric component of the solution are plotted as well as the moment magnitude (M_w), percent double-couple (DC), percent compensated linear vector dipole (CLVD), percent isotropic (ISO) and variance reduction (VR). VR from deviatoric inversion is in parentheses. (b-c) Data (solid line) and synthetic waveforms (dashed line) plotted from left to the right are the tangential, radial and vertical components.

3.4.7 Conclusion

We applied source-receiver reciprocity to compute 3D GFs using the FD method. Using the full waveform MT inversion method (Minson and Dreger, 2008) we analyze earthquakes and explosions at NTS using 1D and 3D Earth models. Other than the computation of the GFs, we applied identical data processing procedures to the 1D and 3D waveform inversion and use the same station configuration to allow for direct comparisons between the source properties and associated uncertainties of the two models and evaluate the results in different frequency bands. Our results at low frequencies show good agreement for the focal mechanisms between the two models and slight improvement in waveform fits when using the 3D model. At high frequencies the advantage of the 3D model is limited, mainly due to poor agreement between Love wave data and synthetics,

and for the two earthquakes we see an increase in non-DC components in our full 3D MT results; however we do see significant improvements in the 3D inversion along the paths to BKS and MHC and the reduction in variance is especially prominent at high frequencies. In addition, we see better agreement between Mw and the reported catalog magnitudes when 3D models are applied in the inversion. We do not see a systematic reduction in uncertainties associated with the MT when 3D GFs are applied, in most cases the uncertainties are the same between the two models at short periods but vary from event to event at long periods. The 3D model that was used tends to add a false isotropic component to MT solutions of earthquakes. While this is a negative result from a source-type discrimination perspective it is important to recognize that the improvement in fit afforded by the isotropic component is not statistically significant. Using 3D velocity models for source inversion is often cited as a means to improve results, however this analysis demonstrates that this may not always be the case and even if calibrated 3D models are employed careful analysis of uncertainty and solution sensitivity are needed before non-DC components of MTs of earthquakes can be interpreted. The results also show for the explosions that there is no difference in the ability to discriminate the explosions from earthquakes, which is a positive result, although reduced uncertainty in the source-type goodness of fit space using the 3D GFs would be preferred. The results however do show that the minor non-isotropic components of explosions are highly variable with respect to both the velocity model and the passband. This means that it will be difficult to interpret such results for mechanisms of non-isotropic radiation in explosions from MT inversions.

Our results indicate that the surface wave derived 3D model for the Western U.S. for seismic MT estimation still needs further refinement along the paths we examined (except perhaps BKS/MHC) to model wave propagation at high frequencies, and instead of the more costly 3D simulation using path-averaged 1D models for short period inversion is a more practical option in many cases. A 3D model by Shen et al. (2013) that uses additional constraints from receiver functions should be evaluated and compared to the MT inversion results using the Moschetti et al. (2010) model in future work. In this study we have established a procedure to compare and evaluate 1D and 3D source inversions. When models with better crustal resolutions become available we can begin to explore depth sensitivity for both explosions and shallow earthquakes. It is likely that when trying to improve capabilities for other regions of the world that multiple 3D velocity models will need to be tested, as well as perturbations to those models in order to evaluate the stability of source solutions obtained with 3D velocity models, much in the same way that it is necessary to do so with 1D models.

4. CONCLUSIONS

In section 3.1, we define elements of the general MT in terms of: (1) its normalized eigenvalues that characterize its source-type, (2) a seismic moment scale factor that scales the normalized eigenvalues to appropriate size or scalar moment, and (3) its eigenvectors that specify its orientation. We utilize this formulation to implement an iterative damped LS inversion scheme to invert displacement waveforms for best fitting eigenvectors and the moment scale factor for specific eigenvalues, which results in the best-fitting MT solution for a specific

source-type. However, the expressions are general and can be used with other appropriate inversion techniques as well. Our technique is successfully demonstrated by estimating best fitting MT solutions for synthetic data assuming various source types: cracks, explosion and DC. For low frequency displacement waveforms of the three example events, we find the NSS computed using the inversion approach to be faster and more accurate by VR ~ 0-3% compared to NSS computed by forward modeling 80 million randomly generated MT. To better constrain the source-types of these seismic events, we employ an approximation of the sign function in order to invert FM polarity data along with displacement waveforms using our derivative-based inversion scheme. We find that our inversion method is more successful than the random search approach in recovering the MT solution with the maximum VR as well as the region of best-fitting MT solutions or source-types for NSS computed using low-frequency displacement waveforms and P-wave FM polarities both separately and jointly. The inclusion of P-wave first-motion observations with long-period waveforms narrows the range of possible MT solutions in source-type space leading to improved source-type discrimination (e.g. Ford et al., 2012; Chiang et al., 2014).

In section 3.2 the effects of shallow depth of burial and the impact of vanishing traction at the free-surface on the recovery of the seismic moment tensor is examined. Theoretical vertical dip-slip Green's functions associated with the M_{xz} and M_{yz} components have vanishing amplitudes at shallow depths (< 1 km) due to the loss of traction at the free surface, while the Green's function waveforms look similar with little phase distortion. However synthetic calculations at shallow depths show moment tensor based event discrimination is reliable and the resolvability of the moment tensor solution depends on station configuration, noise level, the frequency band, and the velocity model.

We are able to recover a predominantly explosive source mechanism for the three HUMMING ALBATROSS chemical explosions from moment tensor inversions. Although the source-type uncertainty analysis shows that we cannot uniquely characterize the events as predominantly explosive using only waveform data, the combined waveform and first motion method enables the unique discrimination of these events. This method has been applied in previous studies which have shown the inclusion of P-wave first motions in addition to full waveform data eliminates the common ISO-CLVD tradeoff (Ford et al., 2012; Chiang et al., 2014) and reduces the uncertainties of sparsely recorded underground explosions with strong Love waves and reversed Rayleigh waves (Chiang et al., 2014). In this study we further demonstrate that incorporating the two data sets is particularly useful in constraining the isotropic component of explosions, and the method not only applies to large events, but also small magnitude, very shallow explosions that are effectively at the free surface. The combination of both low frequency full waveform data and high frequency P-wave polarities greatly enhances the capabilities of the moment tensor source-type discrimination method in cases of sparse station coverage, strong Love waves and free-surface effects.

The moment tensor method is capable of event discrimination, and although yield estimation using the recovered absolute seismic moment from moment tensor inversion remains challenging and can have large uncertainties, we can begin to put error bounds on our moment estimates, and therefore yield, using the NSS technique and combining waveform and first motion.

In section 3.3 numerical experiments were conducted to investigate the effect of 3D seismic velocity structure on the recovery of the seismic moment tensor and in discriminating the event source-type. The results of the synthetic 3D model sensitivity tests show that using 1D velocity models to compute Green's functions for use in long-period (as short as 10 seconds) MT inversions is possible, and that at least synthetically, we do not find significant bias in solutions, nor issues in being able to discriminate different types of sources. For the DC case, we can recover the correct mechanism and source depth using a universal 1D velocity model for all stations. The ISO component in the full MT is less than 20% for the two DC mechanisms explored. But for the oblique mechanism the inversion recovers a solution with a high CLVD component, resulting in a solution that is 50% DC. The observation of false non-DC components up to 50% for the earthquake source shows that although the correct fault plane solutions for the DC can be recovered at relatively long periods, the CLVD component can be large in full MT inversions, however the NSS remains earthquake-like focused at the origin of the source-type plot. For the explosion cases, the level of false non-ISO is dominated by the ISO-CLVD tradeoff, although the recovered MT consists of a CLVD solution the DC component is less than 10%, and the NSS exhibits the typical explosion-like signature in source-type space (e.g. Ford et al., 2010). Including additional data from first motion polarities can eliminate the trade-off and the correct solution can be recovered. The constrained MT solution is predominantly explosive and has a very low DC of 9%. Similarly, results for the explosive composite source show the tradeoff affects the recoverability of the MTs. The fault plane orientation of the DC component in a composite source cannot be constrained well, except for the case with 50% DC and 50% ISO. Results from synthetic tests using a more heterogeneous 3D model with crustal velocity fluctuations following the von Karman distribution show the full MT inversion can recover the correct DC mechanism. The percentage of non-DC remains the same compared to the result for a smooth model but the solution has higher uncertainties as indicated by lower waveform fits and larger variability in the NSS. When an explosion source is considered the false-DC component increases to almost 50% in the inversion. The NSS exhibits an explosion-like signature in the source-type space but with large variability that extends to a pure DC source. But considering the best solution with first motion constraints shows a predominantly explosive source with a slightly higher DC of 28% compare to the results from a smooth model. The false non-DC components in earthquakes and the false-DC components in explosions arising from unaccounted for 3D path effects can be reduced by using path-specific 1D Green's functions. The Green's functions are computed by taking the average 1D model for each source-receiver path from the 3D tomographic model. Path-calibration also reduces the large uncertainty in the NSS for the oblique mechanism.

In section 3.4 source-receiver reciprocity is used to compute Green's functions accounting for 3D wave propagation effects in the western US. These 3D velocity model Green's functions are then used to examine moment tensor solutions for NNSS nuclear explosions and nearby earthquakes. Using the full waveform MT inversion method (Minson and Dreger, 2008) we analyze earthquakes and explosions at NTS using 1D and 3D Earth models. Other than the computation of the GFs, we applied identical data processing

procedures to the 1D and 3D waveform inversion and use the same station configuration to allow for direct comparisons between the source properties and associated uncertainties of the two models and evaluate the results in different frequency bands. Our results at low frequencies show good agreement for the focal mechanisms between the two models and slight improvement in waveform fits when using the 3D model. At high frequencies the advantage of the 3D model is limited, mainly due to poor agreement between Love wave data and synthetics, and for the two earthquakes we see an increase in non-DC components in our full 3D MT results; however we do see significant improvements in the 3D inversion along the paths to BKS and MHC and the reduction in variance is especially prominent at high frequencies. In addition, we see better agreement between Mw and the reported catalog magnitudes when 3D models are applied in the inversion. We do not see a systematic reduction in uncertainties associated with the MT when 3D GFs are applied, in most cases the uncertainties are the same between the two models at short periods but vary from event to event at long periods. The 3D model that was used tends to add a false isotropic component to MT solutions of earthquakes. While this is a negative result from a source-type discrimination perspective it is important to recognize that the improvement in fit afforded by the isotropic component is not statistically significant. Using 3D velocity models for source inversion is often cited as a means to improve results however this analysis demonstrates that this may not always be the case, and even if calibrated 3D models are employed careful analysis of uncertainty and solution sensitivity are needed before non-DC components of MTs of earthquakes can be interpreted. The results also show for the explosions that there is no difference in the ability to discriminate the explosions from earthquakes, which is a positive result, although reduced uncertainty in the source-type goodness of fit space using the 3D GFs would be preferred. The results however do show that the minor non-isotropic components of explosions is highly variable with respect to both the velocity model and the passband. This means that it will be difficult to interpret such results for the mechanism of non-isotropic radiation in explosions from MT inversions.

Our results indicate that the surface wave derived 3D model for the Western U.S. for seismic MT estimation still needs further refinement along the paths we examined (except perhaps BKS/MHC) to model wave propagation at high frequencies, and instead of the more costly 3D simulation using path-averaged 1D models for short period inversion is a more practical option in many cases. A 3D model by Shen et al. (2013) that uses additional constraints from receiver functions should be evaluated and compared to the MT inversion results using the Moschetti et al. (2010) model in future work. In this study we have established a procedure to compare and evaluate 1D and 3D source inversions, when models with better crustal resolutions become available we can begin to explore depth sensitivity for both explosions and shallow earthquakes. It is likely that when trying to improve capabilities for other regions of the world that multiple 3D velocity models will need to be tested, as well as perturbations to those models in order to evaluate the stability of source solutions obtained with 3D velocity models, much in the same way that it is necessary to do with 1D models.

REFERENCES

Abdulah, A., (2007), "Seismic body wave attenuation tomography beneath the Seismic body wave attenuation tomography beneath the Australasian region," PhD thesis, The Australian National University.

Aki, K. and Richards, P.G., (2002), *Quantitative Seismology,* Ed. by Ellis, J. Sausalito, California, University Science Books, Second edition.

Appelo, D. and Petersson, N.A., (2009), "Communications in Computational Physics," In: *A Stable Finite Difference Method for the Elastic Wave Equation on Complex Geometries with Free Surfaces* 5, pp. 84–107.

Baise, L.G., Dreger, D.S., and Glaser, S.D., (2003), "The Effect of Shallow San Francisco Bay Sediments on Waveforms Recorded during the MW 4.6 Bolinas, California, Earthquake," In: *Bulletin of the Seismological Society of America* 93.1, pp. 465–479, doi: 10.1785/0120010213.

Barker, T., McLaughlin, K.L., Stevens, J.L., and Day, S.M., (1993), *Numerical models of quarry blast sources: effects of the bench,* S-CUBED Report SSS-TR-93–13915, Maxwell Laboratories, La Jolla, CA.

Bensen, G.D., Ritzwoller, M.H., and Yang, Y., (2009), "A 3-D shear velocity model of the crust and uppermost mantle beneath the United States from ambient seismic noise," Beckman, J.D., and A.K. Williamson (1990), Salt-dome locations in the Gulf coastal plains, south-central United States, *USGS Water-Resources Investigations Report 90-4060.*

Bhattacharyya, J., Sheehan, A.F., Tiampo, K., and Rundle, J., (1999), "Using a genetic algorithm to model broadband regional waveforms for crustal structure in the western United States," In: *Bulletin of the Seismological Society of America* 89.1, pp. 202–214.

Bonner, J.L, Herrin, E.T., and Goforth, T.T., (1996), Azimuthal variation of Rg from Central Texas quarry blasts, *Seism. Res. Letts.*, **67**.

Bowers, D. and J.A. Hudson, (1999), Defining the scalar moment of a seismic source with a general moment tensor, *Bull. Seismol. Soc. Am.,* **89**, 5, pp. 1390-1394.

Boyd, O.S., Dreger, D.S., Lai, V.H., and Gritto, R., (2015), A Systematic Analysis of Seismic Moment Tensor at The Geysers Geothermal Field, California, accepted to *Bull. Seism. Soc. Am.*, 105, No. 6, doi:10.1785/0120140285.

Brocher, T.M., (2005), "Empirical Relations between Elastic Wavespeeds and Density in the Earth's Crust," In: *Bulletin of the Seismological Society of America* 95.6, pp. 2081–2092. doi: 10.1785/0120050077.

Burger, R.W., Lay, T., Wallace, T.C., and Burdick, L. J., (1986), Evidence of tectonic release in long-period *S* waves from underground nuclear explosions at the Novaya Zemlya test sites, *Bull. Seismol. Soc. Amer.* **76**, pp. 733-755.

Burger, R.W., Lay, T., and Burdick, L.J., (1987), "Average Q and yield estimates from the Pahute Mesa test site," In: *Bulletin of the Seismological Society of America* 77.4, pp. 1274–1294.

Chiang, A., Dreger, D.S., Ford S.R., and Walter W.R., (2014), Source characterization of underground explosions from combined regional moment tensor and first-motion analysis, *Bull. Seism. Soc. Am.*, **104**(4), pp. 1587-1600.

Chiang A., Dreger, D.S. Ford, S.R., Walter, W.R., and Yoo S-H., (2016), Moment Tensor Analysis of Shallow Sources, *submitted to Bull. Seism. Soc. Am., under revision.*

Covellone, B.M. and Savage, B., (2012), "A Quantitative Comparison between 1D and 3D Source Inversion Methodologies: Application to the Middle East," In: *Bulletin of the Seismological Society of America* 102.5, pp. 2189–2199, doi:10.1785/0120110278.

Dahlen, F. A. and Tromp, J., (1998), *Theoretical Global Seismology,* Princeton University Press.

Day, S.M., Cherry, J.T., Rimer, N., and. Stevens, J.L., (1987), Nonlinear model of tectonic release from underground explosions, *Bull. Seismol. Soc. Amer.,* **77**, pp. 996-1016.

Dreger, D.S. and Helmberger, D.V., (1990), "Broadband modeling of local earthquakes," In: *Bulletin of the Seismological Society of America* 80.5, pp. 1162–1179.

Dreger, D.S. and Helmberger, D.V., (1993), Determination of source parameters at regional distances with three-component sparse network data, *J. Geophys. Res.,* **98**, no. B5, pp. 8107-8125.

Dreger, D. and Woods, B., (2002), "Regional distance seismic moment tensors of nuclear explosions." In: *Tectonophysics* 356.1–3. Seismic Source Mechanism through Moment Tensors, pp. 139–156, doi: http://dx.doi.org/10.1016/S0040-1951(02)00381-5.

Dreger, D.S., (2003), "85.11 TDMT INV: Time domain seismic moment tensor INVersion," In: *International Handbook of Earthquake and Engineering Seismology,* Ed. by Lee, W. H., Kanamori, H., Jennings, P. C., and Kisslinger, C. Vol. 81, International Geophysics Part B. ACADEMIC PRESS, p. 1627.

Dreger, D.S., Ford, S.R., and Walter, W.R., (2008), Source analysis of the Crandall Canyon, Utah, mine collapse, *Science* **321**, p. 217.

Dziewonski, A. and Anderson, D., (1981), "Preliminary reference Earth model," In: *Physics of the Earth and Planetary Interiors* 25, pp. 297-356.

Eisner, L. and Clayton, R.W., (2001), "A Reciprocity Method for Multiple-Source Simulations," In: *Bulletin of the Seismological Society of America* 91.3, pp. 553–560, doi: 10.1785/0120000222.

Ekström G. and Richards P.G., (1994), Empirical measurements of tectonic moment release in nuclear explosions from teleseismic surface waves and body waves, *Geophys. J. Int.,* **117**, pp. 120-140.

Fichtner, Andreas, Brian, L.N., Kennett, Heiner Igel, and Hans-Peter, Bunge, (2009), Full waveform tomography for upper-mantle structure in the Australasian region using adjoint methods, *Geophys. J. Int.*, *179*(3), pp. 1703-1725.

Fichtner, Andreas, Brian, L.N., Kennett, Heiner Igel, and Hans-Peter, Bunge, (2010), Full waveform tomography for radially anisotropic structure: New insights into present and past states of the Australasian upper mantle, *Earth and Planetary Science Letters*, *290*(3-4), pp. 270-280.

Ford, S.R., (2008), "Isotropic Sources and Attenuation Structure: Isotropic Sources and Attenuation Structure: Nuclear Tests, Mine Collapses, and Q," PhD thesis, University of California, Berkeley.

Ford, S., Dreger, D.S., and Walter, W.R., (2008), Source characterization of the August 6, 2007 Crandall Canyon Mine seismic event in Central Utah, *Seismol. Res. Lett.,* **79**, pp. 637-644, doi: 10.1785/gssrl.79.5.637.

Ford, S.R., Dreger, D.S., and Walter, W.R., (2009a), Identifying isotropic events using a regional moment tensor inversion, *J. Geophys. Res.,* **114**, B01306, doi:10.1029/2008JB005743.

Ford, S.R., Dreger, D.S., and Walter, W.R., (2009b), Source analysis of the Memorial Day Explosion, Kimchaek, North Korea, *Geophys. Res. Lett.,* **36**, p. 21, L21304, doi:10.1029/2009GL040003.

Ford, S.R., Dreger, D.S., and Walter, W.R., (2010), Network sensitivity solutions for regional moment-tensor inversions, *Bull. Seismol. Soc. Am.,* **100**, 5A, pp. 1962-1970, doi: 10.1785/0120090140.

Ford, S.R., Walter W.R., and Dreger, D.S., (2012), Event discrimination using regional moment tensors with teleseismic-P constraints, *Bull. Seismol. Soc. Am.,* **102**, 2, pp. 867-872, doi: 10.1785/0120110227.

Gilbert, H.J. and Fouch, M., (2007), "Complex upper mantle seismic structure across the southern Colorado Plateau/Basin and Range: II. Results from receiver function analysis," In: *Eos Trans. AGU* 88.52.

Given, J.W., and Mellman, G.R., (1986), Estimating explosion and tectonic release source parameters of underground nuclear explosions from Rayleigh and Love wave observations, AFGL-TR-86- 0171(I), Sierra Geophysics, Inc., Kirkland, WA.

Goff, J.A. and Jordan, T.H., (1988), "Stochastic Modeling of Seafloor Morphology: Inversion of Sea Beam Data for Second-Order Statistics," In: *Journal of Geophysical Research: Solid Earth* 93.B11, pp. 13589–13608. doi: 10.1029/JB093iB11p13589.

Goforth, T.T., and Bonner, J.L., (1995), Characteristics of Rg waves recorded in central Texas, *Bull. Seismol. Soc. Am.*, **85**, pp. 1232–1235.

Graves, R.W., Aagaard, B.T., Hudnut, K.W., Star, L.M., Stewart, J.P., and Jordan, T.H., (2008), "Broadband simulations for Mw 7.8 southern San Andreas earthquakes: Ground motion sensitivity to rupture speed," In: *Geophysical Research Letters,* 35, pp. 22, L22302, n/a–n/a. doi: 10.1029/2008GL035750.

Graves, R.W. and Wald, D.J., (2001), "Resolution analysis of finite fault source inversion using one- and three-dimensional Green's functions, Strong motions," *Journ. Geophys. Res.,* 106.B5, pp. 8745–8766. doi: 10.1029/2000JB900436.

Guilhem, A., Hutchings, L., Dreger, D.S., and Johnson, L.R., (2014), Moment tensor inversions of M~3 earthquakes in the Geysers geothermal fields, California, *J. Geophys. Res. Solid Earth* **119**(3), doi: 10.1002/2013JB010271.

Hardebeck, J.L., and Shearer, P.M., (2002), A new method for determining first-motion focal mechanisms, *Bull. Seismol. Soc. Am.,* **92**, pp. 2264–2276.

Haskell, N.A., (1964), Radiation pattern of surface waves from point sources in a multi-layered medium, *Bull. Seismol. Soc. Am.,* **54**, 1, pp. 377-393.

Helmberger, D.V., (1983), "Theory and application of synthetic seismograms," In: *Earthquakes: Observation, Theory, and Interpretation : Proceedings of the International School of Physics "Enrico Fermi", Course Lxxxv,* Ed. by Kanamori, H. and Boschi, E. Proceedings of the International School of Physics, Elsevier Science Ltd, pp. 174–222.

Herrmann, R.B. and Wang, C.Y., (1985), A comparison of synthetic seismograms, *Bull. Seism. Soc. Am.,* **75**(1),pp. 41-56.

Herrmann, R.B., Benz, H., and Ammon, C.J., (2011), Monitoring the earthquake source process in North America, *Bull. Seismol. Soc. Am.,* **101**, no. 6, pp. 2609-2625.

Herrmann, R.B., (2013), Computer programs in seismology: An evolving tool for instruction and research, *Seism. Res. Lett.*, **84**(6), pp. 1081-1088.

Hingee, M., Tkalčić, H., Fichtner, A., and Sambridge, M., (2011), "Seismic moment tensor inversion using a 3-D structural model: applications for the Australian region," In: *Geophysical Journal International* 184.2, pp. 949–964. doi: 10.1111/j.1365- 246X.2010. 04897.x.

Holliger, K. and Levander, A.R., (1992), "A stochastic view of lower crustal fabric based on evidence from the Ivrea Zone," In: *Geophysical Research Letters* 19.11, pp. 1153–1156. doi: 10.1029/92GL00919.

Hudson, J.A., Pearce R.G., and Rogers, R.M., (1989), Source type plot for inversion of the moment tensor, *J. Geophys. Res.,* **94**, B1, pp. 765-774.

Julian, B.R., Miller, A.D., and Foulger, G.R., (1998), Non-Double-Couple earthquakes – 1. Theory, *Rev. Geophys.* **36**, 4, pp. 525-549.

Jost, M.L. and Herrmann R.B., (1989), A student's guide to and review of moment tensors, *Seismol. Res. Lett.,* **60**, 2, pp. 37-57.

Khalturin, V.I., Rautian, T.G., and Richards, P.G., (1998), The seismic signal strength of chemical explosions, *Bull. Seis Mol. Soc. Am.,* **88**(6), pp. 1511-1524.

Kim, S., Rhie, J., and Kim, G., (2011), "Forward waveform modelling procedure for 1-D crustal velocity structure and its application to the southern Korean Peninsula," In: *Geophysical Journal International* 185.1, pp. 453–468.

Kustowski, B., Ekstrom, G., and Dziewonski, A., (2008), "The shear-wave moment tensor inversions for earthquakes in southern California," In: *Bulletin of the Seismological Society of America* 94.5, pp. 1748–1761.

Langston, C.A., (1981), "Source inversion of seismic waveforms: The Koyna, India, earthquakes of 13 September 1967," In: *Bulletin of the Seismological Society of America* 71.1, pp. 1–24.

Langston, C.A. and Helmberger, D.V., (1975), "A Procedure for Modelling Shallow Dislocation Sources," In: *Geophysical Journal of the Royal Astronomical Society* 42.1, pp. 117– 130. doi:10.1111/j.1365-246X.1975.tb05854.x.

Larsen, S. and Shultz, C., (1995), *ELAS3D: 2D/3D elastic finite difference wave propagation code,* Technical Report UCRLMA-121792, Lawrence Livermore National Laboratory.

Laske, G. and Masters, G., (1997), "A Global Digital Map of Sediment Thickness," In: *EOS Trans., AGU* 78.F483.

Lee, E.-J., Chen, P., Jordan, T.H., and Wang, L., (2011), "Rapid full-wave centroid moment tensor (CMT) inversion in a three-dimensional earth structure model for earthquakes in Southern California," In: *Geophysical Journal International* 186.1, pp. 311–330, doi: 10.1111/j.1365-246X.2011.05031.x.

Liu, Q., Polet, J., Komatitsch, D., and Tromp, J., (2004), "Spectral-Element Moment Tensor Inversions for Earthquakes in Southern California," In: *Bulletin of the Seismological Society of America* 94.5, pp. 1748–1761. doi: 10.1785/012004038.

Massé, R.P., (1981), "Review of seismic source models for underground nuclear explosions," In: *Bulletin of the Seismological Society of America* 71.4, pp. 1249–1268.

Menke, W., (1989), *Geophysical Data Analysis: Discrete Inverse Theory,* Revised Edition, International Geophysics, Academic Press.

Menke, W., (2012), *Chapter 5 - Solution of the Linear, Gaussian Inverse Problem, Viewpoint 3: Maximum Likelihood Methods,* Ed. by Menke, W. Third Edition, Boston: Academic Press, pp. 89–114.

Moschetti, M.P., Ritzwoller, M.H., Lin, F.-C., and Yang, Y., (2010), "Crustal shear wave velocity structure of the western United States inferred from ambient seismic noise and earthquake data," In: *Journal of Geophysical Research: Solid Earth* 115.B10. B10306, n/a–n/a. doi: 10.1029/2010JB007448.

McLaughlin, K.L., Bonner, J.L., and Barker T., (2004), Seismic source mechanisms for quarry blasts: modelling observed Rayleigh and Love wave radiation patterns from a Texas quarry, *Geophys. J. Int.,* **156**, pp. 79–93, doi: 10.1111/j.1365-246X.2004.02105.x.

McNamara, D.E., Benz, H.M., Herrmann, R.B., Bergman, E.A., Earle, P., Holland, A., Baldwin, R., and Gassner, A., (2015), "Earthquake hypocenters and focal mechanisms in central Oklahoma reveal a complex system of reactivated subsurface strike-slip faulting," *Geophysical Research Letters* 42.8, 2014GL062730, pp. 2742–2749. doi: 10.1002/ 2014GL062730.

Minson, S.E., Dreger, D.S., Burgmann, R., Kanamori H., and Larson K.M., (2007), Seismically and geodetically determined non-double couple source mechanisms from the Miyakejima volcanic earthquake swarm, *J. Geophys. Res.,* **112**, B10308, doi:10.1029/2006JB004847.

Minson, S.E. and Dreger, D.S., (2008), Stable inversions for complete moment tensor, *Geophys. J. Int.,* **174**, pp. 585-592, doi: 10.1111/j.1365-246X.2008.03797.x.

Mueller, R.A. and Murphy, J.R., (1971), Seismic Characteristics of Underground Nuclear Detonations, I: Seismic Spectrum Scaling, *Bull. Seism. Soc. Am.,* 61, pp. 1675-1692.

Murphy, J.R., (1977), Seismic coupling and magnitude/yield relations for underground nuclear detonations in salt, granite, tuff/rhyolite and shale emplacement media, CSCTR-77-0004, Comput. Sci. Corp., Falls Church, VA.

Murphy, J.R., (1996), Types of seismic events and their source descriptions, in Monitoring a Comprehensive Test Ban Treaty, Eystein S. Husebye and Anton M. Dainty (Editors), Kluwer Academic Publishers, Dordrecht, Netherlands, pp. 225-245.

Nakano, M. and Kumagai, H., (2005), Waveform inversion of volcano-seismic signals assuming possible source geometries, *Geophys. Res. Lett.,* 32, L12302, doi:10.1029/2005GL022666.

Nayak, A. and Dreger, D.S., (2014), Moment tensor inversion of seismic events associated with the sinkhole at Napoleonville Salt Dome, Louisiana, *Bull. Seism. Soc. Am.*, 104, pp.1763-1776.

Nayak, A. and Dreger, D.S., (2015), Source-type Specific Inversion of Moment Tensors, accepted to *Bull. Seism. Soc. Am.,* 105:2987-3000; doi:10.1785/0120140334.

Nielsen, L. and Thybo, H., (2006), "Identification of crustal and upper mantle heterogeneity by modelling of controlled-source seismic data," In: *Tectonophysics* 416, pp. 209–228.

Olsen, K.B., Day, S.M., Dalguer, L.A., Mayhew, J., Cui, Y., Zhu, J., Cruz-Atienza, V.M., Roten, D., Maechling, P., Jordan, T.H., Okaya, D., and Chourasia, A., (2009), "ShakeOut- D: Ground motion estimates using an ensemble of large earthquakes on the southern San Andreas fault with spontaneous rupture propagation," In: *Geophysical Research Letters* 36.4, L04303, n/a–n/a, doi:10.1029/2008GL036832.

Panning, M., Dreger, D.S., and Tkalcic, H., (2001), Near-source velocity structure and isotropic moment tensors: a case study of the Long Valley Caldera, *Geophys. Res. Lett.,* **28**, pp. 1815-1818.

Pasyanos, M.E., Dreger, D.S., and Romanowicz, B., (1996), "Toward real-time estimation of regional moment tensors," In: *Bulletin of the Seismological Society of America* 86.5, pp. 1255–1269.

Pasyanos, M.E., Franz, G.A., and Ramirez, A.L., (2006), "Reconciling a geophysical model to data using a Markov chain Monte Carlo algorithm: An application to the Yellow Sea–Korean Peninsula region," In: *Journal of Geophysical Research: Solid Earth* 111.B3. B03313, n/a–n/a, doi:10.1029/2005JB003851.

Pearce, R.G. and Rogers, R.M., (1989), Determination of Earthquake Moment Tensors From Teleseismic Relative Amplitude Observations, *J. Geophys. Res.* **94**(B1), pp. 775-786.

Petersson, N.A. and Sjogreen, B., (2014), "Super-grid modeling of the elastic wave equation in semi-bounded domains," In: *Communications in Computational Physics* 16.4, pp. 913–955.

Porritt, R.W., Allen, R.M., and Pollitz, F.F., (2014), "Seismic imaging east of the Rocky Mountains with *{*USArray*},*" In: *Earth and Planetary Science Letters* 402, Special issue on *{*USArray*}* science, pp. 16–25, doi:http://dx.doi.org/10.1016/j.epsl.2013.

Ramos-Martínez, J. and McMechan, G.A., (2001), "Source-Parameter Estimation by Full Waveform Inversion in 3D Heterogeneous, Viscoelastic, Anisotropic Media," In: *Bulletin of the Seismological Society of America* 91.2, pp. 276–291, doi: 10.1785/0120000017.

Reasenberg, P.A. and Oppenheimer, D., (1985), FPFIT, FPPLOT, and FPPAGE: Fortran computer programs for calculating and displaying earthquake fault-plane solutions, *U.S. Geol. Surv. Open-File Rep., 85-739.*

Saikia, C.K., Kafka, A.L., Gnewuch, S.C., and Mctigue, J.W., (1990), Shear velocity and Intrinsic Q Structure of the Shallow Crust in Southeastern New England From Rg Wave Dispersion, J. Geophys. Res., 95(B6), pp. 8527-8541.

Shen, W., Ritzwoller, M.H., and Schulte-Pelkum, V., (2013), "A 3-D model of the crust and uppermost mantle beneath the Central and Western US by joint inversion of receiver functions and surface wave dispersion," In: *Journal of Geophysical Research: Solid Earth* 118.1, pp. 262–276, doi:10.1029/2012JB009602.

Šílený, J., (2004), "Regional moment tensor uncertainty due to mismodeling of the crust," In: *Tectonophysics* 383.3-4, pp. 133–147.

Šílený, J., Hill, D.P., Eisner, L., and Cornet, F.H., (2009), Non-double-couple mechanisms of microearthquakes induced by hydraulic frac turing, *J. Geophys. Res.,* **114**, B08307, doi:10.1029/2008JB005987.

Sjogreen, B. and Petersson, N., (2012), "A Fourth Order Accurate Finite Difference Scheme for the Elastic Wave Equation in Second Order Formulation," English, In: *Journal of Scientific Computing* 52.1, pp. 17–48, doi:10.1007/s10915-011-9531-1.

Song, X.J., Helmberger, D.V., and Zhao L., (1996), Broad-Band modelling of regional seismograms: the basin and range crustal structure, *Geophys. J. Int.,* **125**(1), pp. 15-29.

Stevens, J.L. and Murphy J.R., (2001), Yield estimation from surface-wave amplitudes, *Pure and Applied Geophys.*, 158(11), pp. 2227-2251.

Springer, D.L., Pawloski, G.A., Ricca, J.L., Rohrer, R.F., and Smith, D.K., (2002), "Seismic Source Summary for All U.S. Below-Surface Nuclear Explosions," In: *Bulletin of the Seismological Society of America* 92.5, pp. 1806–1840, doi:10.1785/0120010194.

Tape, W. and Tape, C., (2012a), A geometric setting for moment tensors, *Geophys. J. Int.,* **190**(1), pp. 476-498, doi: 10.1111/j.1365-246X.2012.05491.x.

Tape, W. and Tape C., (2012b), A geometric comparison of source-type plots for moment tensors, *Geophys. J. Int.,* **190**(1), pp. 499-510, doi: 10.1111/j.1365-246X.2012.05490.x.

Tape, W. and Tape, C., (2013), The classical model for moment tensors, *Geophysical Journal International,* **Vol. 195**, pp. 1701-1720.

Tape, W. and Tape, C., (2015), A uniform parameterization of moment tensors, *Geophysical Journal International*, **Vol. 202**, pp. 2074-2081.

Templeton, D.C. and Dreger D.S., (2006), Non-double-couple earthquakes in the Long Valley Volcanic Region, *Bull. Seismol. Soc. Am.*, **96**(1), pp. 69-79, doi: 10.1785/0120040206.

Tkalčić, H., Dreger, D.S., Foulger, G.R., and Julian, B.R., (2009), "The Puzzle of the 1996 B´ardarbunga, Iceland, Earthquake: No Volumetric Component in the Source Mechanism," In: *Bulletin of the Seismological Society of America* 99.5, pp. 3077–3085.

Toksöz, M.N. and Kehrer, H. H., (1972), Tectonic strain release by underground nuclear explosions and its effect on seismic discrimination, *Geophys. J. Roy. Astron. Soc.,* **31**, pp. 141-161.

Toksöz, M.N., Harkrider, D.G., and Ben-Menahem, A., (1965), Determination of source parameters by amplitude equalization of seismic surface waves. 2. Release of tectonic strain by underground nuclear explosions and mechanisms of earthquakes, *J. Geophys. Res.,* **70**, pp. 907-922.

Vavryčuk, V., (2011), Tensile earthquakes: Theory, modeling, and inversion, *J. Geophys. Res.,* **116**, no. B12320, doi:10.1029/2011JB008770.

Vavryčuk, V., (2015), Moment tensor decompositions revisited, *J. Seismol.,* 19(1), pp. 231-252.

Walter, W.R. and Rodgers, A.J., (1999), Regional waveform modeling in southwestern Asia; tectonic release from the May 11, 1998 Indian nuclear tests, 94th SSA Annual Meeting, *Seismol. Res. Lett.,* **70**, p. 228.

Walter, F., Clinton, J.F., Deichmann, N., Dreger, D.S., Minson, S.E., and Funk, M., (2009), "Moment Tensor Inversions of Icequakes on Gornergletscher, Switzerland," In: *Bulletin of the Seismological Society of America* 99.2A, pp. 852–870, doi: 10.1785/0120080110.

Walter, F., Dreger, D.S., Clinton, J.F., Deichmann, N., and Funk, M., (2010), "Evidence for Near-Horizontal Tensile Faulting at the Base of Gornergletscher, a Swiss Alpine Glacier," In: *Bulletin of the Seismological Society of America* 100.2, pp. 458–472,. doi:10.1785/0120090083.

Wang, C.Y. and Herrmann, R.B., (1980), A numerical study of P-, SV- and SH-wave generation in a plane layered medium, *Bull. Seismol. Soc. Am.,* **70**, 4, pp. 1015-1036.

Wei, S., Zhan, Z., Tan, Y., Ni, S., and Helmberger, D., (2012), "Locating earthquakes with surface waves and centroid moment tensor estimation," In: *Journal of Geophysical Research: Solid Earth,* 117.B4, B04309, doi:10.1029/2011JB008501.

Wessel, P. and Smith, W.H.F., (1998), New, improved version of Generic Mapping Tools released, *EOS Trans. AGU* **79**, p. 579.

Wu, R.-S., (1982), "Attenuation of short period seismic waves due to scattering," *Geophysical Research Letters* 9.1, pp. 9–12, doi:10.1029/GL009i001p00009.

Zhao, L., Chen, P., and Jordan, T.H., (2006), "Strain Green's Tensors, Reciprocity, and Their Applications to Seismic Source and Structure Studies," In: *Bulletin of the Seismological Society of America,* 96.5, pp. 1753–1763, doi:10.1785/0120050253.

Zhu, L. and Rivera, L.A., (2002), "A note on the dynamic and static displacements from a point source in multilayered media," In: *Geophysical Journal International,* 148.3, pp. 619–627.

APPENDIX

Partial derivatives of MT elements with respect to $(m_0, a_1, a_2, a_3, b_1, b_2)$

For partial derivatives of a quantity y with respect to $\mathbf{x} = [a_1, a_2, a_3, b_1, b_2]$, we will follow the convention

$$\frac{\partial y}{\partial \mathbf{x}} = \left[\frac{\partial y}{\partial a_1}, \frac{\partial y}{\partial a_2}, \frac{\partial y}{\partial a_3}, \frac{\partial y}{\partial b_1}, \frac{\partial y}{\partial b_2}\right] \qquad \text{(A-1)}$$

Partial derivatives of r_1 and r_2

$$\frac{\partial r_1}{\partial a_i} = \frac{a_i}{r_1} \text{ and } \frac{\partial r_1}{\partial b_j} = 0 \text{ for } i = 1,2,3 \text{ and } j = 1,2$$

$$\frac{\partial r_2}{\partial \mathbf{x}} = [-b_1 e_{23}, -b_2 e_{23}, (b_1 e_{21} + b_2 e_{22}), (a_3 e_{21} - a_1 e_{23}), (a_3 e_{22} - a_2 e_{23})] \qquad \text{(A-2)}$$

Partial derivatives of $\mathbf{e_1}$

$$\frac{\partial e_{1i}}{\partial a_j} = \frac{\delta_{ij}}{r_1} - \frac{a_i a_j}{r_1^3} \text{ for } i = 1,2,3 \text{ and } j = 1,2,3$$

$$\frac{\partial e_{1i}}{\partial b_j} = 0 \text{ for } i = 1,2,3 \text{ and } j = 1,2 \qquad \text{(A-3)}$$

Partial derivatives of $\mathbf{e_2}$

$$E = \begin{bmatrix} 0 & 0 & b_1 \\ 0 & 0 & b_2 \\ -b_1 & -b_2 & 0 \end{bmatrix}, \qquad \frac{\partial e_{2i}}{\partial a_j} = -\frac{e_{2i}}{r_2}\left(\frac{\partial r_2}{\partial a_j}\right) + \frac{E_{ij}}{r_2} \text{ for } i = 1,2,3 \text{ and } j = 1,2,3$$

$$F = \begin{bmatrix} a_3 & 0 \\ 0 & a_3 \\ -a_1 & -a_2 \end{bmatrix}, \qquad \frac{\partial e_{2i}}{\partial b_j} = -\frac{e_{2i}}{r_2}\left(\frac{\partial r_2}{\partial b_j}\right) + \frac{F_{ij}}{r_2} \text{ for } i = 1,2,3 \text{ and } j = 1,2 \qquad \text{(A-4)}$$

Partial derivatives of $\mathbf{e_3}$ with respect to $[a_1, a_2, a_3, b_1, b_2]$ can be computed using partial derivatives of $\mathbf{e_1}$ and $\mathbf{e_2}$ by simple chain rule. For example,

$$e_{31} = e_{12}e_{23} - e_{13}e_{22}$$

$$\frac{\partial e_{31}}{\partial \mathbf{x}} = e_{12}\frac{\partial e_{23}}{\partial \mathbf{x}} + e_{23}\frac{\partial e_{12}}{\partial \mathbf{x}} - e_{13}\frac{\partial e_{22}}{\partial \mathbf{x}} - e_{22}\frac{\partial e_{13}}{\partial \mathbf{x}} \tag{A-5}$$

Partial derivatives of M_{ij} with respect to $[a_1, a_2, a_3, b_1, b_2]$ can be computed using partial derivatives of $\mathbf{e_1}, \mathbf{e_2}$ and $\mathbf{e_3}$ with respect to $[a_1, a_2, a_3, b_1, b_2]$ by chain rule.

$$\frac{\partial M_{ij}}{\partial \mathbf{x}} = m_0^2 \left[\lambda_1 \left(e_{1i}\frac{\partial e_{1j}}{\partial \mathbf{x}} + e_{1j}\frac{\partial e_{1i}}{\partial \mathbf{x}} \right) + \lambda_2 \left(e_{2i}\frac{\partial e_{2j}}{\partial \mathbf{x}} + e_{2j}\frac{\partial e_{2i}}{\partial \mathbf{x}} \right) \right.$$
$$\left. + \lambda_3 \left(e_{3i}\frac{\partial e_{3j}}{\partial \mathbf{x}} + e_{3j}\frac{\partial e_{3i}}{\partial \mathbf{x}} \right) \right] \; for \; i = 1,2,3 \; and \; j = 1,2,3 \tag{A-6}$$

The partial derivatives with respect to the moment scale factor are straightforward.

$$\frac{\partial M_{ij}}{\partial m_0} = \frac{2M_{ij}}{m_0} \; for \; i = 1,2,3 \; and \; j = 1,2,3 \tag{A-7}$$

DISTRIBUTION LIST

DTIC/OCP
8725 John J. Kingman Rd, Suite 0944
Ft Belvoir, VA 22060-6218   1 cy

AFRL/RVIL
Kirtland AFB, NM 87117-5776   2 cys

Official Record Copy
AFRL/RVBYE/Robert Raistrick   1 cy

This page is intentionally left blank.